Ignition and propagation mechanisms of spray flames

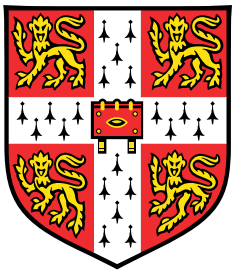

Pedro Magalhães de Oliveira

Department of Engineering
University of Cambridge

Doctor of Philosophy

Magdalene College

May 2019

Declaration

This dissertation is the result of my own work and contains nothing which is the outcome of work done in collaboration except where specifically indicated in the text. It has not been submitted for another qualification to this or any other university. It contains 40,000 words, 57 figures and 5 tables.

Pedro Magalhães de Oliveira
May 2019

Ignition and propagation mechanisms of spray flames

Pedro Magalhães de Oliveira

Abstract

Fuel droplets represent strong inhomogeneities that are generally detrimental and intensify the stochastic behaviour of ignition. Still, the presence of small droplets has been found to decrease minimum ignition energies and enhance flame speeds. In this study, a comprehensive analysis of the phases of ignition in sprays is carried out in a controlled, well-characterised experiment: the initiation of a spherically expanding flame in a turbulent droplet-laden jet by a laser spark. A revision of definitions of ignition-related terms is proposed based on a critical time scale of the spark effects on the flame, evaluated from OH* visualisation, allowing for a distinction between the phases of kernel generation and flame growth. Based on the critical time scale, ignition failure time scales can be measured, as well as kernel sizes conditional on ignition or failure. Small kernels typically quenched faster than the critical time scale, characterising the short-mode failure. This mode was suppressed by increasing the laser energy and, consequently, the initial kernel size. Still, the ignitability of lean ethanol mixtures was only effectively improved through high-energy sparks and partial prevaporisation, with ignition being limited by breakdown. In jet fuel sprays, a suppression of short and long-mode failure occurred by decreasing the droplet size. In fact, by doing this, different flame propagation mechanisms were observed by OH/fuel PLIF. Both aviation fuels investigated – Jet A and a renewable alternative, ATJ-8 – exhibited similar flame speed behaviour due to changes in droplet size in each of the modes identified: the droplet, inter-droplet, and gaseous-like propagation modes. Concentrated reactions around large droplets found in lean conditions allowed for a slowly propagating flame front which ignited new droplets. Stoichiometric to rich conditions presented stronger evaporation at the flame and higher and more uniform heat release. Still, large droplets penetrated the flame, locally inducing regions of negative curvature and continuing to evaporate in the products. The droplet-induced effects disappeared at low SMD and rich conditions, giving rise to a fully gaseous layer at the flame and the highest flame speeds. Finally, insight and data from experiments are used to improve a low-order ignition model towards applications with sprays. Fuel fluctuations are modelled using a stochastic approach, and the extinction criterion of the model is calibrated. The model is then tested for an aviation gas-turbine combustor.

laboratorium est oratorium
J. Needham

Acknowledgements

I am truly grateful to Professor Nondas Mastorakos, who, by welcoming me into his group, opened Cambridge's heavy and squeaky doors beyond Trumpington Street. His guidance, trust in my work, and tremendous generosity throughout these years were essential to this thesis.

To Professor Stewart Cant and Professor Yannis Hardalupas (Imperial College), for their time examining this work and for a stimulating viva.

To Dr. Patton Allison, for introducing me to experimental combustion and for our lasting collaboration in many other projects; Dr. Philip Sitte, for all his insight on spray combustion and close assistance with the numerical work; Dr. Andrea Giusti, for the collaboration and for kindly providing important simulation data for this thesis; Dr. Girish Nivarti, for all the exciting scientific discussions; Dr. Aaron Skiba, for his ideas on visualisation techniques; Tomoki Higuchi for the schlieren system; Tim Watson and James Massey for the positive support throughout this work. To friends and colleagues at the *Department of Engineering* who have taken the time to teach me.

To Dr. Med Colket, Dr. Josh Heyne, and the U.S.' *National Jet Fuels Combustion Program*, and to Dr. Tim Edwards at the *U.S. Air Force Research Laboratory* for kindly providing the jet fuels.

To the *Brazilian Space Agency (AEB)* and Brazil's *National Council for Scientific and Technological Development* for funding this work and, most importantly, to Professor Carlos Gurgel at *AEB* who believed in this project. I am also grateful to the *European Commission Clean Sky* projects Amel (#641453) and Proteus (#785349).

To *Magdalene College*. One cannot put into words the beauty and despair of a cloistered life of rowing and port. I am grateful to all friends who helped me by putting my work into perspective, and to the Fellows and Master of the College who have been nothing

but kind, interested, and welcoming. I also thank the Tutor's Fund and the Derman Christopherson Award.

To Professor Jader R. Barbosa Jr. (UFSC) and to Dr.-Ing. Klaus Mösl (TU Munich), whose encouragement, kindness, and continued support led me here.

To Maria, for her utmost, unconditional support and for reducing to nothing the transatlantic distance between the two Cambridges.

To my loving parents and sister.

To the Brazilian people and our unwavering hope in Science.

Publications

The content of this thesis has been published in the following papers:

Journal articles

- de Oliveira, P.M., Sitte, M.P., Mastorakos, E., Giusti, A., Zedda, M. 'Low-order modelling of spray ignition in gas turbine combustors at high-altitude relight conditions'. (in preparation)

- de Oliveira, P.M., Sitte, M.P., Mastorakos, E. 'Polydispersity effects in low-order ignition modelling of jet fuel sprays', *Combustion Science and Technology*. (accepted)

- de Oliveira, P.M., Mastorakos, E. [2019] 'Mechanisms of flame propagation in jet fuel sprays as revealed by OH/fuel planar laser-induced fluorescence and OH* chemiluminescence'. *Combustion and Flame* **206**, 308–321.

- de Oliveira, P.M., Allison, P.M., Mastorakos, E. [2019] 'Ignition of uniform droplet-laden weakly turbulent flows following a laser spark', *Combustion and Flame* **199**, 387-400.

Conference papers

- de Oliveira, P.M., Sitte, M.P., Mastorakos, E. [2019] 'Polydispersity effects in low-order ignition modelling of jet fuel sprays', *11th Mediterranean Combustion Symposium*, Tenerife, Spain.

- de Oliveira, P.M., Mastorakos, E. [2019] 'The structure of spherical flames in turbulent two-phase flows as revealed by OH and fuel PLIF', *57th AIAA Aerospace Sciences Meeting*, San Diego, USA.

- de Oliveira, P.M., Sitte, M.P., Mastorakos, E. [2019] 'Validation of a low-order model for ignition of sprays', *57th AIAA Aerospace Sciences Meeting*, San Diego, USA.

- de Oliveira, P.M., Mastorakos, E. [2018] 'Effects of droplet size on the ignition of conventional and alternative jet fuels in turbulent air', *Proceedings of the 9th International Symposium on Turbulence*, Heat and Mass Transfer, Rio de Janeiro, Brazil.

- de Oliveira, P.M., Higuchi, T., Allison, P.M., Mastorakos, E. [2017] 'Flame speed measurements in turbulent dispersions of liquid fuels', *26th Interantional Colloquium on the Dynamics of Explosions and Reactive Systems*, Boston, USA.

- de Oliveira, P.M., Allison, P.M., Mastorakos, E. [2017] 'Early phase of laser ignition processes in droplet-laden turbulent flows'. *Proceedings of the 9th World Conference on Experimental Heat Transfer, Fluid Mechanics, and Thermodynamics*, Iguazu Falls, Brazil.

- de Oliveira, P.M., Allison, P.M., Mastorakos, E. [2017] 'Forced ignition of dispersions of liquid fuel in turbulent air flow', *55th AIAA Aerospace Sciences Meeting*, Grapevine, USA.

Contents

List of figures

List of tables

Nomenclature

Roman letters

c_p	Specific heat at constant pressure [J/kg · K]
d	Droplet diameter [m, µm]
d_q	Quenching distance [mm]
h	Specific enthalpy [J/kg]
h_{lv}	Enthalpy of vaporisation [J/kg]
k	Turbulent kinetic energy [m^2/s^2]
l_d	Mean droplet spacing [m]
n	Droplet number density [m^{-3}]
p	Pressure [Pa]
q	Rosin-rammler constant [−]
r	Radius or radial coordinate [mm, m]
t	Time [s, ms, µs]
u	Velocity [m/s]
B	Spalding number [−]
D	Mass diffusivity [m^2/s]
Da	Damköhler number [−]
F	Flammability [−]
G	Group combustion number
Ka	Karlovitz number [−]
L_turb	Integral length scale [m]
Le	Lewis number [−]
N	Number of droplets [−]
P	Probability [−]
Pr	Prandtl number [−]
Q	Accumulated volume [−]
Re	Reynolds number [−]

S	Flame speed or burning velocity [m/s]
Sc	Schmidt number [−]
St	Stokes number [−]
T	Temperature [K, °C]
T_{turb}	Integral timescale scale [s]
$\mathbf{U}$	Velocity vector
U_{b}	Bulk flow velocity [m/s]
V	Volume [m^3]
X	Rosin-Rammler constant [µm]
$\mathbf{X}$	Cartesian coordinates vector

Greek letters

α	Thermal diffusivity [m^2/s]
δ	Flame thickness [mm]
η	Kolmogorov length scale [µm]
ε	Turbulent dissipation rate [m^2/s^3]
κ	2-Dimensional curvature [m^{-1}]
λ	Thermal conductivity [W/m·K]
μ	Dynamic viscosity [$Pa \cdot s$]
ν	Kinematic viscosity [m^2/s]
ξ	Mixture fraction [−]
ρ_{turb}	Density [kg/m^3]
ρ	Autocorrelation coefficient [−]
ϕ	Equivalence ratio [−]
Γ	OH* emission density [a.u.]
Γ	Mass source term [s^{-1}]
Π	Ignition progress factor [−]
Ω	Prevaporisation degree [−]

Subscript indices

a	Air
atm	Atmospheric
abs	Absorbed
b	Burnt or bulk
bd	Breakdown

c	Cell
crit	Critical
d	Droplet
f	Fuel or flame
g	Gaseous
ign	Ignition
in	In or incident
ker	Kernel
l	Liquid
lean	Lean flammability limit
long	Relative to the long-mode ignition failure
m	Modified
out	Out
p	Pressure or particle
r	Radial coordinate
rich	Rich flammability limit
sat	Saturation
short	Relative to the short-mode ignition failure
st	Stoichiometric
trans	Transmitted
turb	Turbulent
u	Unburnt
x	X coordinate
y	Y coordinate
z	Axial or z coordinate
L	Liquid
R	Jet radius
T	Turbulent

Superscript indices

sat	Saturated

Overbar symbols

$\bar{}$	Average
$\circ$	Unstretched
$'$	Fluctuation

Acronyms

DNS	Direct numerical simulation
ER	Equivalence ratio
LDA	Laser doppler anemometry
LIBS	Laser-induced breakdown spectroscopy
PDA	Phase doppler anemometry
PDF	Probability density function
PLIF	Planar laser-induced fluorescence
RANS	Reynolds-averaged Navier-Stokes
RMS	Root mean square
SMD	Sauter mean diameter

Chapter 1

Introduction

1.1 Motivation

Turbulent spray combustion is present in a range of devices such as aviation gas-turbines and liquid-propellant rocket engines. In these equipment, the process of igniting the mixture in the combustion chamber is complex, as it involves a series of interdependent physical phenomena occurring in the two-phase flow: the atomisation and evaporation of the fuel droplets, turbulence and mixing in the gas-phase, and the interaction of droplets with the spark and, subsequently, with the flame.

The ignitability of an aviation engine, for example, is highly dependent on its operating conditions. From ground cold start to altitude relight of the engine, significant changes in fuel atomisation and distribution in the combustor control the establishment of a flame [Lefebvre and Ballal, 2010]. Thus, the use of alternative jet fuels or blends has a direct impact on ignition, not only due to chemical differences between fuels but, notably, due to changes in fuel atomisation and evaporation caused by small variations in thermophysical properties. Nonetheless, ignition of the combustor must be ensured under all circumstances. Ignition is, therefore, a key design parameter limiting both the operating range of the engine and the use of alternative non-petroleum fuels – an urgent challenge in commercial aviation to mitigate climate change [International Civil Aviation Organization (ICAO), 2013].

It is generally understood that the process of initiating a flame in a combustor requires a mixture with optimal equivalence ratio in the vicinity of the spark. However, this process is highly stochastic, and failure to ignite can occur even in the presence of an overall flammable mixture [Mastorakos, 2009]. Typically, this random behaviour has been studied numerically under ideal flow conditions, although such simulations

are limited by simplifying modelling assumptions, or studied experimentally in burners involving features of gas-turbine combustion, which are characterised by the complexities arising from recirculating flows, spray atomisation, and the flame's stabilisation mechanism. In this thesis, ignition is studied from a fundamental perspective through canonical experiments, allowing further development of an ignition model.

This PhD research was carried out at the Hopkinson Laboratory of the Department of Engineering thanks to the generous support of the Brazilian Space Agency and Brazil's National Council for Scientific and Technological Development. The work was developed under the auspices of the EU Commission's Clean Sky Program and in collaboration with the U.S.' National Jet Fuels Combustion Program.

1.2 General objectives and outline

The development of cleaner and more efficient aviation engines relies on fundamental understanding of the ignition process. In a gas-turbine combustor, the key factor controlling this process is the presence of fuel in the form of finely atomised liquid droplets. For reaction to occur, fuel must be available as vapour in the gas phase. This depends on the location of the droplets in relation to the flame and, most importantly, their respective evaporation time scales. As ignition is inherently a transient process, droplets have a strong impact on the establishment of the flame, ultimately intensifying the stochastic behaviour of this process.

Numerical works have shown that the random position of droplets in the spray can be determining to an ignition event. At times, a droplet at the spark location may give rise to regions of optimal mixture which, in turn, enhance flame propagation, while a similar-sized droplet located in the vicinity of a flame kernel may extinguish the flame due to intense evaporative cooling. The mean effect of droplets on ignition over several ignition attempts is not straightforward. Experiments have focused on whole-burner ignition effects of global spray parameters, while the effect of droplets on different phases of the ignition process, from the establishment of a flame kernel to its growth into a large flame at the burner scale, is still poorly understood. These issues will be discussed next, in the literature review.

Identifying the effect of droplets on the phases of ignition can be challenging. Other than variations in the local parameters of the flow arising from spray atomisation or burner-geometry effects present in experiments, the distinction between the phases

of ignition is not clear. As it will be shown in this thesis, a measurement of radicals produced in the flame can be used to quantitatively define the early phases of the process. Further, in order to reduce the number of phenomena affecting the flame growth, experiments of ignition of spherically-expanding flames are carried out in uniform droplet dispersions in the absence of large-scale flow inhomogeneities.

The objective of this work is to investigate the role of droplets on the ignition behaviour of spray flames in simple well-controlled experiments, through a statistical and rigorous characterisation of the flame in the early phases of this process. To understand how droplets affect the propagation speed and structure of the flame, advanced high-speed diagnostics are used to visualise the droplet-flame interactions at the droplet scale. Some of the ideas and results from the experimental work are applied towards the improvement of a low-order ignition model.

This thesis is structured as follows. Chapter 2 presents a review of the main works on ignition and flame propagation in sprays, with focus on canonical experiments and simulations that investigate the physical phenomena controlling the ignition behaviour of spray flames. The open questions in the literature and the specific objectives of this thesis to address such questions are presented at the end of the literature review. The experimental and numerical methods of this work are given in Chapter 3, which includes a description of the burner, measurement techniques and models used, followed by a definition of ignition-related terms and concepts. Chapter 4 gives a full characterisation of the two-phase flow in which the ignition experiments are carried out. The findings of this study are discussed in Chapters 5 to 7; each chapter is introduced by a focused motivation section. Chapter 5 discusses the *stochastic nature of ignition* of spray flames, while Chapter 6 focuses solely on the *flame propagation mechanisms* of such flames. In Chapter 7, *a low-order ignition model* is improved with a simple stochastic model and calibrated based on data from previous chapters. Lastly, conclusions and recommendations for future work are presented in Chapter 8. Appendix A includes a reference to a video with a compilation of the phenomena visualised in the experiments.

Chapter 2

Literature review and objectives

The initiation of a flame in a flammable mixture through external action is defined as forced ignition. Differently from autoignition, where the mixture is in a state of slow chemical reaction that eventually leads to a vigorous burning state, the forced ignition process consists of adding to the mixture either enough heat or chemical radicals, or both, by means of an external source. In autoignition, this change of state occurs due to a series of interdependent rises in temperature and in reaction rate of the mixture, leading to a thermal runaway process that occurs within a time interval known as the autoignition time. In contrast, the change from a chemically frozen to a fully burning state in forced ignition occurs promptly, at first glance, as a result of a spark. Nevertheless, it involves a series of convoluted processes marked by different time scales until a steady propagating front is achieved.

In comparison to forced ignition of a gaseous mixture, the presence of droplets increases the complexity of the process as it affects each of its phases: the kernel generation, the flame growth, and the burner-scale flame establishment [Lefebvre and Ballal, 2010; Mastorakos, 2017]. In this chapter, issues related to the early phase of ignition of sprays, concerning the generation of a flame kernel up to its development into a self-sustained flame, are discussed in Sec. 2.1, while the topic of flame propagation in sprays is covered in more details in Sec. 2.2. Finally, a summary of the main open questions in the field are presented in Sec. 2.3, where the specific objectives of this work are defined. Additionally, in the following chapters, the motivations for each part of this work are given in Secs. 5.1, 6.1, and 7.1, by summarising the relevant findings and open scientific questions leading to the specific objectives to be addressed in the respective chapter.

2.1 Ignition of sprays

2.1.1 Fundamental concepts

In general terms, ignition of a flammable mixture may only occur if enough energy is delivered to a region of characteristic size in such a way that its temperature is raised high enough, kick-starting reaction and overcoming energy losses. The minimum energy to promote this process is defined as the *minimum ignition energy*, or simply MIE. Due to the stochastic character of forced ignition processes, the experimental evaluation of MIE involves a probabilistic approach. In a premixed and homogenous system, this behaviour is mainly explained by the randomness of the spark itself [Phuoc, 2006; Mastorakos, 2009], while in turbulent non-premixed systems, turbulent velocity fluctuations [Chakraborty et al., 2007] and concentration fluctuations [Birch et al., 1981], for example, add another layer of randomness to the process. Due to the stochastic nature of ignition, an experimental evaluation of MIE in sprays relies on the definition of the *probability of ignition*, P_{ign} [Aggarwal, 1998], defined as the ratio of successful ignition events to the total number of ignition attempts by the spark. Thus, MIE is often evaluated in experiments for an ignition probability of 50% [Danis et al., 1988; Ko et al., 1991; Aggarwal, 1998].

While the concept of MIE is in itself simple, and standards exist for evaluating MIE in quiescent mixtures [ASTM Standard D7566-16, 2013], its evaluation in spray flows is not straightforward. A number of factors contribute to the lack of consistency in the evaluation of MIE between different authors. First, experiments are carried out in different configurations, hence ignition of the whole combustor is subjected to burner-scale effects. Due to that, MIE can be more precisely defined if evaluated based on the *probability of establishing/generating a kernel*, P_{ker} [Mastorakos, 2017]. In this definition, a successful event consists simply in the generation of a small propagating flame rather than including further propagation of the flame and its stabilisation, leading to full ignition of the burner. Nevertheless, this definition also allows for different interpretations, as "establishment" and "generation" of the flame kernel are terms that are used interchangeably and are loosely defined, as is the term "flame kernel" itself.

The difficulty in defining the different probabilities of ignition accurately is acknowledged by Mastorakos [2017], who states that "*the boundaries between these phases,* [i.e., kernel generation, flame growth, and burner ignition] *are not always clear and this is amply manifested by the different interpretations given to the term ignition in the*

literature." In practical terms, a *flame kernel* is often considered as the region resulting from the action of the spark. Thus, the *kernel generation phase* has been conveniently defined as the part of the ignition process occurring over a length scale of the same order of the spark size [Mastorakos, 2017]. Consequently, the *flame growth phase* comprises the process occurring at larger length scales and time scales, comparable to the integral length scale of the flow and some bulk flow-related time scale, while the *burner ignition phase* is combustor specific and depends on the interaction of the flame with the flow at the combustor scale and its eventual stabilisation [Mastorakos, 2017].

In the kernel generation phase, the type of spark dictates the power and volume in which energy is deposited in the mixture. To put it simply, energy deposition is usually achieved through a breakdown process, where ionisation of gas occurs due to electrons striking the gas molecules. In a typical electric spark, this is achieved over relatively long periods (up to a millisecond [Lewis and von Elbe, 1961; Cardin et al., 2013]) and through a glow discharge process occurring once the voltage between the electrodes is higher than the breakdown voltage of the gas. In a nanosecond-pulse laser spark, the process is characterised by shorter time scales (up to microseconds [Cardin et al., 2013; Mulla et al., 2016; Gebel et al., 2015*b*]) and starts by absorption of photons by a few gas molecules (multi-photon ionisation). This process releases electrons that, in turn, absorb more photons, thus leading to a cascade effect (i.e., cascade ionisation by inverse bremsstrahlung) and an electron avalanche resulting in breakdown of the gas [Phuoc, 2006]. As a result of the breakdown process, a highly reactive and high-temperature plasma grows and immediately starts to cool [Phuoc, 2006]. The plasma is marked by strong H_α emissions and eventually transitions to a hot gas, which continues to cool and is marked by a significant decrease in radical emissions such as OH* and CH* [Beduneau et al., 2009; Gebel et al., 2015*b*]. In cases where a spark leads to the establishment of a kernel, a sudden rise of these radicals is observed between 300-800 µs, indicating the beginning of branching phenomena [Beduneau et al., 2009]. Thus, by monitoring the mean OH* intensity in the flame kernel as it grows, a time scale characteristic of the net increase of chain-branching reactions in the kernel can be defined [Cardin et al., 2013].

Although successful flame kernels tend to present high H_α emissions in the plasma phase [Beduneau et al., 2009; Mulla et al., 2016], it is still not clear how and which radicals in the initial phase of the plasma affect the formation of the kernel. Overall, to understand the kernel generation phase, insight can be drawn from autoignition [Aggarwal, 1998; Mastorakos, 2017], as failure to establish a kernel is usually attributed

to factors leading to a slow autoignition process [Mastorakos, 2017]. This includes, for example, low temperatures resulting from a weak spark or simply a mixture that is locally too lean. In this phase, failure to establish a flame kernel is defined as the *short mode of ignition failure* [Mastorakos, 2017]. As a general rule, in order to successfully establish a kernel in a flammable mixture, the energy deposited in the mixture must be concentrated in a region with size of the order of the laminar flame thickness, raising its temperature to the adiabatic flame temperature [Spalding, 1979]. Once a flame kernel has been established, it may still quench as a result of excessive heat loss. Thus, the resulting rate of energy released through combustion must be enough to overcome the rate of heat loss from the kernel to the surrounding flow, allowing the flame kernel to develop into a self-sustained propagating flame [Lewis and von Elbe, 1961]. This phase is defined as the flame growth phase, and failure of establishing a self-sustained flame at this phase is defined as the *long mode of ignition failure* [Mastorakos, 2017].

2.1.2 Minimum ignition energy

The effect of droplets on MIE was systematically investigated for the first time in a series of experimental and analytical works by Ballal and Lefebvre concerning quiescent mixtures [Ballal and Lefebvre, 1978*b*,*a*, 1979] as well as spray flows [Ballal and Lefebvre, 1979, 1981*a*]. In these works, an MIE model was developed based on the assumption that ignition depends on the evaporation of fuel by the spark leading to an optimal fuel vapour concentration, and that the time required for a kernel to quench by energy losses to the surrounding flow is equal to the time necessary for evaporation and reaction to take place. Experiments were performed with lean to stoichiometric mixtures of various fuels, and a spray Sauter mean diameter (SMD) generally between 30–150 µm[1].

To ensure an absolute minimum ignition energy, an optimisation of the spark gap was carried out for every test condition following the initial results presented in [Ballal and Lefebvre, 1978*b*]. The presence of an optimum spark gap minimising the ignition energy was explained as a combination of two main effects [Ballal and Lefebvre, 1978*b*]: decreasing the spark gap width resulted in an enhancement of the quenching effect caused by the spark electrodes, while increasing the gap width led to larger kernels which were detrimental to ignition due to their possible lower temperature [Ballal and Lefebvre, 1978*b*]. A strong dependence of the optimal spark gap width with the atomisation degree of the fuel was also present. This was discussed in terms of the

[1]Droplet size measurements were limited to 20 µm at the lower end due to the light-scattering measurement technique used [Lorenzetto and Lefebvre, 1977]

quenching distance of the spray, but could potentially be related to fuel fluctuations as discussed by Mastorakos [2009, 2017] and a possible reduction of the local flammability of the mixture, as defined by [Birch et al., 1979], as the spark volume decreases.

Overall, increasing the SMD and reducing the overall equivalence ratio and fuel volatility was found to have a negative impact on MIE [Ballal and Lefebvre, 1978*b*,*a*, 1979]. In a turbulent flow, an increase in bulk flow velocity (with turbulence levels $u^{'}/U_b$ of approximately 2–3%) was also detrimental to MIE, an effect that was attributed to the intensification of heat transfer from the kernel to the fresh mixture through convenction [Ballal and Lefebvre, 1979, 1981*a*]. This behaviour was successfully captured in the model, initially proposed by Ballal and Lefebvre [1978*a*] and later updated to quiescent as well as flowing sprays [Ballal and Lefebvre, 1979], and to include a smooth transition from gaseous to partially prevaporised gas-liquid mixtures [Ballal and Lefebvre, 1981*a*]. The minimum ignition energy is given as [Spalding, 1979],

$$E_{min} = c_{p,a}\rho_a \Delta T_{st} \frac{\pi}{6} {d_{\mathrm{q}}}^3, \tag{2.1}$$

where c_p is the specific heat at constant pressure, ρ is the density, ΔT_{st} is the rise in temperature relative to the stoichiometric adiabatic flame temperature, and the subindices a and f denote air and fuel, respectively. The quenching distance, d_{q}, in turbulent spray flows is given as [Ballal and Lefebvre, 1981*b*],

$$d_q = \frac{0.32 \mathrm{Pr} \rho_f}{Z\phi \log\left(1+B_{st}\right)} \sqrt{\frac{u' {d_{32}}^3}{\rho_a \mu_a}} + \frac{10\alpha}{S_{\mathrm{T}} - 0.63u'}, \tag{2.2}$$

where Pr is the Prandtl number, μ is the dynamic viscosity, ρ is the density, α the thermal diffusivity, and S_{T} is the turbulent burning velocity for the spray. The parameter B is the Spalding mass transfer number [Spalding, 1979], which represents a measure of mass transfer potential and fuel volatility, and Z is defined based on various averages of droplet size evaluated experimentally [Ballal and Lefebvre, 1981*a*].

An additional model based on the characteristic time approach of Ballal and Lefebvre [1978*a*] was later developed for quiescent mixtures by Peters and Mellor [1980], who introduced concepts of flame stabilisation and an additional modification of the evaporative time scale. This and the model by Ballal and Lefebvre [1981*a*] were evaluated in the experimental work of Danis et al. [1988], which showed that both models performed similarly, but under-predicted MIE for lean and finely atomised (d <30 μm) spray flows.

As discussed, the concept of minimum ignition energy applied to sprays systems implies that, in order to raise the temperature of the mixture, the spark needs to account for the extra energy required for the evaporation of the fuel [Ballal and Lefebvre, 1978*a*]. Thus, it is not surprising that experiments focusing on the effects of global spray parameters on MIE have shown that increasing the amount of prevaporised fuel or varying any parameters of the two-phase flow or mixture in order to enhance evaporation of the droplets will normally lead to a decrease in MIE [Ballal and Lefebvre, 1978*b*,*a*, 1979, 1981*a*; Singh and Polymeropoulos, 1988; Danis et al., 1988; Dietrich et al., 1991]. Nevertheless, what is revealing about the nature of the ignition process, and has been shown both analytically [Aggarwal and Sirignano, 1985; Singh and Polymeropoulos, 1988] and experimentally [Singh and Polymeropoulos, 1988; Danis et al., 1988], is that the lowest MIE in a spray may be actually found for droplets with an intermediate size.

An optimum droplet size for minimum ignition energy was first verified in the experiments of Singh and Polymeropoulos [1988], although the phenomenon was observed in flame propagation experiments since Burgoyne and Cohen [1954]. Singh and Polymeropoulos [1988] verified in a rich mixture a quadratic behaviour of MIE in respect to droplet size, with a minimum occurring at approximately 25 μm. To explain this behaviour, a model for transient droplet evaporation due to the spark was used, showing that the effective amount of vapour resulting from the spark depends on the droplet size: small droplets may result in a very rich mixture in the centre of the kernel, being detrimental to ignition, while intermediate droplets may give rise to a stoichiometric mixture, enhancing ignition [Singh and Polymeropoulos, 1988]. Moreover, Danis et al. [1988] also reported the presence of an optimum droplet size effect, claiming its occurrence between 10–30 μm for both lean to stoichiometric mixtures. It should be noted that no experimental data was available for these conditions, and looking closely at the results, one may clearly see that only a positive correlation between ignition energy and droplet diameter was verified (between 30–50 μm). Still, in comparison to MIE data available for fully prevaporised mixtures, Danis et al. [1988] observed that the presence of the smallest droplets may decrease MIE in comparison to a gaseous mixture, and that this effect is enhanced as the overall mixture becomes leaner. Furthermore, the importance of the resulting gaseous equivalence ratio was also highlighted in the numerical work of Aggarwal and Sirignano [1985], who also verified the possibility of a lower MIE in a spray, in comparison to an equivalent gaseous mixture.

Some aspects of the works by Singh and Polymeropoulos [1988] and Danis et al. [1988] are worth noting. First, an actual optimum droplet size leading to MIE was only directly observed in rich conditions by Singh and Polymeropoulos [1988]. Other works, including the experiments of Ballal and Lefebvre, considered only lean to stoichiometric conditions. Second, the presence of droplets was verified to lead to a lower MIE if compared to fully-prevaporised cases in lean to stoichiometric mixtures. This effect increased as the mixtures became leaner [Danis et al., 1988]. Third, the criterion for successful ignition used to evaluate MIE in the previously-mentioned works considered not only the formation of a kernel, but its growth into a "large" flame that propagated into the fresh mixture. That is, the effects of the droplets on flame propagation were also taken into account; this is discussed in Sec. 2.2. Other than the works discussed previously, the reader may refer to the extensive review provided by Aggarwal [1998] for more detail on the present issue, as well as a broad discussion on the effects of global spray parameters on autoignition and forced ignition of sprays. Further, Annamalai and Ryan [1992] review works dealing with combustion and ignition of droplet groups, while single-droplet ignition has been reviewed more recently by Aggarwal [2014].

2.1.3 Stochastic behaviour

To explain the existence of an optimum droplet size for MIE, Aggarwal and Sirignano [1985] also presented a preliminary account of the stochastic nature of spray ignition through 1-D unsteady droplet-scale calculations. In their work, the ignition behaviour of droplets close to a heated wall was found to be strongly dependent on their location in relation to the ignition source and, consequently, to the resulting fuel concentration inhomogeneities arising from the evaporation process. This idea would be later revisited at much greater level of detail by a number of works using 3-D direct numerical simulations (DNS) to explore the ignition behaviour of spherically-expanding flames – a topic that has been recently addressed in the review by Mastorakos [2017].

DNS works have shown the importance of droplet evaporation following the deposition of energy to the outcome of an ignition attempt. Using one-step chemistry and homogenous isotropic decaying turbulence, ignition in a uniform droplet mist [Wandel et al., 2009] and in a droplet-air mixing layer [Neophytou et al., 2010] was attributed to the generation of a mixture with optimum equivalence ratio not only at the spark location, but also at its vicinity. If evaporation of the droplets surrounding the spark led to a near-stoichiometry or rich gas phase, heat release in that area was then maximised, allowing for diffusion of energy to its surroundings and further evaporation

of the droplets. The presence of fuel inhomogeneities is known to enhance ignition in lean gaseous mixtures [Chakraborty and Mastorakos, 2008], and their presence may even allow ignition when the spark is placed in the air side of an air-droplets mixing layer, given that enough energy diffused from the spark reaches an optimum mixture [Neophytou et al., 2010].

Further, the ignition process was described by Neophytou, Mastorakos and Cant [2011, 2012] in detailed-chemistry simulations in terms of the evolution of profiles of heat release and species in the mixture fraction space. During the deposition of energy by the spark, the fuel breaks up leading to mostly endothermic reactions, followed by a peak in heat release at low mixture fractions at the end of the spark. Following the spark, in dense sprays, the energy released allowed for further evaporation of droplets and establishment of a non-premixed type flame, with most of the heat release concentrated around large slowly-evaporating droplets close to the ignition source. In contrast, in dilute sprays, ignition of the kernel was allowed by much lower heat release rates occurring at lean mixture fractions, even below the lower flammable limit. This is discussed further in Sec. 2.2.

In contrast to the ignition cases, Wandel et al. [2009] observed quenching of the flame kernel if the amount of fuel vapour at the spark location was particularly low, below the lower flammable limit, either due to a small number of droplets in that region or due to their large size. This occurred in two particular ways. First, the lack of flammable mixture following the energy deposition was such that it was insufficient to initiate combustion in the kernel. In relation to the flame time scale of the simulations (i.e., the ratio of the laminar flame thickness to the laminar burning velocity), that characterised a short mode of ignition failure as defined by Mastorakos [2017]. Second, combustion was initiated following the spark. However, reaction occurred in lean regions, hence the resulting heat release was too low to overcome evaporation in the surrounding mixture, leading to the failure of the kernel due to fuel starvation. In a later work, Wandel [2014] also verified that intense droplet evaporation in the flame kernel following the spark could lead to ignition failure, in contrast to previous findings. This occurred in cases where most of the oxidiser had been consumed in the flame kernel, but continued evaporation of a single droplet without localised non-premixed type of reaction led to an intense heat-sink effect due to evaporative cooling, preventing the flame from propagating in all directions and resulting in its extinction [Wandel, 2014]. Such extinction modes subsequent to the start of combustion characterise a long mode of ignition failure [Mastorakos, 2017].

In addition to DNS, experiments which explored the stochastic features of the process have been limited to complex geometries and investigated the burner-scale aspects of the problem, that is, the interaction of an established flame kernel with the main flow [Ahmed and Mastorakos, 2006; Ahmed et al., 2007; Letty et al., 2012; Peterson et al., 2011; Mosbach et al., 2010; Cordier et al., 2013; Peterson et al., 2014; Hendershott et al., 2018]. Still, canonical experiments with uniform spray and turbulent conditions in which the early-phase ignition behaviour of a kernel is observed have not yet been carried out.

2.1.4 Laser ignition

The early phase of the ignition process using non-resonant laser sparks consists of the breakdown of the mixture, growth and subsequent cooling of the plasma, and transition of the plasma into a flame kernel, as discussed previously in Sec. 2.1.1. This type of ignition has been suggested as an alternative to increase the ignitability of engines, since the spark can be positioned in regions of the flow that are most prone to ignition [Mastorakos, 2017]. It may also allow for a real-time assessment of the mixture's characteristics by using the laser-induced breakdown spectroscopy technique (LIBS) for equivalence ratio measurements [Kotzagianni et al., 2016]. The fundamentals of laser ignition techniques and all its variants are discussed in the comprehensive review by Phuoc [2006], and a full account of the applications of laser ignition towards new spacecraft and aircraft technologies is presented by O'Briant et al. [2016]. In this section, some of its particular features that are relevant for ignition of sprays are briefly discussed.

Droplets may interact with the laser spark in several ways. One example is the presence of large droplets at the focus point of the laser beam, which may act as an additional lens facilitating the breakdown of the gas, thus decreasing the threshold energy [Müsing et al., 2007]. At the same time, the presence of droplets along the beam path scatters the laser, attenuating the beam and decreasing the total energy delivered at the ignition point [El-Rabii et al., 2005]. Additionally, heating and subsequent explosive boiling of droplets is also possible along the beam, but only for very high fluence levels of the order of $100\,\mathrm{J/mm^2}$ [Pinnick et al., 1990]. For typical energy levels used in ignition, droplet evaporation mostly occurs in the hot gas following the plasma, in addition to droplets that promptly evaporate in the plasma itself [Lee et al., 2016]. As discussed by Beduneau et al. [2009] and Cardin et al. [2013] in the context of gaseous mixtures, the composition of the plasma may affect ignition, although the

transition from plasma to flame kernel is not well understood. Through experiments with kerosene droplets, Gebel et al. [2015*b*] suggested that CH* is formed in the plasma by combustion chain-reactions, where the reactants originate from a radical pool formed in the process of cooling of the plasma through recombination processes.

Additionally, the shockwave that is formed following the laser pulse can also impact ignition. As it propagates towards the fresh mixture, a shock wave can promote breakup of large droplets (of approximately 100 µm) up to a few millimetres away from the focus point of the laser [Gebel et al., 2013, 2015*a*]. Due to the gas-dynamic effects arising from the formation of the shockwave and its interaction with the plasma, the flame kernel is characterised by a toroidal shape and also by the presence of an additional (third) lobe in the direction of the laser [Spiglanin et al., 1995; Bradley et al., 2004]. Such gas-dynamic effects were found to enhance flame propagation up to approximately 1 ms in experiments with gaseous mixtures and a high-energy 200-mJ laser spark [Bradley et al., 2004]. The transition from plasma to flame kernel was also investigated in gaseous mixtures by Mulla et al. [2016], who verified the decay of the H_α emission signal in the plasma due to a 140-mJ spark was of the order of 1 μs, while the subsequent process involving quenching or ignition of the kernel was observed using OH PLIF and found to be of the order of 1 ms.

Overall, in comparison to electric sparks, the minimum ignition energy in experiments with laser sparks is usually higher due to the extra energy required to create the plasma and, especially, due to the energy that is carried by a shock wave formed by the sudden expansion of the plasma [Weinberg and Wilson, 1971]. In order to obtain the amount of energy that is transferred to the flame kernel, blast wave analysis together with schlieren visualisation of the shock wave have been recently used in experiments with constant-volume bombs operating with gaseous fuels [Bradley et al., 2004] and sprays [Lawes et al., 2007]. Even though the ignition energies were found to be usually higher with a laser-spark, its capability of improving (full-burner) ignition by initiating a flame in regions close to the spray injection and near recirculation zones, and preferably with ideal mixture conditions and small droplet sizes, has been observed in spray-injection swirl-stabilised burners operating with air-methane and kerosene [Moesl et al., 2009], n-heptane [El-Rabii et al., 2005; Marchione et al., 2009; Letty et al., 2012], ethanol [El-Rabii et al., 2004; Letty et al., 2012], and methanol [El-Rabii et al., 2004].

2.2 Flame propagation in sprays

The growth of a flame kernel into a self-sustained flame is an essential part of the ignition process. As previously discussed, following the growth and cooling of the kernel and the predominance of chain-branching over recombination reactions, successful ignition depends solely on the propagation of the flame into the fresh mixture. The presence of droplets in the flow and their interaction with the flame, turbulence, as well as with each other, increases the complexity of this propagation-controlled phase and, therefore, must be considered.

2.2.1 Flame speed

Some of the fundamental ideas concerning the propagation of a flame in a spray were first introduced in the early experimental work of Burgoyne and Cohen [1954]. In that work, the authors observed that the size of the droplets played an important role in determining the propagation characteristics of a tetralin spray flame: "*below 10 μm the suspension behaves like a vapour, but above 40 μm the drops burn individually, in their own air envelope, and one burning droplet ignites adjacent ones, thus spreading combustion. At intermediate sizes, behaviour is transitional.*" [Burgoyne and Cohen, 1954].

Following the work of Burgoyne and Cohen [1954], a number of experiments generally verified a decrease in flame speed in the presence of droplets, in comparison to a gaseous mixture of the same equivalence ratio [Čekalin, 1961; Mizutani and Nishjmoto, 1972; Mizutani and Nakajima, 1973*b*,*a*; Polymeropoulos and Das, 1975; Hayashi et al., 1977; Ballal and Lefebvre, 1981*b*; Myers and Lefebvre, 1986; Richards and Lefebvre, 1989; Nomura et al., 2007; Mikami et al., 2009; Lawes and Saat, 2011]. Similarly to what has been discussed by Ballal and Lefebvre [1979] in the context of spark ignition, the detrimental effect of droplets was attributed to the extra energy released by the flame required to vaporise the fuel droplets at the flame front and, most importantly, to the long evaporation time scales of the droplets [Ballal and Lefebvre, 1981*b*]. Thus, the same notion discussed for ignition applies: decreasing fuel prevaporisation or evaporation rates is generally detrimental to flame speed.

Nevertheless, similarly to the presence of an optimal droplet size leading to MIE in sprays, it has been found that the speed of a self-sustained flame across a droplet mist can also be maximum for a specific value of droplet size, which usually occurs between 10–30 µm, approximately. This was verified in experiments with uniform

droplet dispersions in three types of geometries: constant-volume bombs [Hayashi et al., 1977; Nomura et al., 2007], channels [Mizutani and Nishjmoto, 1972; Mizutani and Nakajima, 1973*b*; Myers and Lefebvre, 1986; Richards and Lefebvre, 1989; Burgoyne and Cohen, 1954], and piloted-stabilised v-shape flames [Čekalin, 1961; Polymeropoulos and Das, 1975]. Additionally, flame speeds higher in sprays than in a premixed gaseous mixture with the same equivalent ratio have been verified both in rich n-octane and ethanol sprays [Hayashi et al., 1977] and lean ethanol sprays at high pressure [Nomura et al., 2007].

The enhancement of flame speed has been mostly attributed to the occurrence of regions of optimum equivalence ratio (i.e., close to stoichiometry) formed in the inter-droplet space [Mizutani and Nakajima, 1973*a*; Polymeropoulos and Das, 1975; Hayashi et al., 1977; Richards and Lefebvre, 1989]. Thus, Hayashi et al. [1977] defined an effective fuel-air ratio which controls flame propagation and takes into account only the fuel vapour available at the flame front, that is, does not consider the remaining fuel in droplets surviving the flame. Wrinkling of the flame caused by the droplets was also suggested as a factor enhancing the flame speed in sprays [Mizutani and Nakajima, 1973*a*; Hayashi et al., 1977]. Further, an alternative hypothesis to explain this effect was suggested by Myers and Lefebvre [1986], which consisted in micro-explosions occurring in the flame front in multicomponent hydrocarbon fuels: superheated vapour trapped inside the fuel droplets due to different boiling points between the components would be released in large quantities at the flame front, causing microexplosions and unusually high flame speeds [Myers and Lefebvre, 1986]. Interestingly, Myers and Lefebvre [1986] also suggested that high flame speeds in the presence of fine droplets could be related to increase in turbulence generated by the air-blast atomisers; these are used in channel flow and v-shape flame experiments, as opposed to the method of condensation of super-heated vapour. Moreover, the enhancement effect of droplets was suppressed in cases where the liquid fuel was injected as a very fine mist [Mizutani and Nakajima, 1973*a*; Polymeropoulos and Das, 1975], resulting in excessive evaporation of the droplets leading to a rich inter-droplet region [Richards and Lefebvre, 1989].

Based on the afore-mentioned experimental works, the flame speed was modelled based on the assumption that propagation is such that the quench time scale of the reaction zone is equal to the sum of the evaporation and chemical time scales [Polymeropoulos, 1974; Ballal and Lefebvre, 1981*b*]. The model developed by Ballal and Lefebvre [1981*b*] was later improved by Polymeropoulos [1984] assuming that propagation may occur as a combination of individually burning droplets and homogenous

reaction in a gaseous mixture, which was then introduced by using a criterion for individual droplet burning at the flame front. Thus, the rate of heat release in the flame was modelled as the heat release due to individual droplet combustion, if it occurs, in addition to the heat release due to the homogenous combustion of the gaseous mixture. The resulting equation for flame speed [Polymeropoulos, 1984] is,

$$S^2 = \left\{ \frac{(1-\Omega)\,{d_\mathrm{f}}^2}{12{\alpha_g}^2 d^2 \ln(1+B)} \frac{\rho_l}{\rho_g} + \frac{1}{{S_\mathrm{L}}^2} \left[1 - \left(\frac{d_\mathrm{f}}{d} \right)^3 (1-\Omega) \right] \right\}^{-1}, \tag{2.3}$$

where Ω the degree of prevaporisation, α is the thermal diffusivity, d_f is the droplet size at the flame front. For complete vaporization, or $d_\mathrm{f} = 0$, Eq. 2.3 gives $S = S_\mathrm{L}$. The resulting model exhibited a good fit with the experimental data of Ballal and Lefebvre [1981*b*], while reproducing the effect of flame speed enhancement verified by Burgoyne and Cohen [1954] with small droplets ($d \leq 40\,\mu$m).

2.2.2 Propagation mechanisms

Three distinct propagation modes may be defined for a flame propagating across a droplet dispersion. The first mode, normally occurring in the presence of large droplets, is characterised by a flame relay mechanism where one individually burning droplet ignites other surrounding droplets. This mechanism was first described by Čekalin [1961] and elaborated further by Mizutani and Ogasaware [1965] based on experimental observations and macro-scale photographs and shadowgraphs of the flames. A second propagation mode occurs when droplets are small enough so that they evaporate and mix ahead of the flame, giving rise to a behaviour similar to the one of a gaseous premixed flame [Burgoyne and Cohen, 1954]. Finally, a transition mode takes place for a wide range of droplet sizes, having the main features of the two other propagation modes [Burgoyne and Cohen, 1954], that is, individually burning droplets as well as the presence of homogenous reaction occurring in the inter-droplet space, either due to rapidly evaporating droplets or due to the presence of prevaporised fuel [Čekalin, 1961; Mizutani and Ogasaware, 1965].

As a result of the normally long droplet evaporation time scales in respect to the chemical time scales (except in the gaseous-like propagation mode), the resulting equivalence ratio at the reaction zone is often understood as the main parameter controlling flame propagation [Hayashi et al., 1977]. This effect was explored in detailed-chemistry laminar flame calculations [Neophytou and Mastorakos, 2009] where the

highest flame speed was observed for an effective equivalence ratio near stoichiometry, which occurred either for small droplets in overall lean sprays or large droplets in overall rich sprays. Similar findings which corroborated the results of the experiments discussed in Sec. 2.2.1 were obtained by Rochette et al. [2019] in global two-step chemistry laminar flame calculations, by Nicoli et al. [2015, 2016] in 2-D single-step chemistry calculations, and in 3-D single-step [Wandel et al., 2009; Neophytou et al., 2010; Wacks et al., 2016] and detailed-chemistry [Neophytou, Mastorakos and Cant, 2012] DNS of spherically expanding flames. An empirical correlation for the evaluation of the laminar burning velocity of the spray was presented by [Neophytou and Mastorakos, 2009], while Rochette et al. [2019] presented a set of analytical equations that can be used for weakly and fully evaporation controlled flames.

The fact that large and low volatility droplets have long evaporation times leading to a gas phase at the flame front leaner than the overall mixture means that such droplets must survive the flame, reaching the burnt products side. Evidence of this effect in spherically expanding flames has been verified in experiments with schlieren [Bradley et al., 2014] and by tracking the sudden change of velocity of ethanol droplets as they crossed the flame [Thimothée et al., 2017]. In DNS of spherically expanding flames, droplet penetration and subsequent evaporation in the products side was observed, leading to an additional influx of fuel towards the flame front [Wandel et al., 2009; Neophytou et al., 2010; Wacks et al., 2016]. In overall rich conditions, an absence of oxygen and, therefore, of combustion has been verified in the burnt products [Neophytou and Mastorakos, 2009; Nicoli et al., 2016]. Yet, due to the high temperatures in that region, evaporation of surviving droplets led the pyrolysis of the fuel, resulting in hydrogen and acetylene generation which diffused back to the flame front and contributed to the acceleration of the flame [Neophytou and Mastorakos, 2009; Neophytou, Mastorakos and Cant, 2012]. The phenomenon of droplets surviving the flame was investigated from the perspective of the relative velocity between the droplet and the flame by Greenberg [2007], observing that the long residence time of the droplets in the reaction zone may cause flame extinction due to enhanced evaporative cooling in that reaction zone leading to a strong heat-sink effect. The same effect was later observed in DNS [Wandel, 2014] and in experiments with stabilised flames by Verdier et al. [2018].

It is well known that the presence of droplets may also promote wrinkling of the flame surface, leading to a higher surface area and, therefore, higher burning velocity. This effect was first observed in direct photographs by Mizutani and Nakajima [1973*a*] and

through schlieren by Hayashi et al. [1977], who suggested that strong evaporative fluxes occurring at the flame front could add to the total turbulence of the flow and, therefore, be the cause of flame wrinkling. Neophytou, Mastorakos and Cant [2012] showed that mixture inhomogeneities alone, in addition to turbulence, can generate such effect in the presence of inter-droplet flame propagation. This effect was found to be more pronounced in lean mixtures, as the isosurface of local of stoichiometric equivalence ratio is located close to the droplet surface for such cases [Neophytou et al., 2010]. Additionally, larger droplets in a dilute spray can give rise to a significantly wrinkled flame, occurring due to localised droplet-scale reaction zones. Further, Thimothée et al. [2017] observed the development of a cellular flame pattern in ethanol droplets with sizes between 5–23 μm – that is, in the presence of strong evaporation at the flame front – and attributed this effect to the triggering of Darrieur-Landau instabilities caused by droplet perturbations once these survived the flame. The contribution of droplet-induced flame curvature has been observed in 3-D DNS of n-heptane spray flames and its magnitude directly correlated to the droplet size, although this effect may be eclipsed as turbulence increases [Ozel Erol et al., 2018, 2019].

As a result of the contribution of droplets to stretch due to strain and curvature at the droplet-scale [Wacks and Chakraborty, 2016], it is expected that spray flames may extinguish at global Karlovitz numbers that differ from those verified by Abdel-Gayed and Bradley [1985] in premixed flames. Evidence of this effect has been seen in bluff-body stabilised spray flames [Cavaliere et al., 2013] and swirl-stabilised spray flames [Yuan et al., 2018], where extinction of the flames was observed at values between 0.8 and 1.2 for a range of fuels, in comparison to 1.5 for gaseous premixed flames. Additionally, Verdier et al. [2018] visualised local events of flame extinction led by large droplets approaching the reaction zone of a lifted flame in a hollow-cone spray injector. Local extinction was attributed either due to the heat-sink effect occurring in the evaporative cooling of the fuel, or due to the large rich region surrounding the droplet as a result of evaporation, similarly to the mechanisms verified by Wandel [2014] in DNS of spherically expanding flames.

Moreover, spray flames have been observed to exhibit both premixed and non-premixed characteristics, with reaction occurring in a wide range of mixture fractions [Wandel et al., 2009; Wacks et al., 2016]. While small droplets fully evaporate in the pre-heating zone, leading to premixed combustion mode, localised diffusion flames surround large droplets [Wacks et al., 2016]. In fact, this phenomenon has been observed by Neophytou, Mastorakos and Cant [2012] to allow for the droplet ignition

relay mechanism proposed based on flame visualisations [Čekalin, 1961; Mizutani and Ogasaware, 1965]. Still, Neophytou, Richardson and Mastorakos [2012] verified that the diffusion of heat and species occurring around individually burning droplets not only ignited neighbouring droplets, but also allowed for a slowly reacting gas phase in the inter-droplet space marked by very low heat release levels. This phenomenon was observed even for conditions of low equivalence ratio of the inter-droplet space, below the flammability limit. This mechanism of propagation occurred in dilute sprays while a transition mode occurred in dense sprays, where the increased evaporation rates lead to a flammable region ahead of the flame, resulting in a more homogenous front.

Finally, the group combustion theory proposed by Chiu and Liu [1977]; Chiu et al. [1982] was used by Neophytou, Mastorakos and Cant [2012] to assess the propagation mode of a spray flame, distinguishing between a dilute and a dense spray. Although this has been proposed for combustion of droplet clouds, some features of spherically expanding flame propagation seem to be represented in this theory. A spray group number may be defined, G, which represents the ratio of the rate of droplet evaporation to the transport of gaseous species by diffusion [Chiu et al., 1982]. For a dilute spray ($G < 10^{-2}$) this model predicts the individual burning of the droplets. As G increases and the spray becomes denser, the mode changes from single-droplet combustion to group combustion, in which the droplets evaporate creating a radial flux of fuel vapour transported outwards the cloud and then mixing with air. In the internal group combustion mode ($10^{-2} < G < 10^{-1}$), a flame separates the core of evaporating droplets from an external region of individually burning droplets. As the size of the core increases, the flame surrounds the whole cloud, defined as the external combustion mode ($10^{-1} < G < 10^{2}$). A fourth mode of high G is also possible, where the flame is located even further from the evaporating droplet cloud, while a core of non-evaporating droplets exists at the centre of the cloud ($G > 10^{2}$). This theory also applies to a flow to a certain extent; any convective effects are assumed to lower the G values where transition from mode to mode occurs [Annamalai and Ryan, 1992]. The spray's group number is given as [Chiu and Liu, 1977],

$$G = 3\left(1 + 0.276\,\mathrm{Re}_\mathrm{d}^{1/2}\,\mathrm{Sc}^{1/3}\right)\mathrm{Le}\,N^{2/3}\,(d/l_\mathrm{d}) \tag{2.4}$$

where Re_d, Sc and Le are the droplet Reynolds number, the Schmidt number, and the Lewis number of the gas, respectively, and d is the droplet diameter, N the number of droplets in the cloud, and l_d is the mean droplet spacing.

2.3 Specific objectives

Ignition and flame propagation are inherently transient processes, significantly affected by long evaporation times of fuel droplets and the resulting fuel concentration inhomogeneities arising from their evaporation. Thus, to understand the complex behaviour of initiation of a spray flame in a real combustor, attention must be given to the phenomena occurring at the most fundamental time scales and length scales of the process. These issues are discussed in three parts of this thesis. The first part investigates the *stochastic nature of ignition* of sprays by focusing on the establishment of a flame kernel and its transition into a self-sustained flame (Chapter 5). Then, *flame propagation mechanisms* in sprays are studied in light of droplet-scale visualisations of the flame (Chapter 6). Finally, some of the fundamental ideas and results of the first two parts are applied to *low-order modelling of ignition* of aviation gas-turbine combustors (Chapter 7).

The first part of this work aims at characterising the stochastic behaviour of the early phase of ignition. As shown in DNS, the local mixture at the spark location strongly impacts the outcome of a single ignition event. Still, it is not clear how mixture fluctuations arising from the random position of droplets can affect ignition probabilities and MIE, as it is impractical to use DNS to obtain a statistically significant assessment of the process. Although experiments in canonical spray flow configurations can be used to this end, no works so far have focused on the effects of global spray and spark parameters on early-phase ignition behaviour [Mastorakos, 2017]. Additionally, by modelling the spark as a high-temperature gas, simulations have also shown that the effects of the spark on temperature and on heat release in the flame kernel may be long-lasting. Recent experiments in gaseous mixtures also suggest a long-lasting effect of the spark, observed as a decay of OH* and CH* possibly formed from radicals originating from recombination reactions, then followed by a rise of these radicals due to a kick-start of chain-branching combustion reactions. These ideas may be applied to redefine the early phase of ignition. Thus, to investigate the *stochastic nature of ignition*, the objectives are as follows:

- Setup an apparatus for experiments in a canonical droplet-laden turbulent flow, allowing for the ignition and visualisation of the flame in the absence of large-scale inhomogeneities of velocity and droplet number density.

- Distinguish between the kernel generation and flame growth phases by using a straightforward, measurable time scale. Based on that, consolidate the definitions of kernel, self-sustained flame, probabilities of ignition, and time scales of ignition.

- Evaluate the effects of fuel, and global parameters of the spray and the spark on the resulting kernel size, the time scales of the spark effects, the time scales of ignition failure, and probabilities of ignition.

The second part of this work focuses on the problem of flame propagation in sprays. The prediction of the laminar and turbulent burning velocities of a spray flame based on analytical models relies on a combination of distinct propagation mechanisms. Yet, there is insufficient evidence of the propagation mechanisms of turbulent spray flames or the range of conditions at which they occur, as no experimental droplet-scale visualisation of the interaction between the droplets and the flame has been carried out until this moment. Experimental studies that attempted to measure flame speed in sprays have been mostly carried out at operating conditions chosen to ensure the continued existence of the flame, while conditions in which the flame is prone to extinguish are often not evaluated [Greenberg, 2007]. Again, these aspects of spray flames have been investigated in detail using DNS, although findings must be interpreted within the limitations of the spray and the combustion chemistry models. Thus, the effects of droplets on the *flame propagation mechanisms* in a spray and their resulting impact on flame speed are studied based on the following objectives:

- Visualise the structure of the flame and its propagation modes at the droplet scale as a function of droplet size using advanced high-speed diagnostics.

- Experimentally evaluate the flame speed and flame curvature in a self-sustained spray flame at different propagation modes.

Finally, in the third part of this work, attention is given to ignition models focusing on the propagation of the flame at the burner scale. Even under ideal atomisation conditions, the spray in a real combustor is polydisperse, leading to fuel inhomogeneities which impact on flame propagation has been discussed previously. The combination of effects such as fluctuations of flame speed and increased flame wrinkling at the droplet scale suggests that the proposed value of the Karlovitz number for flame extinction may differ in sprays, in comparison to gaseous premixed flames [Bradley et al., 2014].

SPINTHIR is a *low-order ignition model* that relies on this parameter as the flame extinction criterion. In order to improve its application to spray conditions relevant to aviation gas turbine combustion, the following specific objectives are proposed:

- Introduce a stochastic-based approach to incorporate the effects of fuel inhomogeneities arising from the polydispersity of the spray on local flammability and flame speed.
- Calibrate the extinction criterion of the model, that is, the critical Karlovitz number, directly based on experimental data from the experiments discussed in Chapters 5 and 6.
- Test the calibrated model in an aviation gas turbine combustor.

Chapter 3

Methods

The ignition experiments presented in this thesis are carried out in uniformly distributed droplet dispersions in turbulent air, where the initiation of a flame kernel is performed by means of a laser spark. Details of the burner, the laser ignition system, and the fuels used in this work are given in Sec. 3.1. Following the spark, the evolution of the flame occurs in the absence of large-scale inhomogeneities of velocity and droplet number density. The visualisation of the flame is done by using high-speed line-of-sight and laser-based diagnostics, while flow measurements are performed with a laser/phase doppler anemometry system – these are discussed in Sec. 3.2. Further, Sec. 3.3 presents a clear definition of terms used in this work (e.g., ignition probability), the experimental conditions, and the techniques used for measurements of flame speed and for the characterisation of the two-phase flow. Finally, Sec. 3.4 shows details of the low-order ignition model used for ignition prediction in complex combustors.

3.1 Apparatus

3.1.1 Burner and fuels

The experimental apparatus used in this work is shown schematically in Fig. 3.1. It consists of three fluid lines connected to a divergent-convergent tube, i.e. the burner (Fig. 3.1, item 1), where the two-phase fuel-air flow is formed. Inside the burner, a modified version of [Kariuki and Mastorakos, 2017], the liquid fuel (ethanol or a jet fuel) is atomised by an air-assist atomiser (item 2, Delavan AL-06) in the centre of the burner. Preheated air is injected from multiple holes at the bottom of the burner, passing through a pair of fine stainless-steel meshes and carrying the fuel droplets

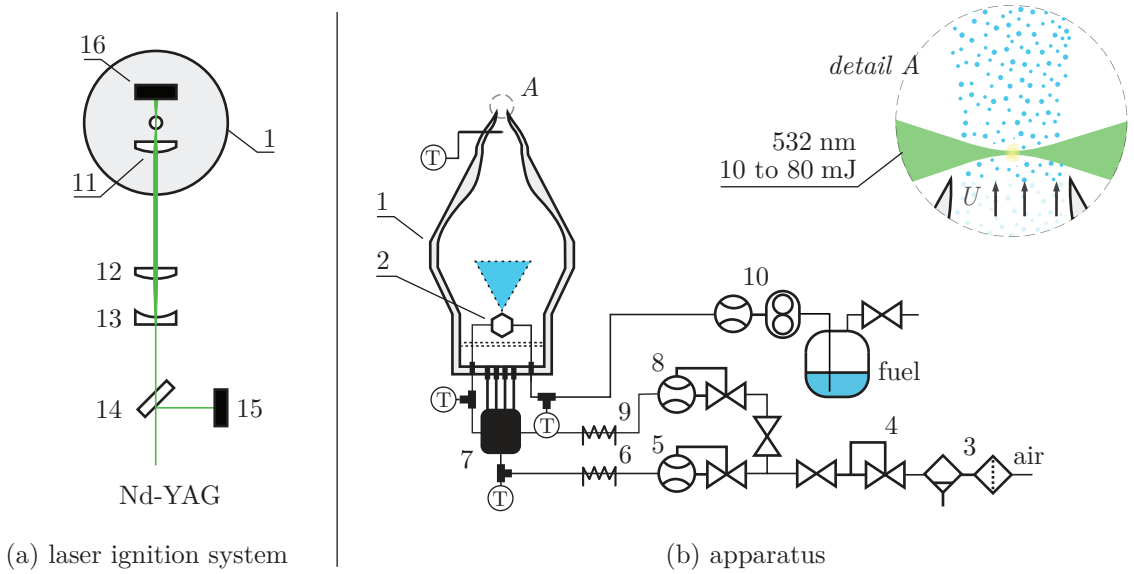

(a) laser ignition system (b) apparatus

Fig. 3.1 Schematic representation of the (a) the laser ignition system and (b) apparatus. The components of the system are: (1) burner, (2) air-assist atomiser, (3) particulate and coalescent filters, (4) pressure regulator, (5,8) flow controller, (6,9) in-line heater, (7) flow splitter, (10) Coriolis flow meter and gear pump, (11) 30-mm plano-convex lens, (12) 75-mm plano-convex lens, (13) -30-mm plano-concave lens, (14) beam-splitter, (15,16) pyroelectric energy meters.

formed at the atomiser. The mixture of fuel vapour, liquid droplets, and air, exits the burner through a 20.8-mm diameter nozzle, forming a jet. The local droplet velocity and size distribution are measured with a PDA/LDA system.

Air is obtained from a compressed-air system, filtered with particulate and coalescent filters (3), and the pressure is set with a regulator (4). The carrier air flow is set using a flow controller and an in-line heater with a PID temperature controller (5,6), and a flow splitter is used to evenly distribute the air flow at the bottom of the burner. Similarly, the atomising-air line comprises a flow controller and a temperature-controlled in-line heater (8,9). The preheating air temperature is measured in the burner, upstream of the atomiser. The liquid fuel is stored in a small reservoir at ambient temperature and pumped into the air-assist atomiser by a gear pump controlled by a Coriolis mass flow meter (10). The global equivalence ratio of the flow results from the air and fuel mass flow rates which are independently set for each test condition.

In the first part of this work (Chapter 5), the stochastic behaviour of ignition processes is studied through experiments mostly carried out with ethanol, although some data for a lower-volatility fuel, Jet A, is also provided. Additionally, in the second part, (Chapter 6) jet fuels are selected to study the effect of droplet size on the flame propagation characteristics in sprays of low-volatility multi-component fuels.

Table 3.1 Thermochemical surrogate composition of the aviation fuels studied [Edwards, 2017].

Name	*Surrogate composition*	*Avg. form.*
Jet A	15% 1,2,4-trimethylbenzene (C_9H_{12}) 30% iso-dodecane ($iC_{12}H_{26}$) 20% n-undecane ($nC_{11}H_{24}$) 35% pentyl-cyclohexane ($MC_{11}H_{22}$)	$C_{11}H_{22.1}$
ATJ-8	85% iso-dodecane ($iC_{12}H_{26}$) 15% iso-hexadecane ($iC_{16}H_{34}$)	$C_{12.6}H_{27.2}$

Data for experiments with ethanol are also given. The standard Jet A was compared to the ATJ-8, a commercial renewable jet fuel derived from isobutanol through the alcohol-to-jet process. Both ATJ-8 and Jet A fuels are being studied under the United States' *National Jet Fuels Combustion Program* [Colket et al., 2017], being referred to as C-1 and A-2, respectively, following the nomenclature of the program. The fuels' thermochemical surrogate composition is shown in Table 3.1 for reference. ATJ-8 (C-1) is a fuel formed primarily of C_{12} and C_{16} iso-paraffins with 1% of aromatic content [Edwards, 2017], hence resulting in a characteristic bimodal distillation curve shown in Fig. 3.2a. Additionally, Jet A and ATJ-8 present similar thermophysical properties controlling evaporation, that is, vapour pressure, specific heat, as well as enthalpy of vaporisation of approximately 300 kJ/kg [Edwards, 2017] (Fig. 3.2). Thus, the resulting molar fraction of fuel in the gas phase is expected to be similar between experiments with the two fuels, although a minor variation of the gas-phase equivalence ratio, ϕ_g, should occur due to the difference in the fuels' average molecular formulas. Additionally, both fuels present similar laminar burning velocities, with Jet A presenting approximately 10% higher S_u° than ATJ-8 [Wang et al., 2019].

The droplet size distribution is set between a fine monodisperse-like spray and a coarse spray by adjusting the air flow rate into the atomiser while keeping constant the total air flow and the fuel flow. Thus, the droplet size is adjusted independently of the overall equivalence ratio of the mixture. A detailed characterisation of the spray is presented in Sec. 3.3, showing that the resulting Sauter mean diameter (SMD) was between 16 and 33 µm. The preheating temperature of the air is set to 30 °C and 100 °C for the ethanol and jet fuel experiments, respectively, resulting in partial prevaporisation of the fuel droplets corresponding to an approximate equivalence ratio of the gas phase, ϕ_g, of approximately 0.3. A second set of experiments with a preheating temperature of 50 °C was carried out with ethanol, resulting in ϕ_g of approximately 0.5. This was estimated using a First-Law energy balance approach, shown in Sec. 4.4.

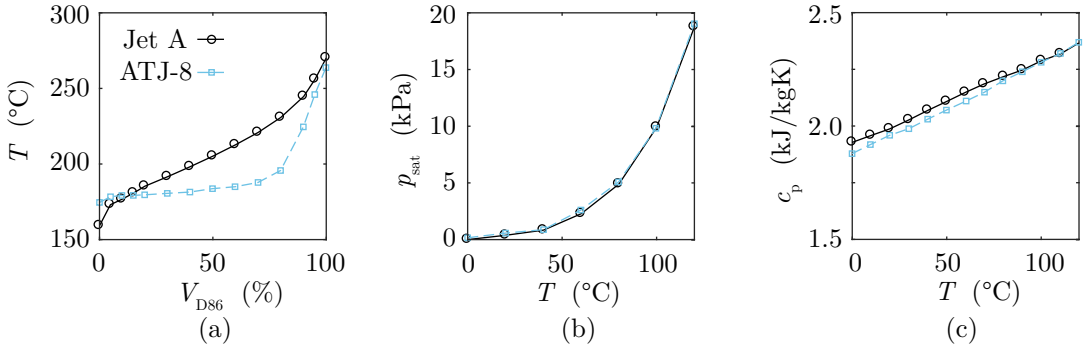

Fig. 3.2 (a) ASTM D86 distillation curve, (b) vapour pressure, and (c) heat capacity of Jet A and ATJ-8. Data obtained from [Edwards, 2017].

3.1.2 Laser ignition

The jet is ignited with a Nd-YAG laser (Continuum Surelite II) beam at 5 mm downstream of the nozzle (Fig. 3.1, detail A). A 532-nm 5-mm diameter laser beam is used, with pulse duration of 4-6 ns. The ignition system consists of a 30-mm plano-convex lens (Fig. 3.1, item 11) to focus the beam, and a 75-mm plano-convex lens and a -30-mm plano-concave lens (12,13) to expand the beam before the focusing lens. This configuration leads to consistent breakdown at the centre of the jet. The laser energy was varied by changing the Q-switch delay of the laser, resulting in incident laser energies from 10–80 mJ. The laser was fired at 2 Hz, and measurements of the incident laser energy E_{in} and the transmitted energy E_{trans} were carried out using pyroelectric energy sensors and a beam splitter (Fig. 3.1, items 14-16) at each shot. Thus, the instantaneous energy absorbed by the flow E_{abs} was evaluated as $E_{\text{abs}} = E_{\text{in}} - E_{\text{trans}}$. It should be noted that this definition does not account for losses along the beam path.

The combination of lenses resulted in a beam with a 3-µm waist at its narrowest point, calculated similarly to Bradley et al. [2004], and Rayleigh length of 53 µm, approximately. The dimensions of the focusing volume are of the same order as the droplet size (5–80 µm), smaller than the average inter-droplet distance of the flow (300–500 µm), and also smaller than the Kolmogorov length scale of flow (∼200 µm). The inter-droplet distance was evaluated based on the droplet number density n calculated from PDA measurements, being $n^{-1/3}$ for a dilute spray [Reveillon and Vervisch, 2005]. In order to evaluate the Kolmogorov length scale, the integral time scale of the flow T_{turb} was obtained from experiments, as further detailed in Chapter 4.3.

3.2 Diagnostics

3.2.1 Flow measurements

A Dantec FiberFlow system was used for the velocity and droplet size measurements. The system was arranged in a 1-D LDA and PDA configuration, allowing for measurements of droplet diameters of up to approximately 80 µm and axial velocity. The system consists of an Argon-Ion laser, a transmitting probe with a 500-mm focal length lens, a receiving probe with a 310-mm focal length lens and three photodetectors, which were positioned at an angle of 30° off-axis from the forward scattering direction. Typical validation rates and spherical validation rates were above 95%, with data rates of the order of 1 kHz. Approximately 20000 samples were obtained per position. The probes were mounted in a 3-dimension traverse, and measurements were taken across the jet for various axial distances, z, from the exit nozzle.

The velocity of the gas phase was estimated by taking the velocity measurements of droplets smaller than 10 µm ($u_{z,\mathrm{g}} = u_{z,d<10}$) corresponding to a Stokes number of the order of 0.01. In this work, the overbar $\bar{y}$ and prime y' symbols denote the time-average and root mean square (rms) of y, respectively, while $\langle y \rangle$ represents a spatial-average of y within the uniform part of the jet, that is, within $r < 0.9R$, approximately, where R is the radius of the jet and r is the radial coordinate.

3.2.2 Visualisation

The flame is visualised with two different setups, shown in Fig. 3.3. Simultaneous high-speed OH*-chemiluminescence and schlieren visualisation is carried out for all range of experimental conditions shown in this work. From this data, the flame speed is evaluated. Additionally, simultaneous OH and fuel planar laser-induced fluorescence provides a more detailed visualisation of the flame front and the spray in the cross-sectional plane formed by the ignition beam and the axis of the jet. OH and fuel PLIF is carried out for the experiments presented in Chapter 6 only. In both visualisation setups, the imaging of the flame is carried out within the first jet diameter downstream of the nozzle. A region of 20×20 mm immediately downstream of the nozzle is imaged, characterised by uniform velocity and droplet size profiles and also free from entrainment of ambient air (Sec. 4.3).

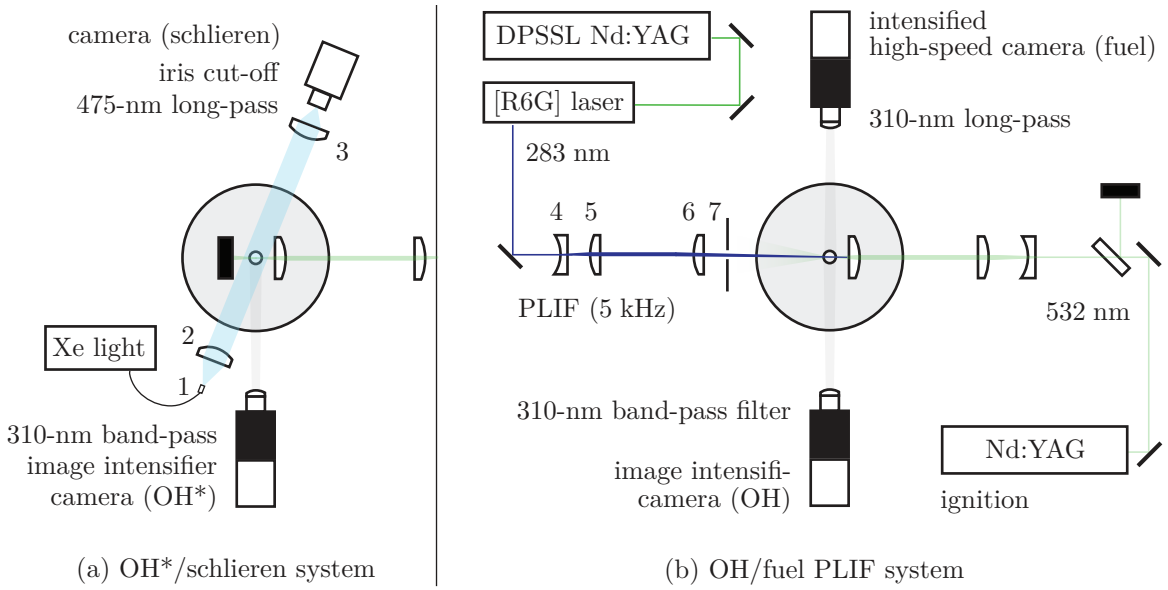

(a) OH*/schlieren system (b) OH/fuel PLIF system

Fig. 3.3 Schematics of the (b) OH*-chemiluminescence and schlieren setup and the (b) OH/fuel planar laser-induced fluorescence setup. The components of the system are: (1) 1-mm optical fiber, (2) 200-mm plano-convex lens, (3) 500-mm plano convex lens, (4) 100-mm plano-convex cylindrical lens, (5) -30-mm plano-concave cylindrical lens, (6) 20-mm plano-convex cylindrical lens, (7) cut-off plate

OH* chemiluminescence and schlieren

High-speed chemiluminescence of the OH* radical and schlieren imaging were used to visualise the flame within the region of interest. For the OH* visualisation, a high-speed CMOS camera (Photron SA1.1) and a two-stage image intensifier (LaVision HS-IRO) were used, equipped with a Scheimpflug extension bellow, a 100-mm UV lens, and a 310 nm band-pass filter. The imaging of the flow was carried out at 12 kHz with an exposure time of 80 µs. The recording of each ignition event was synchronised with the laser beam by using a photodiode, and then delayed by 100 µs[1], lasting for five milliseconds. The resulting size of the image was 20×20 mm, with a nominal resolution of 31.2 µm/pixel. A simultaneous visualisation of the flow was done using the schlieren technique with a second Photron SA1.1 camera operating at the same settings. The light of a Xenon light source (Karl-Storz Xenon Nova 300) exiting a 1-mm optical fibre was collimated with a 200-mm plano-convex lens. The collimated light passed through the flow and was refocused with a 500-mm plano-convex lens, passing through a 1.5-mm pinhole, a long-pass 475-nm filter, and reaching the camera sensor. The imaging parameters (i.e. the frequency, exposure time, etc.) were kept the same as for the OH* system.

[1]Except for Figs. 3.4 and 5.2 for the purpose of capturing breakdown using schlieren.

In the line-of-sight experiments (Fig. 3.3b), the high-speed cameras were operated at 12 kHz and 80-μs exposure time. The camera setup used for OH* chemiluminescence was the same as in the PLIF experiments, except for the use of a wider (25-nm FWHM) 310-nm band-pass filter. All imaging parameters of the system (e.g., gain, aperture, and shutter speed) were kept the same during the experiments so that the OH* signal, representing the approximate heat release in the flame [Hardalupas and Orain, 2004], could be directly compared between conditions. The schlieren system comprised of a CMOS camera (non-intensified), two plano-convex lenses (200-mm and 500-mm), a 1-mm optical fibre and a Xenon light source (Karl-Storz Xenon Nova 300). A 1.5-mm cut-off iris is also used with a long-pass 475-nm filter to improve the sharpness of the image. A resulting nominal resolution of 31.2 μm/pixel is achieved in the line-of-sight visualisation, while 15.6 μm/pixel is achieved in PLIF imaging.

OH and fuel PLIF

In the PLIF experiments (Fig. 3.3a), a high-repetition diode-pumped solid-state laser (JDSU Q201-HD, 532 nm, 14 W at 5 kHz, 18-ns pulse length) is used to pump a high-speed dye laser (SIRAH Credo model 2400) with a solution of rhodamine 6G and ethanol. The resulting 566-nm beam is doubled by a BBO crystal and tuned at approximately 283 nm (at 300 mW, 60 μJ/pulse) to excite the fuel and the $Q_1(6)$ transition in the (1,0) vibrational band of the OH. Sheet-forming optics are used (Fig. 3.3a, 1-3) to produce a sheet of 20 mm in height and approximately 0.1 mm in thickness, that is, of the same order of the largest droplets. The sheet passes through a cut-off plate, which blocks most of the diverging 532-nm ignition beam coming from the opposite direction and aligned with the 283-nm sheet. The fluorescence signal of each ignition event is collected by two high-speed CMOS cameras (Photron SA1.1) coupled with a two-stage image intensifier (LaVision HS-IRO, 500-ns gate), a Scheimpflug extension bellow, and identical 100-mm UV lens. A narrow band filter (10-nm FWHM) centred at 310 nm is used for the OH fluorescence avoiding most of the wide-band fuel fluorescence, which is captured by the second camera using a 310-nm long pass filter. The fluorescence of the kerosene is attributed to the fuel's aromatic content, and occurs mostly between the wavelengths of 320 nm and 360 nm once excited at approximately 283 nm, as experimentally demonstrated by Orain et al. [2014]. Finally, the fluorescence signals of both cameras are post-processed to correct for the sheet's energy profile and pulse-to-pulse fluctuations.

3.3 Procedures

3.3.1 Definitions

As discussed in Chapter 2, the definitions concerning the early phases of ignition are not always clear, often giving rise to ambiguities. In this thesis, the time scale proposed by Cardin et al. [2013] to evaluate the net increase of chain-branching reactions in the flame kernel is used as a metric of the duration of the spark's effects on the flame. This was used to quantitatively differentiate between the phases of kernel generation and flame growth, as represented by the red line in Fig. 5.5. This figure consolidates the relevant time scales and other ignition-related parameters from the literature. In this thesis, the following definitions are used:

Spark event, or ignition attempt: Every laser pulse in which breakdown is attempted.

Flame kernel: Loosely defined as the region of the flow from the moment breakdown occurs and a plasma is formed, up to its transition into a self-sustained flame. Therefore, a kernel is characterised by a length scale shorter than the flow's integral length scale, and a time scale shorter than the bulk flow time scale [Mastorakos, 2017].

Self-sustained flame: The next stage of a flame kernel, characterised by a length scale of the order or larger of the flow's integral length scale, and a time scale of the order or longer than the bulk flow time scale [Mastorakos, 2017].

Kernel formation: In the present experiments, the formation, or initiation, of the kernel depends solely on breakdown of the mixture by the laser, generating a plasma. This is verified in the first frame of the OH* sequence.

Spark effects on the flame: Its duration is defined as the net increase of chain-branching reactions over recombination reactions, evaluated as the time at which a constant OH* emission signal is observed relative to the size of the kernel [Cardin et al., 2013]. For comparison with DNS simulations, it could also be understood as the time at which the maximum temperature of the flame kernel reaches a stable value, being approximately the adiabatic flame temperature [Wandel et al., 2009].

Short mode of ignition failure: Failure to ignite that occurs short relative to the spark [Mastorakos, 2017]. In this work, this represents failure during Phase I, being evaluated based on the complete decay of OH* emissions occurring earlier than the average duration of the spark effects on the flame.

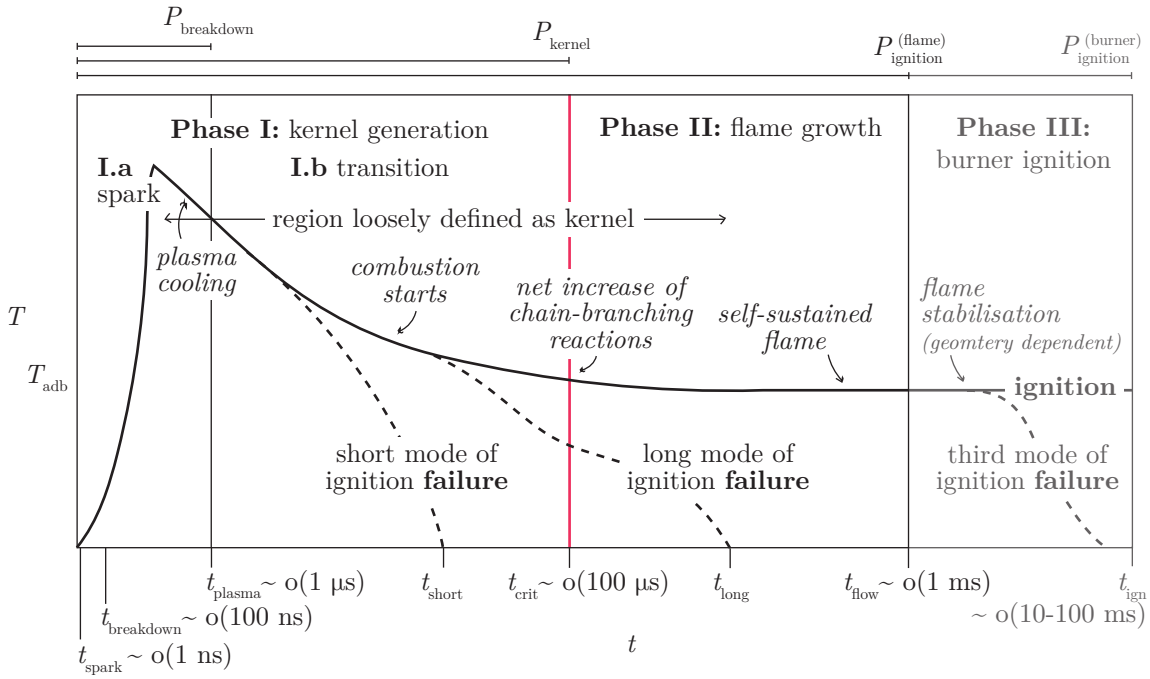

Fig. 3.4 time scales of the process and other relevant definitions. The plot shows the gas temperature in respect to time after the spark. The figure consolidates findings from Wandel et al. [2009], Mastorakos [2009, 2017], Beduneau et al. [2009], Cardin et al. [2013], Phuoc [2006], and Gebel et al. [2015*b*].

Long mode of ignition failure: Similarly, failure to ignite that occurs long relative to the spark [Mastorakos, 2017], representing failure during Phase II.

Kernel establishment: An established kernel is one that survives longer than the average effect of the spark on the flame. In other words, represents the completion of Phase I.

Ignition: In the present experiments, ignition is defined simply as the establishment of a self-sustained flame. That is, completion of Phase II. As no stabilisation mechanism of the flame is present in this experiment, Phase III is not possible.

Probability of breakdown, P_{bd}: Defined as the ratio of events in which breakdown was verified, over the total number of spark events.

Probability of establishing a kernel, P_{ker}: Defined as the ratio of events in which a kernel was verified over the total number of spark events.

Probability of ignition, P_{ign}: Defined as the ratio of events in which ignition of a flame was observed, over the total number of spark events.

Table 3.2 Summary of experimental conditions

Parameters	*Set #1*	*Set #2*	*Set #3*
Fuels	Ethanol	Ethanol	Jet A, ATJ-8
Overall ER	0.8, 0.9, 1, 1.5, 2	1	0.8, 1, 1.4
SMD	20–27 µm	20–27 µm	16, 22, 28, 33 µm ± 1 µm
Bulk velocity	6 m/s ± 0.3 m/s	6, 9, 12 m/s ± 0.3 m/s	7.7 m/s ± 0.4 m/s
Velocity rms	0.2–0.6 m/s	0.2–0.6 m/s	0.3–0.6 m/s
Preheat air	30 °C 50 °C	30 °C 50 °C	100 °C
Gas-phase ER	0.3 0.5	0.3 0.5	0.3
Laser energy	30, 40, 60 mJ	30, 40, 60 mJ	10, 20, 50 mJ
Spark events	120	120	360

3.3.2 Experimental conditions

Experiments were carried out to investigate how mixture, flow, and ignition source parameters affect the ignition process. Three big sets of experiments were performed, and are detailed in Table 3.2. The first set consists of experiments with ethanol, where the effect of varying the overall equivalence ratio was assessed. In the second set of experiments with ethanol, the equivalence ratio was fixed at stoichiometry, and the bulk flow velocity was increased. In the third set of experiments, Jet A and ATJ-8 were studied at fixed equivalence ratios and SMD, at constant bulk flow velocity. In all ethanol experiments, two carrier flow preheating temperatures were investigated (30 and 50 °C), and also four levels of laser energies (30-80 mJ). For the jet fuels, the preheating temperature was set at 100 °C and laser energies varied from 10-50 mJ. In total, 112 experimental test conditions were investigated. For each test condition involving jet fuels, 360 ignition attempts were performed, while only 120 were carried out in ethanol experiments.

An important parameter in spray flames is the equivalence ratio of the gas phase, ϕ_g, which is related to volatility of the liquid fuel and its prevaporisation upstream the region of interest. In this work, this parameter was explored in terms of the preheating temperature of the air flow, which controls the prevaporisation of the fuel inside the burner upstream the region of interest. As the experimental evaluation of ϕ_g is not trivial, a First-Law analysis of the problem was carried out (see Sec. 4.4). For ethanol experiments, it was estimated that ϕ_g was 0.3 and 0.5 corresponding to the preheating temperature of air upstream of the atomiser of 30 and 50 °C, respectively. For jet fuel experiments, that parameter was estimated as 0.3 for 100 °C preheating.

The systematic uncertainty [Coleman and Steele, 2009] of the air mass flow rate was approximately 2% and 1% for the carrier and atomising air, respectively, and 0.2% for the liquid mass flow rate, thus resulting in a derived experimental uncertainty [Moffat, 1988] for ϕ of approximately $\pm 0.3\%$ (confidence interval of 95%). Additionally, a systematic uncertainty of $\pm 2\,^{\circ}\mathrm{C}$ was present, as well as 3% associated with the incident and transmitted laser energy measurements. The variation of the incident and absorbed energies are shown in Section 5.2, and a combined uncertainty of E_{abs} (shown in Fig. 5.3) was evaluated using the Taylor series method for propagation of uncertainties described in Moffat [1988]. These values is given in Table 3.3[2].

Table 3.3 Systematic and derived uncertainties of experimental parameters

Main mass flow rate	2%	Liquid mass flow rate	0.2%
Atomising mass flow rate	1%	Equivalence ratio	0.3%
Temperature	$2\,^{\circ}\mathrm{C}$	Laser energy	3%
Velocity	6%	Droplet size	2%

3.3.3 Flame speed and curvature

Measurement technique

The growth of the flame was evaluated from the OH* image sequences. Each image sequence corresponding to a spark event was binarised based on an absolute threshold. The projected area of the flame A_{f} was evaluated from the binarised images, from which the mean radius of the flame $r_{\mathrm{f}}(t)$ was obtained by assuming an spherical flame, that is, $r_{\mathrm{f}} = \sqrt{A_{\mathrm{f}}/\pi}$. From this parameter, ignition and ignition failure events can be determined simply based on an increase in r_{f} in relation to the first frame. Additionally, the burnt flame speed S_{b} was evaluated as,

$$S_{\mathrm{b}} = \frac{\mathrm{d}r_{\mathrm{f}}}{\mathrm{d}t}. \tag{3.1}$$

Further, the unburnt flame speed was estimated [Egolfopoulos et al., 2014],

$$S_{\mathrm{u}} = S_{\mathrm{b}}\frac{\rho_{\mathrm{b}}}{\rho_{\mathrm{u}}}, \tag{3.2}$$

[2]The systematic uncertainties for velocity and droplet measurements have not been evaluated based on the optical parameters of the PDA/LDA system. Alternatively, a conservative estimate for this system is given, as the standard uncertainties due to variations between each experimental condition were found to be greater (Tab. 3.2).

where ρ_b and ρ_u are the densities of the burnt and unburnt gases, respectively. Here, a series of approximations were made to estimate ρ_b and ρ_u, since the local (effective) equivalence ratio at which the flame burns is unknown as liquid droplets may survive the flame, being found in the burnt products. In the present approach to estimate S_u, the unburnt density was evaluated based on the density of the reactants assuming full vaporisation of the fuel at the overall equivalence ratio and temperature equal to the measured temperature at the outlet of the nozzle. Additionally, the burnt density was evaluated at the adiabatic flame temperature for that mixture.

The unburnt flame speed was evaluated in respect to time for each individual ignition event. A mean value $\overline{S}_u(t)$ corresponding to the unburnt flame speed of a self-sustained flame at a given flow condition was calculated considering ignition events only. Thus, the number of events used to evaluate this quantity varied between flow conditions due to different ignition probabilities. Finally, a time-averaged value of $\overline{S}_u(t)$ was calculated based on the last four images of the sequence, before the flame reached any of the limits of visualisation window. At this point, the effects of the spark on the flame were observed to be negligible, as discussed further in Chapter 5. Still, due to the relatively small size of the flame kernels limited by the jet diameter as well as the visualisation window, some effect of stretch due to the mean curvature of the flame can still be expected.

Additionally, the flame curvature was evaluated from the OH PLIF image sequence. The burnt and unburnt regions were defined based on an absolute threshold corresponding to a progress variable of approximately 0.5. Only the flame front at the most external part of the flame kernel was considered, as from the present visualisation it is not possible to infer if reaction also occurred in the inner part of the flame in cases where a droplet penetrated the propagating front. From that, the flame front was described as a parametric curve $x(s)$ and $y(s)$, and high-frequency variations were filtered using a Fourier-transform low-pass filter. Thus, the local curvature at any point $\mathrm{M}(x, y)$ can be calculated as,

$$\kappa = \frac{x'y'' - y'x''}{(x'^2 + y'^2)^{3/2}}, \tag{3.3}$$

where positive values of κ correspond to a convex flame front in relation to its propagation direction. For reference, the thermal unstretched laminar flame thickness at stoichiometry was calculated from results of the one-dimensional calculations, being approximately 1.8 mm (see Sec. 3.3.3).

One-dimensional flame calculations

The laminar burning velocity of a gaseous flame, $S^{\circ}_{\mathrm{L,g}}$, was obtained from one-dimensional calculations of planar and freely propagating premixed flames. Additionally, these calculations were also used to evaluate ρ_{b} and ρ_{u} so that S_{u} could be estimated. The 1-D calculations were carried out in Cosilab [COSILAB, 2012] using Marinov's [Marinov, 1999], Dagaut's [Dagaut, 2002] and the GRI-Mech [Smith et al., n.d.] chemical mechanisms for ethanol, kerosene, and methane, respectively. The laminar burning velocity was evaluated for a range of equivalence ratios and used for comparison with the present stretched unburnt flame speed measurements in methane-air spherically-expanding flames (used for validation) and in jet fuel-air spray flames. Also, the unstretched laminar flame thickness was calculated from the temperature profile of the flame as $(T_{\mathrm{b}} - T_{\mathrm{u}}) / \max(\mathrm{d}T/\mathrm{d}x)$ [Poinsot and Veynante, 2001].

3.4 Low-order ignition model

In the last part of this work, the low order ignition model SPINTHIR [Neophytou, Richardson and Mastorakos, 2012] is used to predict the ignition capability of an aviation gas-turbine combustor operating with liquid fuels. This model predicts the propagation of a flame in the combustor based on the stochastic motion of "flame particles", simulated from parameters obtained from a time-averaged non-reacting solution of the flow in the combustor.

Inspired by cellular automata methods, the fluid domain is discretised in rectangular cells which can two possible states, i.e. hot or cold, which are determined by the motion of flame particles. At the beginning of the simulation, all cells are set to cold. An ignition event is modelled by switching one or more cells in the domain to the hot state. As the cells switch to the hot state, each emits a virtual flame particle that follows a random walk given by a simplified Langevin model,

$$\Delta \mathbf{X}_{\mathrm{p}} = \mathbf{U}_{\mathrm{p}} \Delta t \tag{3.4}$$

$$\Delta \mathbf{U}_{\mathrm{p}} = -\left(\frac{1}{2} + \frac{3}{4} C_0\right) \left(\frac{L_{\mathrm{turb}}}{u'}\right) (\mathbf{U}_{\mathrm{p}} - \widetilde{\mathbf{u}}) \Delta t + (C_0 \varepsilon \Delta t)^{1/2} \mathbf{N}_{\mathrm{p}} \tag{3.5}$$

The parameters $\Delta\mathbf{X}_\mathrm{p}$ and $\mathbf{U}_\mathrm{p}$ represent the displacement and velocity vectors of the particle. From the cold-flow solution, $\tilde{\mathbf{u}}$ is gas mean velocity, u' is the turbulent velocity fluctuation, L_turb is the integral length scale and ε is the turbulent dissipation rate. The random component to the velocity is added by $\mathbf{N}_\mathrm{p}$, a vector with random direction and length based on a normal distribution $\sim\mathcal{N}(0,1)$. The evolution of the particle gaseous mixture fraction is given by,

$$\Delta\xi_\mathrm{p,g} = \frac{1}{2}C_\xi\left(\frac{L_\mathrm{T}}{u'}\right)\left(\xi_\mathrm{p,g}-\tilde{\xi}_g\right)\Delta t + (1-\xi_\mathrm{p,g})\frac{\overline{\Gamma_m}}{\bar{\rho}}\Delta t \tag{3.6}$$

where $\bar{\rho}$ is the gas density, $\tilde{\xi}_\mathrm{g}$ is the mean gaseous mixture, and $\overline{\Gamma_m}$ is mass source term due to evaporation, which are obtained, for example, from a cold-flow CFD solution.

In order to simulate the growth of the flame, a new particle is emitted when a flame particle enters a cold cell, switching this cell to the hot state. At each time step, an extinction criterion is applied to the particles. This criterion is based on the Karlovitz number of the particle, that is, the ratio of chemical to turbulent time scales, and can be evaluated from the empirical correlation [Abdel-Gayed and Bradley, 1985],

$$\mathrm{Ka_p} = 0.157\left(\frac{u'}{S_\mathrm{L}}\right)^2\mathrm{Re_T^{-0.5}}, \tag{3.7}$$

$$\mathrm{Re_T} = \frac{u'\,L_\mathrm{T}}{\nu}. \tag{3.8}$$

Extinction occurs if $\mathrm{Ka} > \mathrm{Ka_{crit}}$. The value of $\mathrm{Ka_{crit}}$ has been evaluated as 1.5 in premixed flames by Abdel-Gayed and Bradley [1985]. Still, according to Neophytou, Richardson and Mastorakos [2012], although this extinction criterion has been obtained in the context of premixed flames, its use in SPINTHIR for non-premixed and spray systems, in the lack of a better or equally straightforward extinction criterion, also seems to apply, providing accurate results. Further studies on the use of this extinction criterion to sprays system is needed.

Moreover, particles that have extinguished in the domain are no longer computed in the following time steps. Further, ignition success is assessed based on the fraction of domain cells that are marked as burnt and probability of ignition, P_ign, is simply evaluated by performing a large number of simulations for the same condition. In the evaluation of Ka_p, the laminar burning velocity of the spray flame, S_L, is evaluated from the correlation proposed by Neophytou and Mastorakos [2009]. For that, the

Sauter mean diameter of the spray is used, and also the particle's equivalence ratio, ϕ_{p}, and degree of prevaporisation, Ω_{p},

$$\phi_p = \phi_{\mathrm{p,g}} + \phi_{\mathrm{p,l}}, \qquad \Omega_p = \phi_{\mathrm{p,g}}/\phi_p \tag{3.9}$$

The parameter $\phi_{\mathrm{p,g}}$ can be easily calculated from Eq. 3.6, while the evaluation of $\phi_{\mathrm{p,l}}$ is modelled next to account for the liquid fuel fluctuations.

Chapter 4

Flow characterisation

This chapter characterises the droplet-laden jet in which the ignition experiments were carried out. Details of the flow field concerning experiments with ethanol and jet fuels are given in Sec. 4.1 and 4.2, respectively. In Sec. 4.3, the uniformity of the flow field within the visualisation window is verified in terms of velocity and droplet size distributions. Then, an assessment of the degree of prevaporisation of the fuel inside the burner is carried out in Sec. 4.4.

4.1 Ethanol experiments

The turbulence intensity and the Sauter mean diameter of the droplets for the experiments with constant mean velocity (Set #1) are shown in Fig. 4.1. Turbulence intensities generally increased slightly with ϕ (Fig. 4.1a), from 6% to 8%. Inside the burner, turbulence was generated through the high shear between the spray cone and the carrier flow, and higher air flow rates in the air-assist atomiser were needed to atomise high liquid flow rates. As atomisation and turbulence intensity were strongly dependent on each other, the atomisation air flow rate was set in a way to try to minimise the variation of both parameters. Additionally, efforts were made to keep the axial velocity constant in the first set of experiments, within $\pm 5\%$ of 6.1 m/s. Variation of this parameter occurred due to influences of evaporative cooling inside the burner, changes in the atomising air, and different preheating temperatures. Further, by increasing the preheating temperature, a consistent decrease of d_{32} was verified, although some variation was still observed due to changes in atomisation with equivalence ratio. The mean flow parameters in the uniform, central part of the ethanol spray jet are given in Table 4.1.

Table 4.1 Details of ethanol experimental conditions showing mean and rms of axial velocity, $\langle \bar{u}_{z,\mathrm{g}} \rangle$ and $\langle u'_{z,\mathrm{g}} \rangle$, $\langle d_{32} \rangle$, and Rosin-Rammler parameters.

$\langle \bar{u}_{z,\mathrm{g}} \rangle$ (m/s)	$\langle u'_{z,\mathrm{g}} \rangle$ (m/s)	T_{air} (°C)	ϕ (-)	$\langle d_{32} \rangle$ (μm)	$\frac{\langle u'_{z,\mathrm{g}} \rangle}{S^{\circ}_{\mathrm{L,st}}}$ (-)	X (μm)	q (-)	X_m (μm)	q_m (-)
6.2	0.4	30	0.8	25	0.9	34.5	2.31	34.0	7.88
6.1	0.4	30	0.9	25	1.0	35.6	2.25	35.1	7.76
6.1	0.4	30	1.0	25	1.0	37.3	2.13	36.7	7.45
6.0	0.5	30	1.5	27	1.1	39.2	2.22	38.7	7.90
6.0	0.5	30	2.0	28	1.2	41.6	2.26	41.0	8.18
6.0	0.4	50	0.8	20	0.9	26.1	2.63	25.8	8.22
6.1	0.4	50	0.9	20	0.9	26.5	2.49	26.2	7.81
6.1	0.4	50	1.0	20	0.9	27.0	2.49	26.7	7.83
6.2	0.5	50	1.5	22	1.0	31.3	2.31	30.8	7.63
6.4	0.5	50	2.0	24	1.1	36.7	2.21	36.2	7.71
6.1	0.4	30	1.0	25	1.0	37.3	2.13	36.7	7.45
10.5	0.5	30	1.0	27	1.2	44.1	2.29	43.5	8.34
13.1	0.6	30	1.0	27	1.3	44.5	2.34	43.9	8.58
6.1	0.4	50	1.0	20	0.9	27.0	2.49	26.7	7.83
10.3	0.6	50	1.0	24	1.3	39.7	2.11	39.0	7.47
12.9	0.6	50	1.0	26	1.3	43.5	2.10	42.9	7.60

The measurements for experiments with varying bulk flow velocity (Set #2) are given in Fig. 4.2, which shows both $u'_{z,\mathrm{g}}/\bar{u}_{z,\mathrm{g}}$ and d_{32}. Turbulent velocity fluctuations increased slightly with axial velocity (Table 4.1), allowing for experiments where the effect of increasing turbulence and reducing prevaporisation of the flow on ignition was explored. Still, the investigated range of $\langle u'_{z,\mathrm{g}} \rangle / S^{\circ}_{\mathrm{L,st}}$ was limited (0.9-1.3, Table 4.1), corresponding to a regime of weakly corrugated premixed flame. This suggests that the effects of flow parameters on ignition and breakdown probability are more likely to be traceable to overall equivalence ratio, SMD, and small-scale wrinkling associated with the spray, rather than high turbulent strain.

Moreover, a precise characterisation of the polydispsersity of the spray is also given in Table 4.1, allowing for an accurate representation of the ethanol sprays in future simulations of the present experiment. The droplet size distributions followed a modified Rosin-Rammler distribution [Rizk and Lefebvre, 1985],

$$Q(d) = 1 - \exp\left(\frac{\ln(d)}{\ln(X_{\mathrm{m}})}^{q_{\mathrm{m}}}\right) \tag{4.1}$$

where the parameters X_{m} and q_{m} were obtained by fitting of the experimental data.

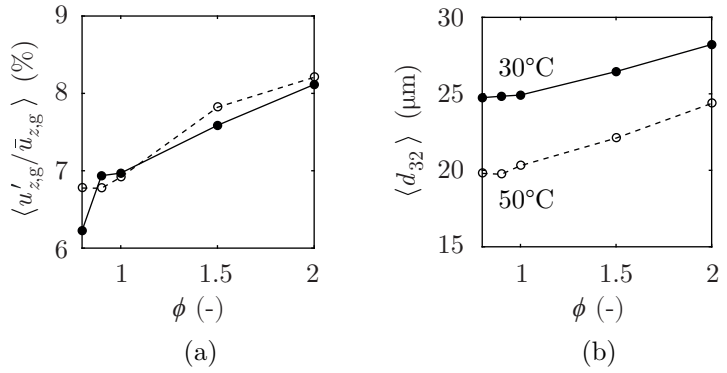

Fig. 4.1 The (a) turbulence levels and (b) Sauter mean diameter for 30 and 50 °C preheat temperature, with varying equivalence ratio – $U_\mathrm{b} = 6\,\mathrm{m/s}$, r=0.

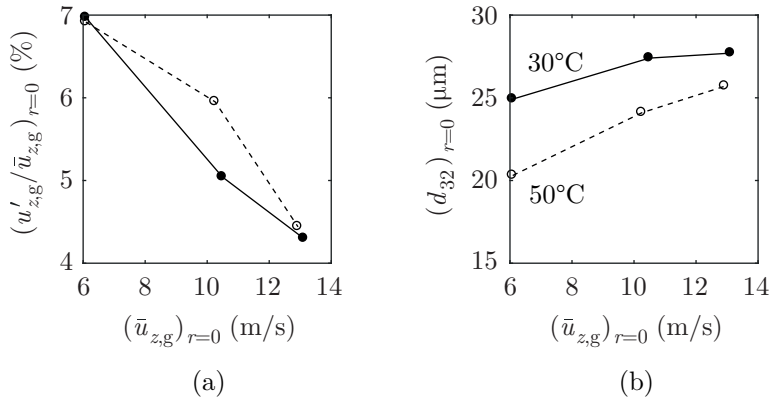

Fig. 4.2 The (a) turbulence levels and (b) Sauter mean diameter evaluated at the centre of the jet ($r = 0$), for 30 and 50 °C preheat temperature, with varying bulk flow velocity – $\phi = 1$.

Further, as briefly mentioned in Sec 3.1, the integral time scale of the flow T_turb was calculated based on PDA/LDA measurements, being approximately 1.5 ms for the present experiments. This parameter was evaluated by integrating the normalised autocorrelation coefficient ρ_turb of the axial velocity signal considering droplets smaller than 10 µm [Pope, 2000],

$$T_\mathrm{turb} = \int_0^\infty \rho_\mathrm{turb}(\tau) d\tau. \tag{4.2}$$

Figure 4.3 shows the (a) autocorrelation coefficient based on the velocity signal shown in (b). The longitudinal integral length scale was evaluated as 9.5 mm, that is, approximately the same as the jet radius. The Taylor hypothesis was assumed for this calculation, hence $L_\mathrm{turb} = U_\mathrm{b} T_\mathrm{turb}$ [Pope, 2000]. Additionally, the Kolmogorov length

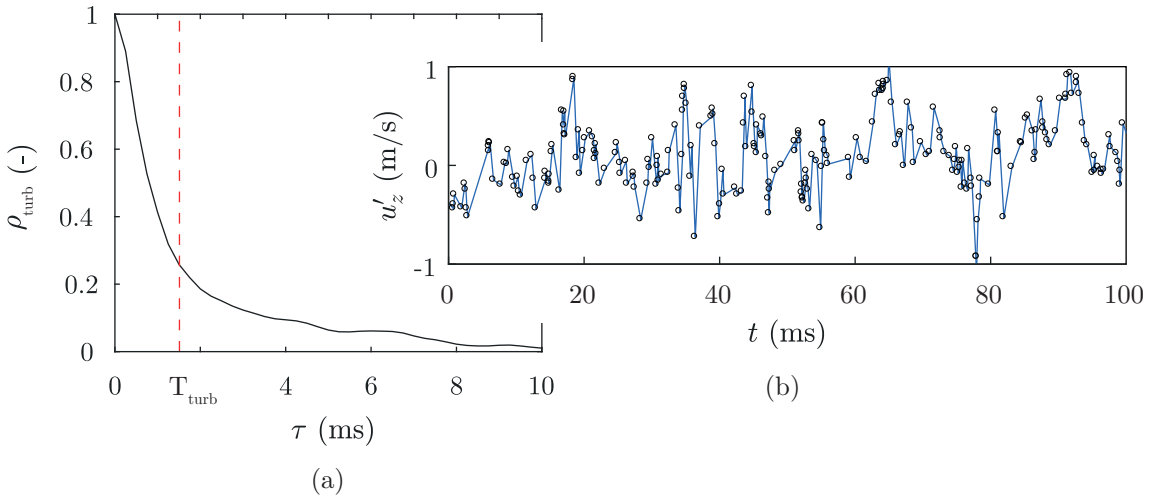

Fig. 4.3 (a) Autocorrelation coefficient for the (b) axial velocity fluctuation signal obtained from the PDA/LDA measurement of droplets smaller than 10 µm – ethanol, $\phi = 1$, U_b=6 m/s, $T_{in} = 30\,^{\circ}$C.

scale was calculated as [Pope, 2000],

$$\eta = L_{\text{turb}} \left(\frac{u'_{z,\text{g}}\, L_{\text{turb}}}{\nu} \right)^{-3/4}, \tag{4.3}$$

being approximately 200 µm in the present experiments.

4.2 Jet fuel experiments

For the Set #3 of experiments concerning the jet fuels, a number of tests were carried out to identify the operating conditions at which a fixed SMD of 16, 22, 28, and 33 µm could be obtained for the spray, for overall equivalence ratios of 0.8, 1, and 1.4. For that, flow velocity and droplet size measurements were performed with the PDA/LDA system while recursively adjusting the carrier and the atomising air flow rates until the desired condition was reached. The distribution of droplet sizes was controlled by varying the air flow rate into the atomiser, allowing for experiments where d_{32} and ϕ were independently set. Rosin-Rammler distributions are shown as an example in Fig. 4.4 for a lean mixture of ATJ-8. Plot (a) represents the accumulated liquid volume and (b) the probability density functions of droplet size. In that figure and throughout Chapter 6 for the experiments with jet fuels, the colours are used to depict the four different degrees of atomisation. Table 4.2 gives the parameters for a modified and

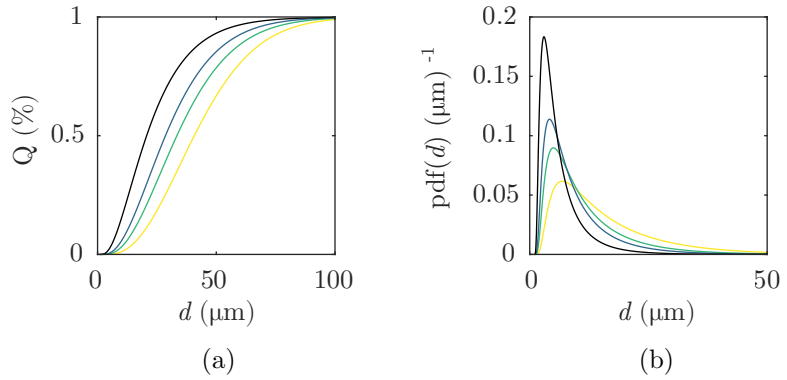

Fig. 4.4 Example of Rosin-Rammler distributions of (a) accumulated volume and (b) pdf of droplet size for four degrees of atomisation – ATJ-8, ϕ=0.8.

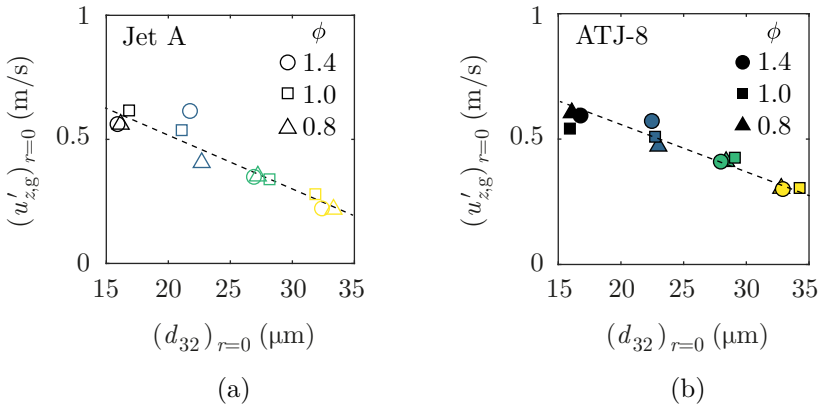

Fig. 4.5 Axial velocity rms fluctuation in terms of the spray SMD for (a) Jet A and (b) ATJ-8.

regular Rosin-Rammler distributions, respectively, for all spray conditions investigated with jet fuels.

The random uncertainty [Coleman and Steele, 2009] associated with the variation of d_{32} between experiments with a fixed ϕ was approximately $\pm 1\,\mu$m for a confidence interval of 95%. In addition to that, some variation of the axial velocity root mean square (rms) fluctuation u'_z occurred within the experiments. A negative correlation between u'_z and d_{32} was observed (Fig. 4.5), as expected from ethanol experiments, since varying the atomising air flow rate to control atomisation affected the generation of turbulence in the jet through the shear between the spray cone and the carrier flow within the burner. Experiments were carried at relatively low turbulence levels corresponding to a regime of weakly corrugated premixed flame ($u'_z/S_{\mathrm{L,g},\phi=1}$ between 0.6-1.4).

Table 4.2 Details of the atomisation conditions for jet fuel experiments (i.e., Set #3).

	Jet A					ATJ-8				
ϕ	d_{32} (µm)	X (µm)	q (-)	X_{m} (µm)	q_{m} (-)	d_{32} (µm)	X (µm)	q (-)	X_{m} (µm)	q_{m} (-)
0.8	33	48.5	2.30	50.1	8.38	33	50.8	2.20	47.8	8.66
0.8	27	40.7	2.05	44.7	7.23	28	45.6	1.95	40.0	7.35
0.8	23	35.3	1.92	38.0	6.12	23	39.0	1.72	34.6	6.62
0.8	16	26.4	1.68	27.9	5.04	16	28.9	1.54	25.7	5.29
1.0	32	48.2	2.06	52.9	8.87	34	53.6	2.30	47.3	7.72
1.0	28	43.4	2.01	46.4	7.59	29	47.2	2.03	42.6	7.35
1.0	21	33.5	1.72	38.5	6.13	23	39.5	1.71	32.7	5.85
1.0	17	26.9	1.68	28.0	5.01	16	28.9	1.53	26.1	5.29
1.4	33	49.4	2.06	52.3	8.64	33	53.2	2.24	48.6	7.75
1.4	27	43.8	1.83	47.0	7.36	28	47.8	1.96	42.9	6.71
1.4	21	32.4	1.93	37.4	6.34	23	31.8	38.3	1.79	6.43
1.4	16	22.3	1.98	28.2	5.20	17	21.9	29.1	1.59	5.75

Further, the Group combustion number G, representing the ratio of the rate of droplet evaporation to the transport of gaseous species by diffusion [Chiu and Liu, 1977], was calculated for the jet fuel experiments based on droplet sizes corresponding to d_{32}. For that, a volume with characteristic length of the order of the longitudinal integral length scale of the flow, L_{turb}, was assumed. Within the present conditions, G increased with ϕ and d_{32}, ranging from approximately 10 to less than 100 for ϕ of 0.8 and 1, and to over 100 for ϕ of 1.4. The range of $1 < G < 100$ represents the external combustion mode [Chiu and Liu, 1977], and is characterised by an increasing droplet burning rate from the centre of the cloud towards its outer layer as as G increases. For higher values of G, above 100, the combustion mode was defined as sheath combustion, which indicates that droplet vaporisation within the cloud is negligible and occurs mostly in a thin external layer of the cloud [Chiu and Liu, 1977]. In Chapter 6, G and ϕ are used to classify the experimental conditions in terms of the propagation modes observed.

4.3 Flow uniformity

A uniform flow field within the visualisation window is necessary to allow for the spherical expansion of the flame in the ignition and flame speed experiments. A verification of the uniformity of the flow at the exit of the nozzle was carried out for a range of air flow rates resulting in bulk velocities from 6 to 15 m/s. In order to

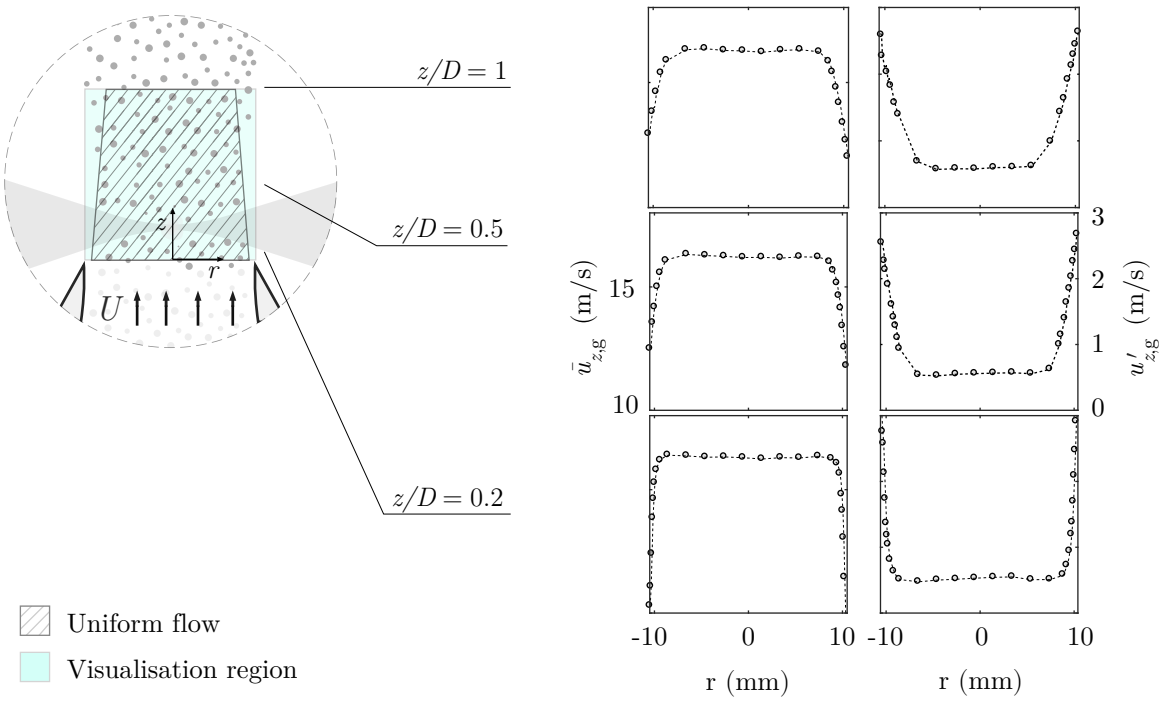

Fig. 4.6 Radial profiles of axial velocity (left column) and fluctuation (right column) along the axial coordinate of the jet within the region of interest (z/d=1, 0.5, and 0.2, from top to bottom).

allow for PDA measurements, a small flow rate of ethanol was injected in the air flow ($\phi = 0.1$, T_a =26 °C). The flow within the visualisation window is shown in Figure 4.6 for U_b =15 m/s, although other velocities also presented an equally uniform profile. The profiles of mean axial velocity $\bar{u_z}$ and rms u'_z were measured for three axial distances downstream the exit of the nozzle, corresponding to z/d of 0.2, 0.5, and 1. A top-hat velocity profile was observed at the exit of the nozzle, and the increasing thickness of the mixing layer along the axis of the jet can also be observed (corresponding to the low velocities or high turbulence in the plots). The mixing layer of the jet was identified, and all measurements were then carried out within the core region (cross-hatch region within the visualization window, Fig. 4.6). The profiles of $\bar{u_z}$ and u'_z for a range of bulk velocities are shown in 4.7, and confirm the uniformity of the flow field for the range of bulk velocities investigated in this work.

Figure 4.8a shows the bulk velocity evaluated from the mass flow rate measurements U_b (horizontal axis), versus the bulk velocity evaluated by integrating the velocity profile of the gas phase along the diameter of the nozzle U_b^{LDA} (vertical axis). The combined uncertainty of U_b is shown in the horizontal error bars, and accounts for the uncertainty due to evaporative cooling, due to measurements of the diameter of the

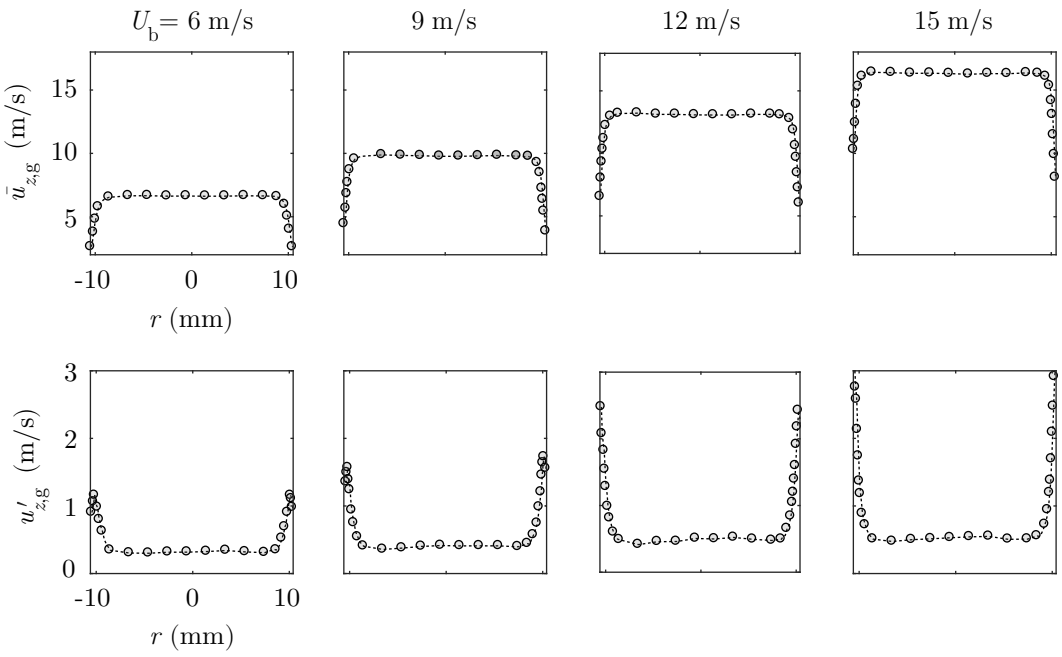

Fig. 4.7 Radial profiles of axial velocity and fluctuation along the axial coordinate of the jet at the exit of the nozzle (z/d=0.2).

nozzle, temperature, and mass flow rate. The uncertainty due to evaporative cooling was evaluated from the minimum and maximum velocities of the gas phase assuming the case of full prevaporization and zero prevaporization of the fuel, respectively.

Further, the uniformity of droplet sizes along the radial coordinate of the jet for the range of equivalence ratios investigated in the ethanol experiments is evaluated in Fig. 4.9. Nine overlapping curves are shown in each plot, representing pdfs of droplet size taken every 2 mm along the radial coordinate of the jet; starting at 2 mm from the mixing layer of the jet. The spatial-averaged Sauter mean diameter $\langle d_{32} \rangle$ is shown, with the grey area indicating the variation of this parameter across the jet. Some variation of d_{32} in terms of r was mainly seen in experiments with high equivalence ratios, being related to a small variation of the number distribution at large droplet sizes, therefore resulting in a significant change of d_{32} for the whole distribution. Additionally, typical number and volume distribution based on the droplet sizes are shown in Fig. 4.10. As all experimental conditions followed the modified form of the Rosin-Rammler distribution, as seen in Fig. 4.11, the droplet size distributions were expressed in terms of Rosin-Rammler and Modified Rosin-Rammler distributions. This allows for a precise implementation of the spray size in future simulations of this experiment.

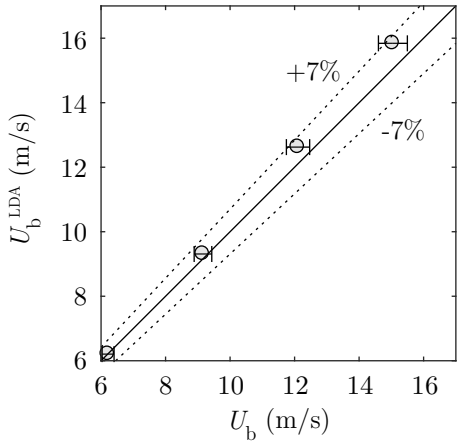

Fig. 4.8 Bulk velocity obtained from PDA and from flow rates and temperature measurements.

The end velocity of the droplets at the exit of the nozzle is illustrated in Fig. 4.12a. Mean axial velocity and turbulence are shown, and were calculated according to five classes, d (μm), of droplet size: $d < 5$; $5 < d < 10$; $10 < d < 30$; $30 < d < 50$; $d > 50$. Overall, for the range of conditions investigated in the ethanol experiments, about 95% of the total number of droplets were within the first 3 categories, that is, were smaller than 30 μm. Figure 4.12a shows that the mean axial velocity of these small droplets were virtually the same across the profile, therefore, no drift between the gas and the liquid phase existed. The Stokes number of the droplets was evaluated based on the longitudinal integral length scale of the flow and the axial velocity root mean square (rms) fluctuation.

$$\mathrm{St}_k = \frac{t_{0,k}\, u'_z}{L_{\mathrm{turb}}} \tag{4.4}$$

where the relaxation time of the particle of size k is,

$$t_{0,k} = \frac{t_0\, {d_k}^2}{18\mu_{\mathrm{g}}}. \tag{4.5}$$

Droplets between 10-30 μm had a Stokes number between 0.01-0.1, thus closely following the flow. However, droplets larger than 30 μm were found to be slower, with axial velocity of -0.3 and -0.9 m/s relative to the gas phase, for classes $30 < d < 50$ and $d > 50$, respectively. The largest droplets represented approximately 10% of the fuel, and their relative velocity may have affected the growth of the flame, especially in the jet fuel experiments with high SMD. Relative to the flow, large droplets moved towards the upper flame front and away from the lower front as the flame expanded.

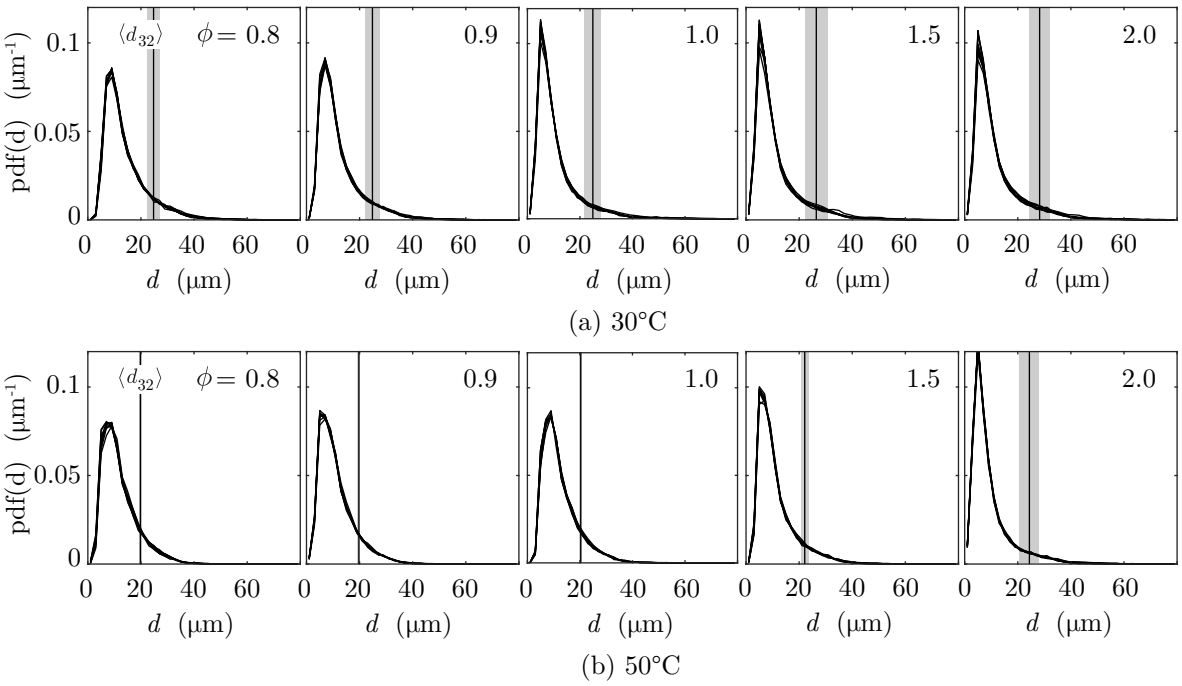

Fig. 4.9 Pdfs of droplet size: ethanol, (a) $T_{\mathrm{in}} = 30\,^{\circ}\mathrm{C}$ and (b) $50\,^{\circ}\mathrm{C}$, $U_{\mathrm{b}} = 6\,\mathrm{m/s}$.

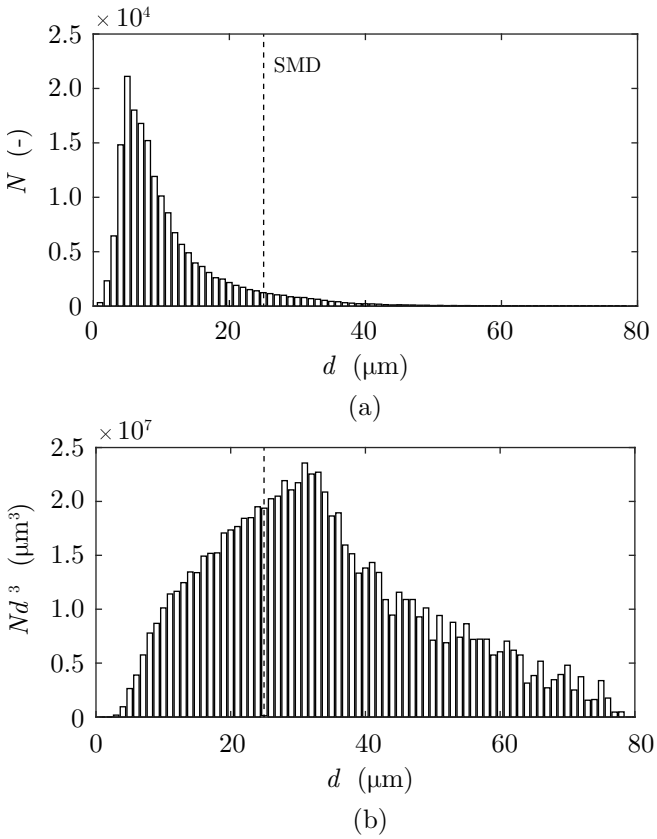

Fig. 4.10 Typical histograms of (a) droplet size and (b) liquid volume distribution ($\sim Nd^3$) concerning measurements within the uniform part of the jet – ethanol, $T_{\mathrm{in}} = 30\,^{\circ}\mathrm{C}$, $U_{\mathrm{b}} = 6\,\mathrm{m/s}$, $\phi = 1$.

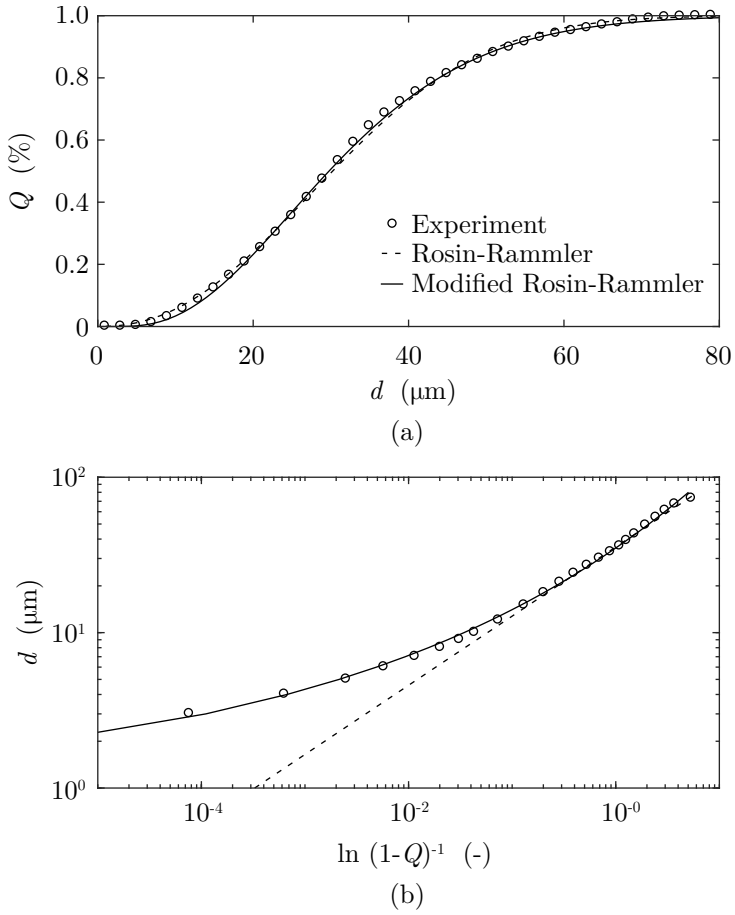

Fig. 4.11 (a) Accumulated volume in terms of droplet size and (b) typical Rosin-Rammler plot – ethanol, $T_{\mathrm{in}} = 30\,^{\circ}\mathrm{C}$, $U_{\mathrm{b}} = 6\,\mathrm{m/s}$, and $\phi = 0.9$.

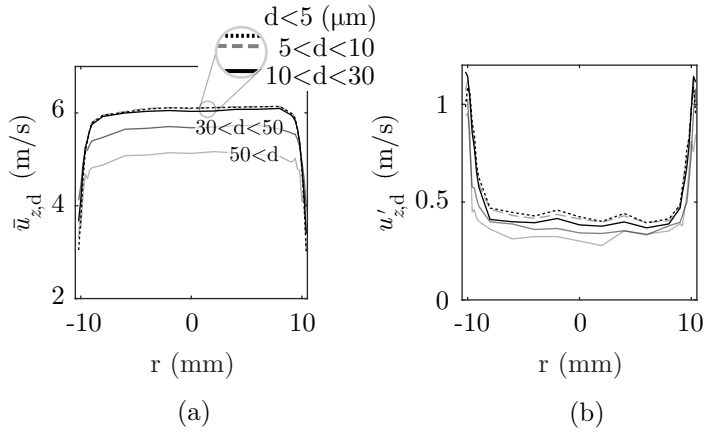

Fig. 4.12 Radial profiles of (a) axial velocity and (b) turbulent fluctuation according to range of droplet sizes – $z/d = 0.2$, $U_{\mathrm{b}} = 6\,\mathrm{m/s}$, and $\phi = 1$.

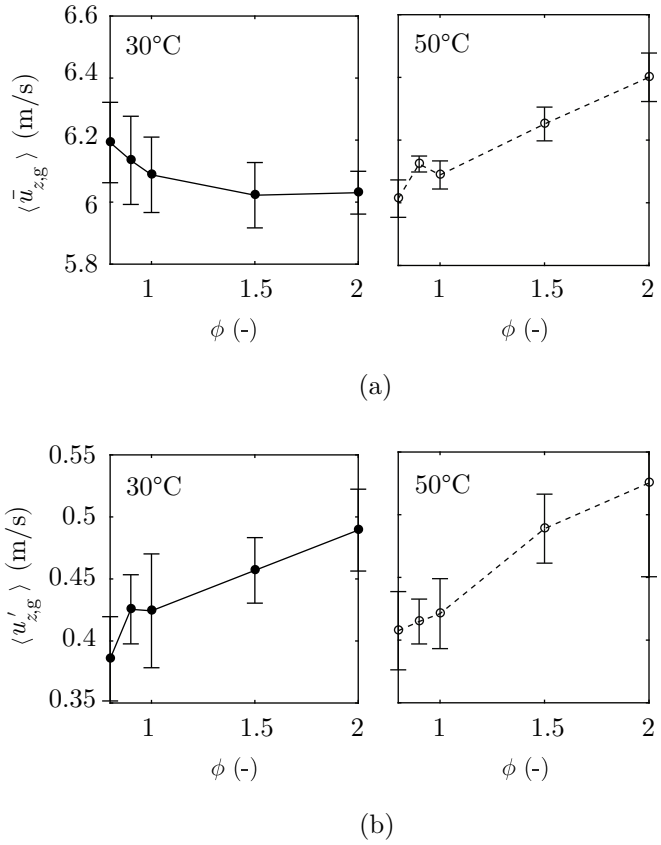

Fig. 4.13 The (a) velocities and (b) turbulent fluctuations in the axial direction concerning the uniform part of the top-hat velocity profile for 30 and 50 °C – ethanol, $U_\mathrm{b} = 6\,\mathrm{m/s}$. Error bars represent the variations along the radial coordinate.

The profile of the rms turbulent velocity for each droplet class is shown in Figure 4.12b, showing that droplets up to 10 µm were found to be responsive to velocity fluctuations. Thus, these were used to estimate the gas-phase velocity.

Additionally, the mean axial velocity and turbulence were also assessed across the profile for the range of conditions investigated (Fig. 4.13). The variation of the mean velocity and rms velocity fluctuation along the radial coordinate is shown as an error-bar for each marker. Experiments were carried out in a way such the centreline velocity was kept constant. Nevertheless, $\langle \bar{u_z} \rangle$ varied within $\pm 3\,\%$ due to changes in the carrier and atomising flow rates as ϕ changed, and also due to evaporation of the liquid fuel which also affects the flow rate and temperature of the gas phase.

4.4 Degree of prevaporisation

In the ethanol experiments, the amount of fuel prevaporised upstream the region of interest, $\dot{m}_{\mathrm{f,g}}$, was estimated from an energy balance of the flow in the burner,

$$[\dot{m}_{\mathrm{l}} h_{\mathrm{l}}(T_{\mathrm{l}}) + \dot{m}_g h_{\mathrm{g}}(T_{\mathrm{g}})]_{\mathrm{in}} = [\dot{m}_l h_{\mathrm{l}}(T_{\mathrm{l}}) + \dot{m}_{\mathrm{g}} h_{\mathrm{g}}(T_{\mathrm{g}}) + \dot{m}_{\mathrm{f,g}} h_{\mathrm{lv,f}}]_{\mathrm{out}}\,, \tag{4.6}$$

where the subindices l and g are the liquid and gas phase, respectively, h_{k} is the enthalpy of the given phase k at temperature T_{k}, and $h_{\mathrm{lv,f}}$ is the enthalpy of vaporisation of the fuel. At the inlet, $\dot{m}_{\mathrm{g}}$ is simply the total measured mass flow rate of air, T_{l} is taken as the ambient temperature, and T_{g} is the preheating temperature of the air measured upstream of the atomiser. At the outlet, the gas phase mass flow rate is,

$$\dot{m}_{\mathrm{g}}|_{\mathrm{out}} = \dot{m}_{\mathrm{g}}|_{\mathrm{in}} + \dot{m}_{\mathrm{f,g}}|_{\mathrm{out}}. \tag{4.7}$$

Given that the residence time of the droplets inside the burner was verified to be relatively long in Large Eddy Simulations of the present experiment (M.P. Sitte, personal communication), saturation of fuel in the gas phase was assumed at the outlet of the nozzle, as well as thermal equilibrium of the gas and liquid phases ($T_{\mathrm{g}} = T_l$). The total amount of fuel vaporised is given by,

$$\dot{m}_{\mathrm{f,g}}|_{\mathrm{out}} = y^{\mathrm{sat}}_{\mathrm{f,g}} \dot{m}_{\mathrm{g}}|_{\mathrm{out}}, \tag{4.8}$$

where the mass fraction of fuel for saturation is,

$$y^{\mathrm{sat}}_{\mathrm{f,g}} = \frac{x^{\mathrm{sat}}_{\mathrm{f,g}} MW_f}{(x^{\mathrm{sat}}_{\mathrm{f,g}} MW_f + (1 - x^{\mathrm{sat}}_{\mathrm{f,g}}) MW_{\mathrm{air}})}, \tag{4.9}$$

and $x^{\mathrm{sat}}_{\mathrm{f,g}}$ depends on the saturation pressure of the fuel at the gas-phase temperature, and is evaluated from its partial pressure,

$$x_{\mathrm{f,g}} = \frac{P_{\mathrm{sat,f}}(T_{\mathrm{g}})}{P_{\mathrm{atm}}}. \tag{4.10}$$

The enthalpy of the gas mixture in Eq. (4.6) was evaluated by taking the specific heat capacity of the mixture assuming an ideal mixture. Equations (4.6-4.10) were solved numerically using thermodynamic tables for h and c_{p} of air and ethanol. Figure 4.14 shows the calculated equivalence ratio of the gas phase, ϕ_{g}. A mean value of 0.3 and

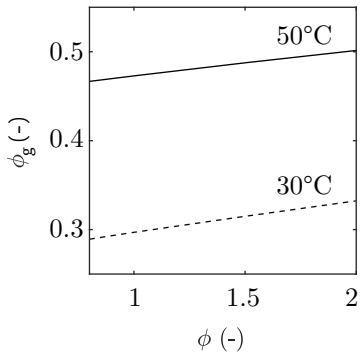

Fig. 4.14 Calculated equivalence ratio of the gas phase in terms of the overall equivalence ratio for ethanol experiments.

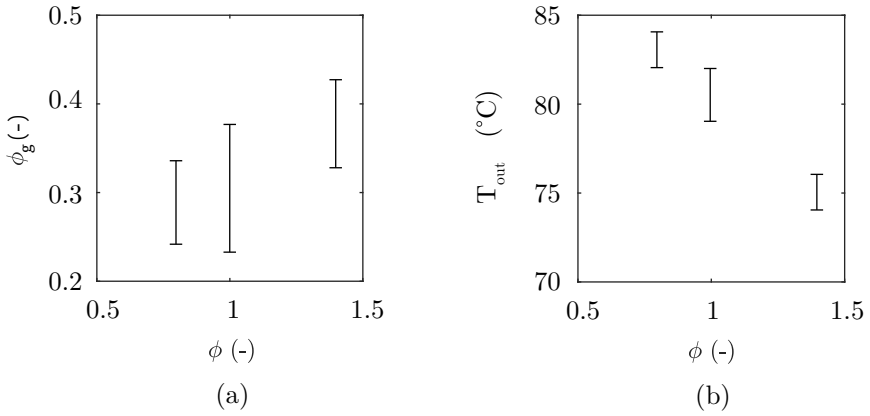

Fig. 4.15 Calculated (a) equivalence ratio of the gas phase and (b) measured temperature at the outlet of the burner in terms of the overall equivalence ratio for ATJ-8 and Jet A experiments.

0.5 was obtained for preheating temperatures of the air flow upstream the atomiser of 30 °C and 50 °C, respectively.

Similarly, in the jet fuel experiments, a degree of prevaporisation of roughly 0.3 was estimated using the First-Law energy balance approach given previously. Still, for the jet fuel experiments, only thermal equilibrium was assumed at the outlet (and not saturation of the gas-phase). Thus, the measured temperature of the flow at the outlet of the burner, T_{out} was used to evaluate Eq. 4.6. Figure 4.15 shows (a) the calculated gas-phase equivalence ratio and the (b) measured outlet temperature for each equivalence ratio of the experiments. Each bar in the plot represents the maximum and minimum values at each condition, considering experiments with all atomisation conditions and both ATJ-8 and Jet A fuels.

Chapter 5

Stochastic nature of ignition

5.1 Motivation and objectives

The factors preventing a flame kernel from igniting in a combustor filled with an overall flammable mixture are associated with fluctuations at the spark location, giving rise to fuel starvation by the flame and heat transfer to the surrounding flow [Mastorakos, 2009]. Such fluctuations include turbulence [Chakraborty et al., 2007], fuel concentration fluctuations [Birch et al., 1981], and those arising from the randomness of the breakdown of the mixture caused by the spark [Phuoc, 2006]. Additionally, fuel inhomogeneities are intrinsic to spray flows, and further fluctuations may occur due to droplet breakup, atomisation and evaporation processes [Mastorakos, 2017]. Hence, the identification of the conditions conducive to the initiation and growth of a flame in a spray can be challenging as such fluctuations add up and interact, giving the ignition process its stochastic character.

In spray flows, the presence of droplets at the spark location can facilitate the breakdown of the mixture by a laser spark [El-Rabii et al., 2005], increasing the probability of breakdown. Still, their presence in the kernel or its vicinity has been shown to be overall detrimental to ignition in cases of large or slowly-evaporating droplets, and beneficial to ignition in experiments with small droplets [Singh and Polymeropoulos, 1988; Danis et al., 1988]. By looking at the local and instantaneous conditions at the spark location, DNS has provided a great deal of insight about the effects of droplets on the establishment of a flame kernel. Following the deposition of

The results of this chapter concerning experiments with ethanol have been published in: de Oliveira, P.M., Allison, P.M., Mastorakos, E. [2019], 'Ignition of uniform droplet-laden weakly turbulent flows following a laser spark', *Combustion and Flame* **199**, 387–400.

energy by the spark, quenching of the flame is characterised by two distinct modes: short mode and long mode of ignition failure [Mastorakos, 2017]. Short-mode failure has been observed in simulations where low temperature of the kernel was observed following the spark [Wandel et al., 2009], which can occur either due to excessive removal of heat from the kernel through stretch by intense turbulence [Chakraborty et al., 2007], or even due to a small-sized kernel formed after energy deposition in a locally lean mixture [Wandel, 2014]. In contrast, slowly-evaporating droplets leading to excessive heat loss and fuel starvation were characteristic of long-mode failure [Wandel, 2014].

Typical ignition failure time scales verified in DNS were approximately $0.6t_\mathrm{f}$ for short-mode failure [Chakraborty et al., 2007; Wandel et al., 2009] and $1.4t_\mathrm{f}$ for long-mode failure [Wandel et al., 2009]; these are defined in terms of the chemical time scale of the flame, t_f. These time scales were assessed as the time interval for the temperature of the kernel to drop from its maximum value (at the moment of spark deactivation) down to the temperature of the fresh mixture. Moreover, recent experiments in gaseous mixtures suggested that the plasma composition may have an important impact on the formation of the kernel [Beduneau et al., 2009; Cardin et al., 2013; Gebel et al., 2015*b*]. The kick-start of chain-branching reactions and their net increase over recombination reactions was identified by measuring OH* emissions in the cooling of the kernel [Beduneau et al., 2009; Cardin et al., 2013] and, ultimately, provides a measure of the duration of the spark effects in the process. These findings may be applied towards defining the transition between the phases of kernel generation and flame growth.

In experiments with sprays, the effect of droplets on the duration of the decay of the plasma and initiation of combustion reactions has not yet been measured. In fact, experiments focusing on probability of ignition have only looked at the burner-scale aspects of the problem [Moesl et al., 2009; Marchione et al., 2009; Letty et al., 2012], and although some experiments have evaluated MIE in terms of the global parameters of the flow [Ballal and Lefebvre, 1978*a*, 1979; Dietrich et al., 1991], ignition probabilities and ignition failure time scales have not been investigated in terms of global flow parameters in uniform flow and spray configurations. In this chapter, a characterisation of the early phase of the ignition process is carried out, identifying the conditions which are most conducive to ignition as well as the effects of spray and spark fluctuations on the process. For that,

- Ignition experiments are carried out in a uniformly distributed droplet dispersion in turbulent air, allowing for ignition of a flame by means of a laser spark. The main parameters of the two-phase flow are dicussed in Chapter 3, ensuring an accurate representation of the droplet-laden flow for future simulations.

- The flame is visualised using simultaneous high-speed schlieren and OH* chemiluminescence. Based on the OH* image sequences, the size of the flame kernel is evaluated, thus allowing for the distinction between a successful and a failed ignition event.

- An evaluation of the energy deposited in the flow by the laser spark in each event is carried out in terms of the spray parameters in order to identify the effects of droplets on the process. Additionally, the time scale of the spark effects on the flame is assessed based on the OH* image sequences.

- Based on the duration of the spark effects, the time scales of short and long mode of ignition failure can be evaluated. The effects of fuel, equivalence ratio, prevaporisation degree, ignition energy, and initial kernel size on those time scales are then investigated.

- Finally, the probabilities of ignition and minimum ignition energy using a laser spark are assessed.

5.2 Kernel formation and ignition

The first instants following the spark are shown in the schlieren imaging of Fig. 5.1. The laser beam, focused at the centre of the flow, caused breakdown of an ethanol spray (b) and generated a flame kernel that grew (c) and advected downstream of the jet (d). Due to the camera's long exposure (80 µs), frame (b) shows simultaneously the scattering of the beam due to the droplets, the bremsstrahlung radiation emitted by the plasma at the focusing point, and the initial kernel. Increasing the incident energy of the laser lengthened the plasma from 0.5 to 1.5 mm as seen in Fig. 5.2 for a spark in quiescent air, which then led to larger initial kernels. Such kernels were large compared to the interdroplet distance, thus it is expected that fuel vapour fluctuations in the interdroplet space did not affect the generation of the kernel.

Part of the randomness of the laser ignition process of spray flows is illustrated in Fig. 5.3, which shows in ethanol sprays (a) the shot-to-shot variation of the incident

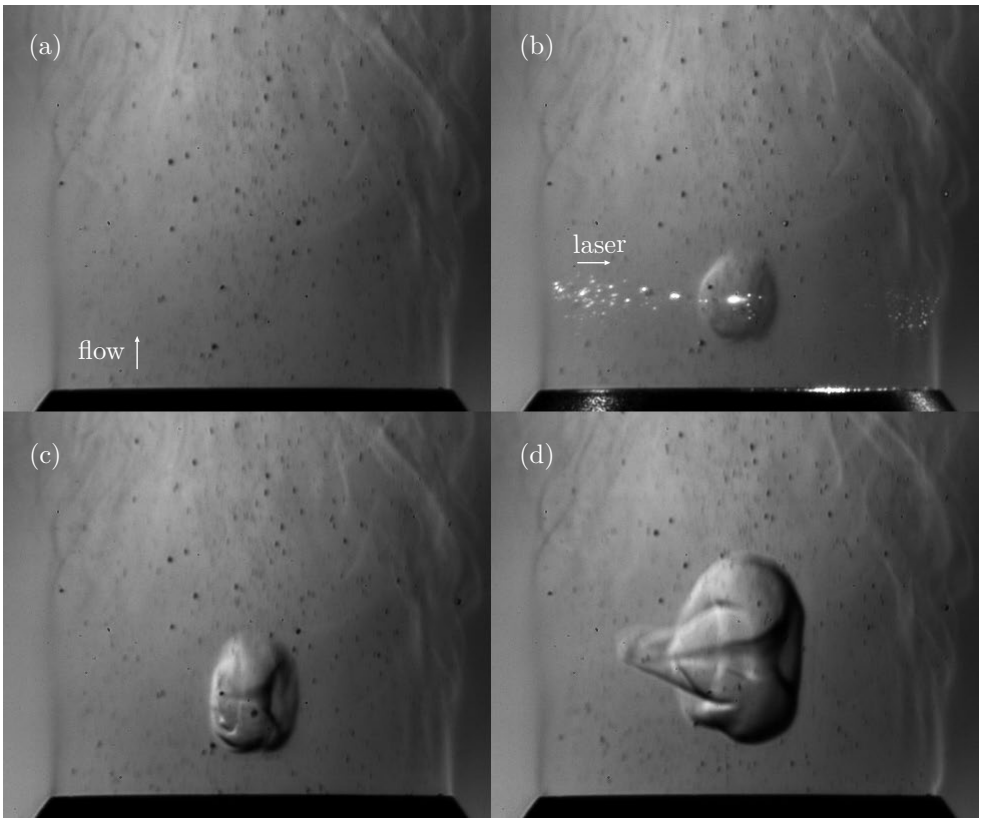

Fig. 5.1 Schlieren image sequence illustrating the ignition process: (a) droplet-laden flow, (b) laser spark, (c) flame kernel, and (d) growth and convection of the flame downstream the jet – ethanol, $U_\mathrm{b} = 6\,\mathrm{m/s}$, $\phi = 1.5$, $T_\mathrm{in} = 30\,^\circ\mathrm{C}$, $E_\mathrm{in} = 60\,\mathrm{mJ}$).

laser energy E_in and the absorbed energy by the flow E_abs. The result of the spark event is depicted by different markers representing three possible outcomes: ignition, kernel formation and subsequent quenching, and no kernel formation (i.e. no breakdown). No evident relation between the fluctuations of E_in and E_abs was observed (i.e. not constant $E_\mathrm{abs}/E_\mathrm{in}$, nor between E_abs and the outcome of the spark event. Conditional averages of E_abs based on the spark outcome are depicted as horizontal lines. The average value of E_abs concerning no-breakdown cases offers a reasonable estimation of the energy lost due to absorption and Mie scattering along the beam path. Hence, for this condition, it can be estimated that only approximately half of E_abs contributed to breakdown of the mixture. No significant difference between the average E_abs corresponding to successful and failed ignition events was observed in this condition.

Further, the resulting kernels of a successful breakdown event presented variation in OH* density and size, which strongly affected the outcome of an ignition event, as discussed further in Sec. 5.3. These variations are shown in Fig. 5.3b, with flame kernels

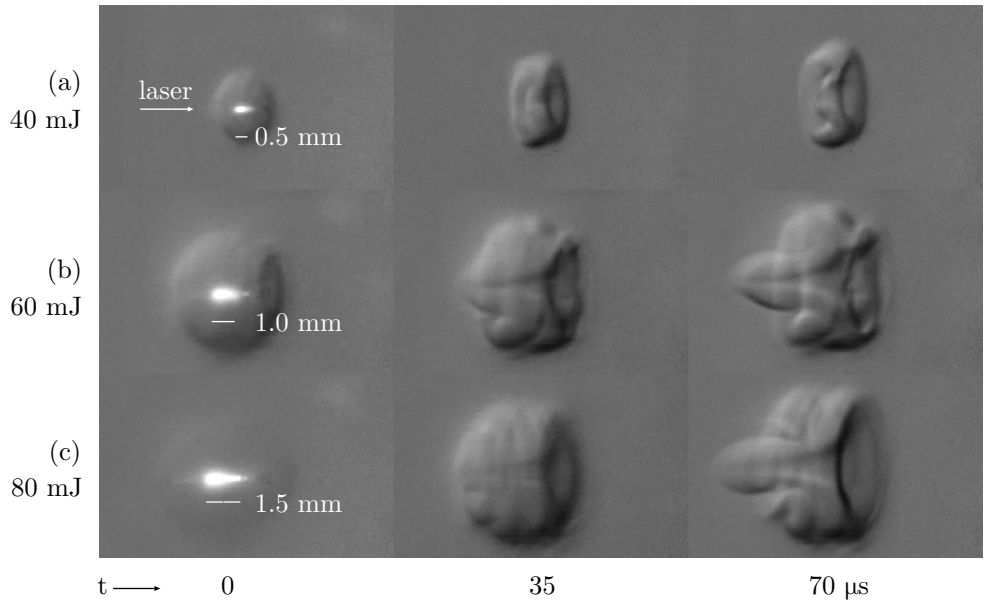

Fig. 5.2 Schlieren visualisation of the breakdown and following 70 µs after a spark event in quiescent air for laser energy of (a) 40 mJ, (b) 60 mJ, (c) 80 mJ.

imaged 100 µs after the spark, for specific ignition attempts chosen from Fig. 5.3a. These events were grouped by similarity in the E_{abs} plot: events 17 and 33 presented a peak value of E_{abs} and resulted in successful ignition, while 16 and 60 resulted in the quenching of the flame even though E_{abs} was also high in both events. Although these events presented kernels of similar size, events 17 and 33 were characterised by a much stronger OH* signal, indicating higher reaction rates in the flame kernel. In contrast, events 22 and 80 show small kernels with a low OH* intensity that still resulted in ignition, although the respective E_{abs} values were low and similar to events where breakdown was not observed. Finally, 48 shows a small kernel that quenched but was identified through the first frame of the OH* sequence and through schlieren.

Following the formation of a kernel, its development into a self-sustained flame is illustrated in Figure 5.4. The average radius of the flame r_{f} as a function of time after the spark event t is shown in Fig. 5.4a, with each curve representing one distinct ignition attempt. Events where the kernel developed into a self-sustained flame are marked in red, representing ignition, while events where quenching occurred are marked in blue. This notation is used throughout this work. In this figure, the effect of increasing the incident energy on the total number of kernels can be clearly observed, while a significant increase of the number of kernels that ignite only occurred for 80 mJ. Additionally, other effects of laser energy on the flame growth can be observed: successful ignition

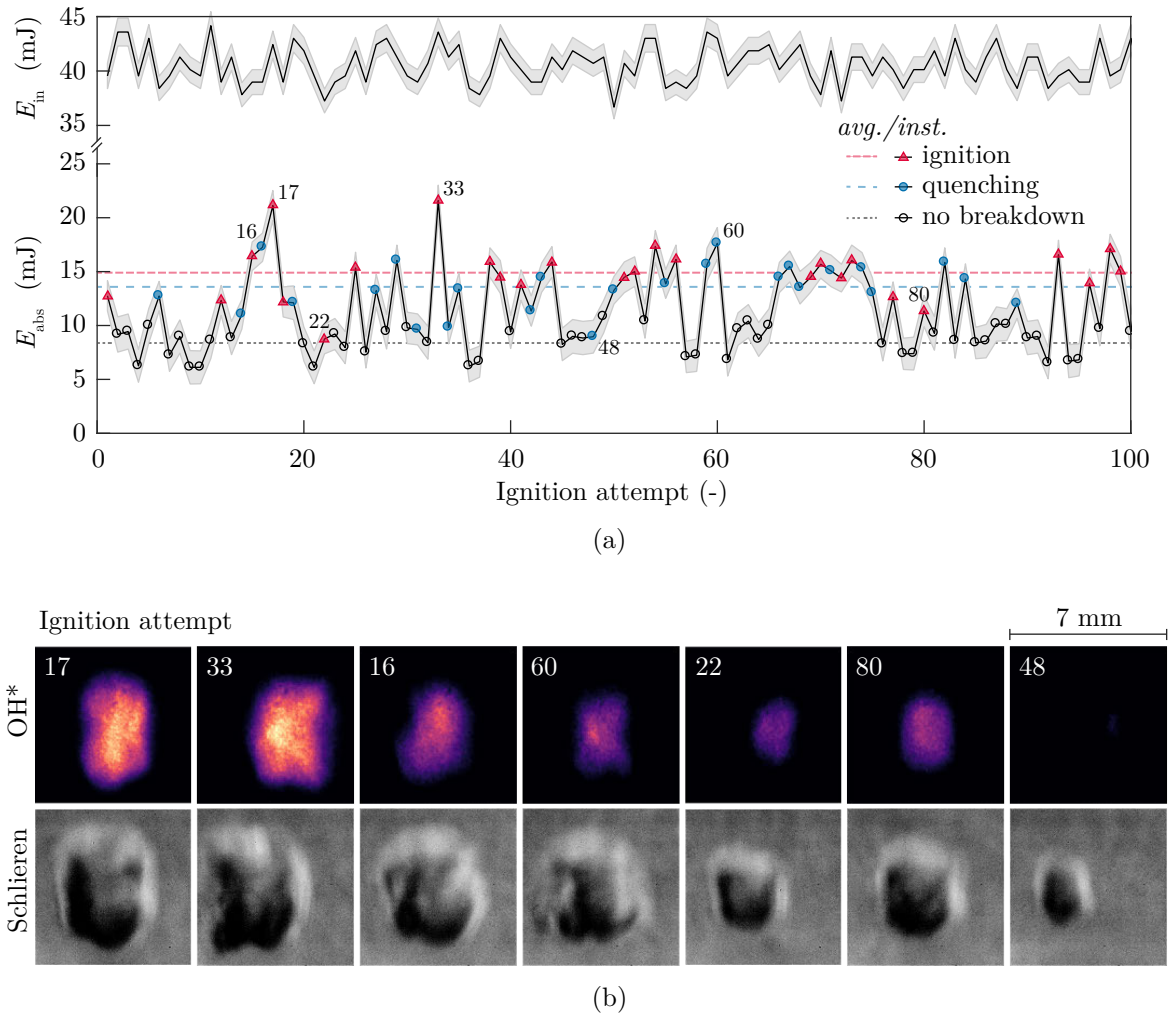

Fig. 5.3 Ignition attempts – ethanol, $U_b = 12\,\mathrm{m/s}$, $\phi = 1$, $T_{in} = 30\,^{\circ}\mathrm{C}$. (a) The incident laser energy and absorbed energy, and their respective systematic and expanded uncertainty values (shown in light grey). Conditional averages based on ignition, quenching, and no breakdown are shown in horizontal lines. (b) OH* and schlieren visualisation at t=0.1 ms for selected ignition attempts based on the value of E_{abs} and the outcome of the event as defined in (a).

events with higher energy, for example, presented a steeper slope of r_f until $t = 0.2\,\mathrm{ms}$, indicating the persistence of the flame overdrive effect due to the laser spark [Bradley et al., 2004]. This effect seemed to strongly affect the initial size of the kernels, due to a combination of increasing the plasma size and, consequently, the absorbed energy as the incident energy increases, with the flame overdrive that accelerates the growth of the kernel immediately after the spark.

The phenomena shown in Fig. 5.4 (a) are summarised in (b). The flame kernel can ignite (b, i) or quench by distinct modes which are characterised by their time scales:

(ii) long and (iii) short mode of ignition failure, as defined by Mastorakos [Mastorakos, 2017]. Examples of events where ignition and long and short mode failure were observed are shown by means of OH* and schlieren visualisation sequences in Fig. 5.4c. The successful ignition attempt was seen both in the OH* and in the schlieren sequences as a kernel that grew radially and advected downstream (upward). In the failed attempts, the OH* signal decreased to zero, although in some events the schlieren sequence showed some growth of the spherical region due to the heat transfer between the non-reacting hot gas kernel and the surrounding flow. Additionally, the uneven OH* signal distributed within the kernel with small regions of high concentration, suggests that for this case of low prevaporisation the flame was characterised by individual droplet burning as well as flame propagation through the interdroplet spacing. For a similar condition, DNS [Neophytou, Mastorakos and Cant, 2012] showed that successful ignition was due to the proximity of the droplets at the spark region, which then generated a flame front that vaporised the fuel ahead of it creating a flammable interdroplet spacing and, therefore, characterised by small areas of high heat release in the vicinity of droplets and large areas of low heat release in the interdroplet spacing.

The majority of short-mode failure events were characterised by an initially low OH* signal in the kernel (Fig. 5.4c, iii), indicating low temperatures and heat release rates following the deposition of energy by the spark. This mode of ignition failure was observed in [Wandel et al., 2009; Wandel, 2014] and attributed to a locally lean mixture and consequently small size of the kernel, which did not allow for thermal runaway to occur despite the initial temperatures above the adiabatic flame temperature. In this case, for ignition to occur, a higher spark energy would be required [Chakraborty and Mastorakos, 2008]. Long-mode failure events commonly presented higher values of OH* immediately after the spark in the present experiments, indicating that combustion took place. In such cases, failure to ignite has been attributed to the presence of liquid either within the core or close to the flame front [Wandel, 2014], preventing the flame from propagating due to intense local evaporative cooling.

A precise experimental evaluation of the quenching time scales of short and long mode failure events depends on the definition of the time scale of the spark itself. Although the duration of the laser pulse was between 4-6 ns, the resulting effects of the spark on the flame were longer than the time scale of the plasma, the latter being typically 1 µs [Gebel et al., 2015*b*]. Thus, a critical time t_{crit} was defined as the time at which the effects of the spark overdriving the chemical reactions in the flame have decayed. This time scale has been measured previously in gaseous mixtures based on

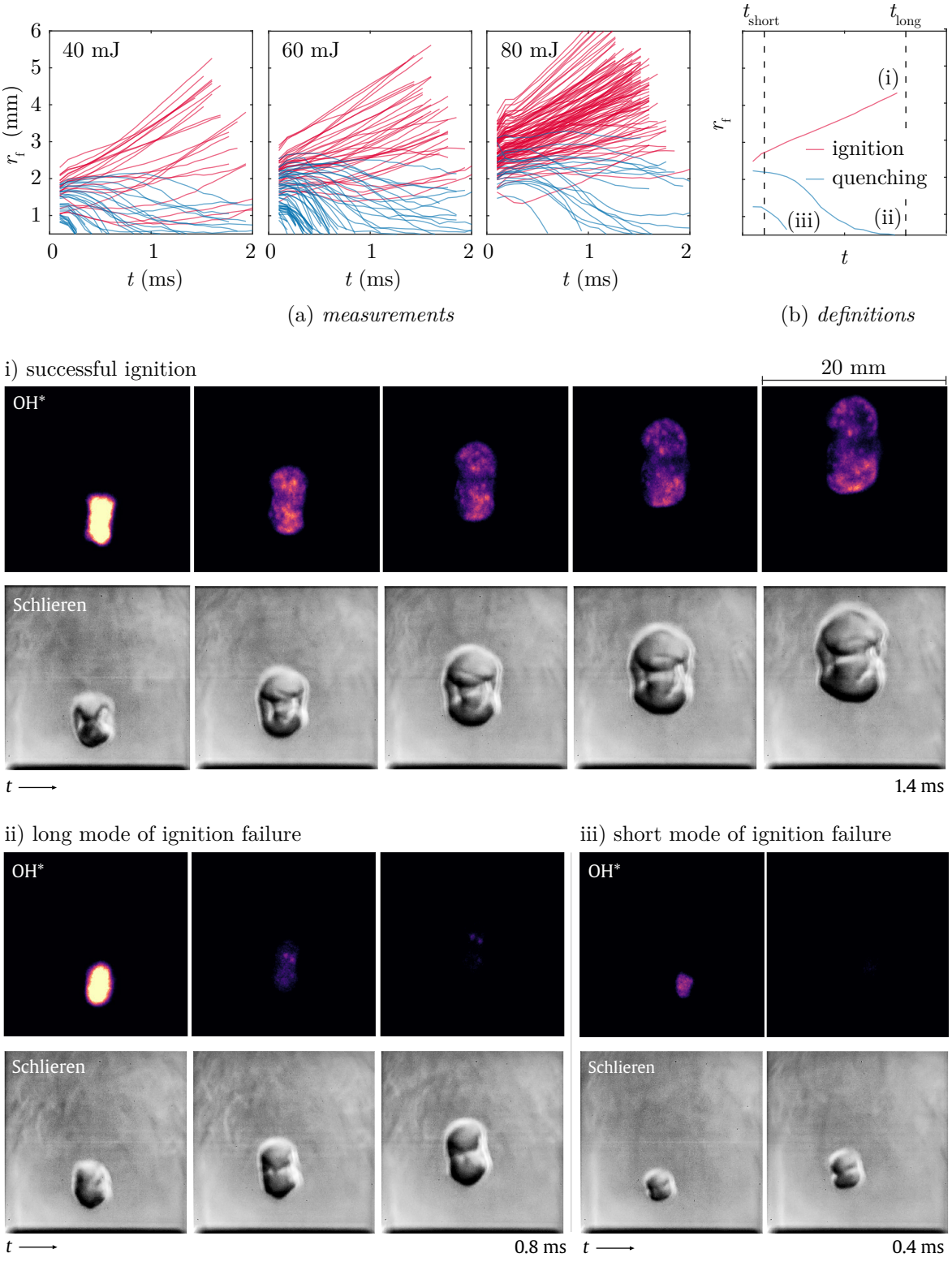

Fig. 5.4 Example of (a) a series of successful (red) and failed (blue) ignition attempts in an ethanol spray based on the growth of the kernel radius r_f for various levels of laser energy – ethanol, $U_b = 6\,m/s$, $\phi = 1$, $T_{in} = 30\,°C$. Three events given in (b) comprising one successful ignition event (i) and two failed ignition events (ii,iii) are shown in (c) by means of schlieren and OH* visualisation.

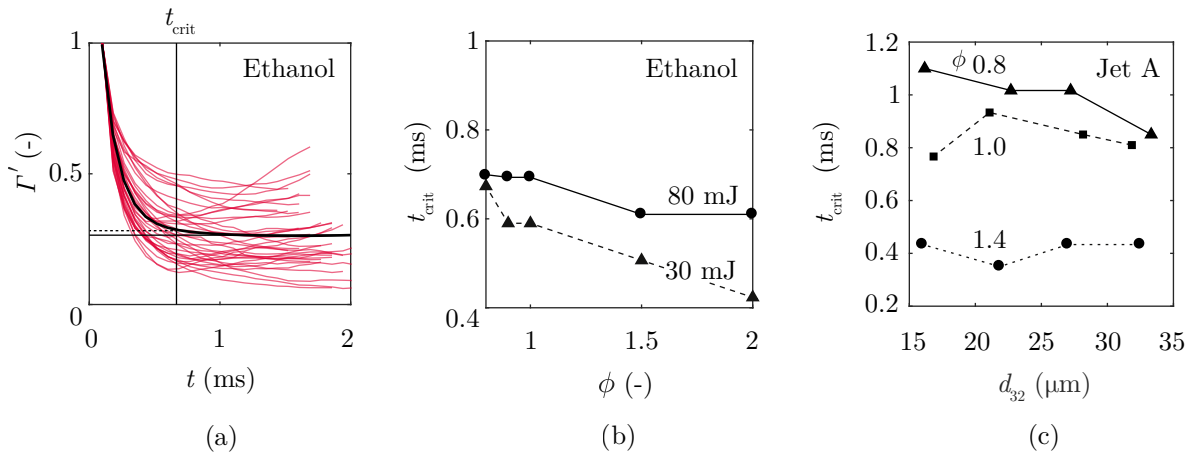

Fig. 5.5 Calculation of t_{crit} based on the normalised density of the OH* signal over time (ethanol, $U_b = 6\,m/s$, $\phi = 1$, $T_{in} = 30\,°C$, $E_{in} = 60\,mJ$), (b) t_{crit} in terms of equivalence ratio for the lowest and highest ignition energy cases in ethanol sprays (ethanol, $T_{in} = 50\,°C$), and (c) t_{crit} in terms of d_{32} for Jet A sprays (Jet A, $E_{in} = 20\,mJ$).

radical emissions [Beduneau et al., 2009; Cardin et al., 2013], and defined as a net increase of chain-branching reactions in the flame kernel following the decrease in radical emissions occurring during the plasma-cooling dominated phase. The parameter t_{crit} was used to distinguish between the two modes of failure: events that were shorter or longer than t_{crit} were defined as being of short-mode and long-mode failure, respectively. It should be noted that the present evaluation of t_{crit} does not account for additional gas dynamic effects [Bradley et al., 2004] that may enhance the propagation of the flame.

In the present work, the chemiluminescence of the OH* radical was used as an indicator of the reaction rate of the flame [Hardalupas and Orain, 2004], so that t_{crit} could be evaluated. Figure 5.5a shows the normalised OH* density, Γ', for a specific test condition and multiple ignition events. This parameter was evaluated as,

$$\Gamma'(t) = \frac{\Gamma}{\Gamma(100\ \mu s)} \tag{5.1}$$

$$\Gamma(t) = \frac{1}{A_f} \int_{A_f} I_{OH^*} \mathrm{d}A \tag{5.2}$$

where I_{OH^*} represents the intensity of the OH* radical as imaged by the camera sensor. An average curve of Γ' was evaluated, and t_{crit} was calculated as the time at which Γ' has reached 1% of its asymptote value, meaning the spark effects were no longer acting on the flame at this point.

Figure 5.5b shows an effect of the spark on the ethanol spray flame up to until 0.7 ms after the spark, as in the case of the leanest equivalence ratio and highest laser energy. This value was lower than the chemical time scale of the flame calculated for the present experiment, $t_f \cong 1$ ms, evaluated as δ/S_L°. The overdrive effect was also assessed in DNS [Wandel et al., 2009] based on the temperature of the kernel, and showed that within $0.6t_f$ from the maximum temperature of the kernel normal adiabatic flame temperatures were reached for cases of ϕ varying from 0.5 to 1.5. In the present experiments, the overdrive effect was verified to be of very similar duration, ranging from 0.4 to $0.7t_f$. Nevertheless, values of t_{crit} were found to be slightly higher for cases with high energy (80 mJ), decreasing with overall equivalence ratio especially for low energy cases. Additionally, t_{crit} in ethanol sprays were longer than those reported by [Cardin et al., 2013] for an air-methane mixture, which were approximately 200 µs for ϕ between 0.7 and 1 [Cardin et al., 2013]. In contrast, Jet A sprays presented generally longer t_{crit} (Fig. 5.5c) than ethanol sprays (b). Still, a negative correlation of t_{crit} with equivalence ratio was also observed for Jet A while the effect of droplet size seemed less relevant, suggesting that the total amount of liquid at the spark location and the associated energy needed for phase change are crucial in this process.

5.3 Statistics of time scale and kernel size

Distributions of initial kernel size for ethanol sprays are shown in Fig. 5.6 for conditions of low preheat temperature and bulk velocity of 6 m/s. The probability density functions of kernel size were estimated from the data histogram and plotted separately according to ignition or quenching depicted in shades of red and blue, respectively, and according to ϕ. The density curves were obtained through the Parzen-Rosenblatt window method [Rosenblatt, 1956; Parzen, 1962], which allows for the representation of the histogram shape, as this method does not assume an underlying distribution of the dataset. Additionally, each probability density function (pdf) was scaled by the number of events observed in the respective class (ignition or quenching), N_e. Hence, the integration of the resulting curve over the horizontal-axis parameter simply leads to N_e as opposed to unity. A strong dependency of the initial kernel size with E_{in} was observed, with kernel size increasing in almost three times as energy increased from 30 to 80 mJ. Also, a minimum kernel size for ignition was observed for $E_{in} = 30$ to 60 mJ, being approximately 1 mm. This value closely agrees with the theoretical minimum kernel size for a spherical kernel in a gaseous mixture [Spalding, 1979], defined as

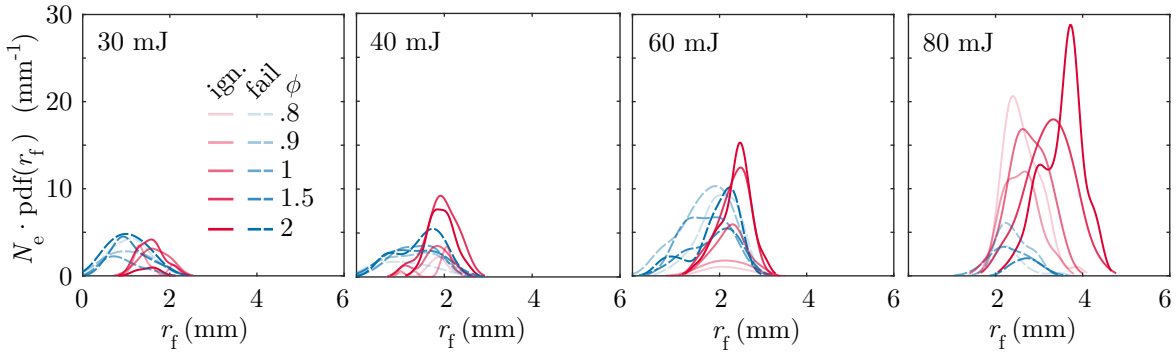

Fig. 5.6 Influence of ignition energy and equivalence ratio on initial kernel size distribution and ignition – ethanol, $U_b = 6\,\mathrm{m/s}$, $T_{in} = 30\,^{\circ}\mathrm{C}$, 120 ignition attempts per condition.

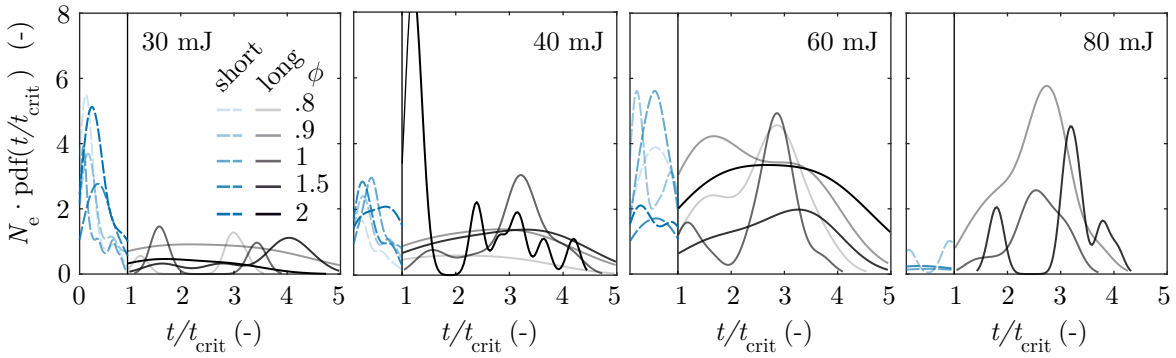

Fig. 5.7 Distributions of short and long mode of ignition failure time scales for various energy levels and equivalence ratios – ethanol, $U_b = 6\,\mathrm{m/s}$, $T_{in} = 30\,^{\circ}\mathrm{C}$, 120 ignition attempts per condition.

two times the flame thickness ($\delta \cong 0.5\,\mathrm{mm}$, for an equivalent gaseous stoichiometric mixture). Such limit was not observed for 80 mJ, as the sparks led to kernels larger than 1.5–2 mm. For this level of incident energy, the long-mode of ignition failure was observed and will be discussed next. In general, the effect of equivalence ratio on the initial kernel radius seemed to affect mostly the total number of events, but not the range of kernel sizes. However, for 80 mJ, there is a clear dependency of r_f, which increased with ϕ.

Further, Fig. 5.7 shows pdfs of ignition failure time scales normalised in terms of t_{crit}, also for ethanol sprays. In each plot, the density curve was scaled by the respective N_e in each class, either short and long mode, depicted in shades of blue and grey, respectively, according to ϕ. Results show substantial change from short to long-mode failure as E_{in} increased, with short-mode quenching being fully suppressed at 80 mJ. Additionally, in experiments with preheating of 50 °C both short and long mode failures

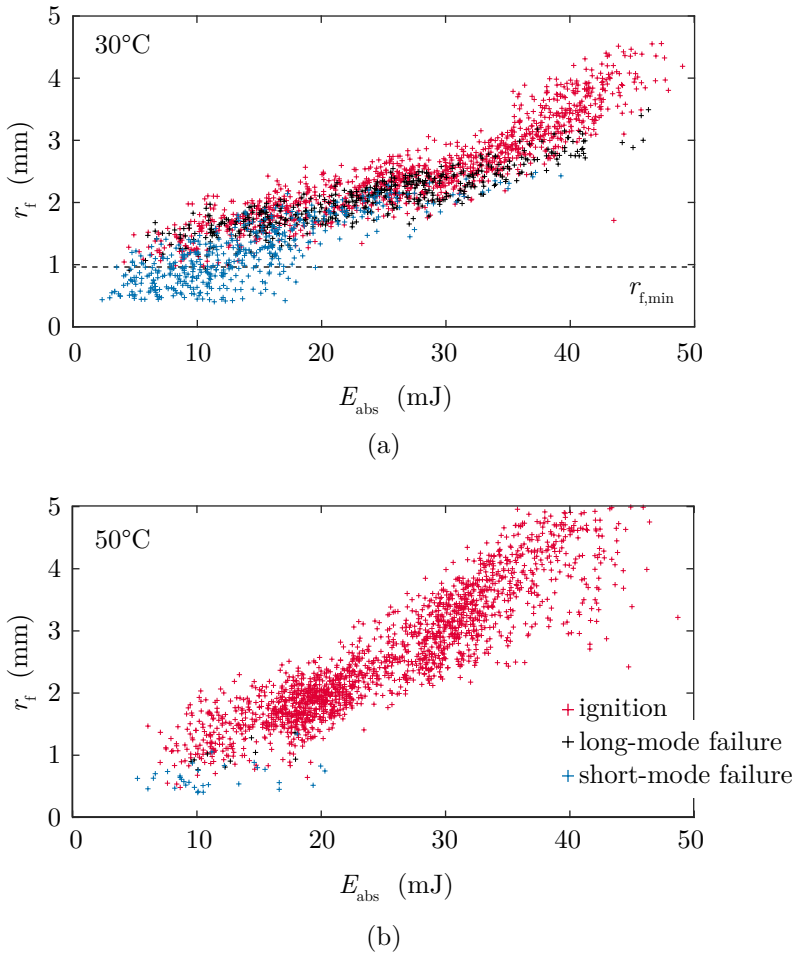

Fig. 5.8 Initial kernel size in terms of the absorbed energy for preheat temperatures of (a) 30 °C and (b) 50 °C – ethanol, $U_b = 6\,m/s$

were scarce, as failure to ignite the flow was almost exclusively due to failure to break down the mixture. This will be discussed in Sec. 5.4.

The relation between the absorbed laser energy E_{abs} and the initial radius of the flame is given by Figure 5.8 for all experimental conditions concerning ethanol sprays. In this figure, red markers represent ignition events, and blue and black markers represent short and long-mode failure events, respectively. For the low preheating condition (Fig. 5.8a), the presence of the minimum kernel radius for values below E_{abs} 20 mJ can be clearly noticed. Nevertheless, the presence of short-mode failure events for values of r_f above the minimum size and up to more than twice that value indicate that low reaction rates (Fig. 5.4) and other mechanisms other than the initial kernel size may also have resulted in short-mode failure in the present experiment.

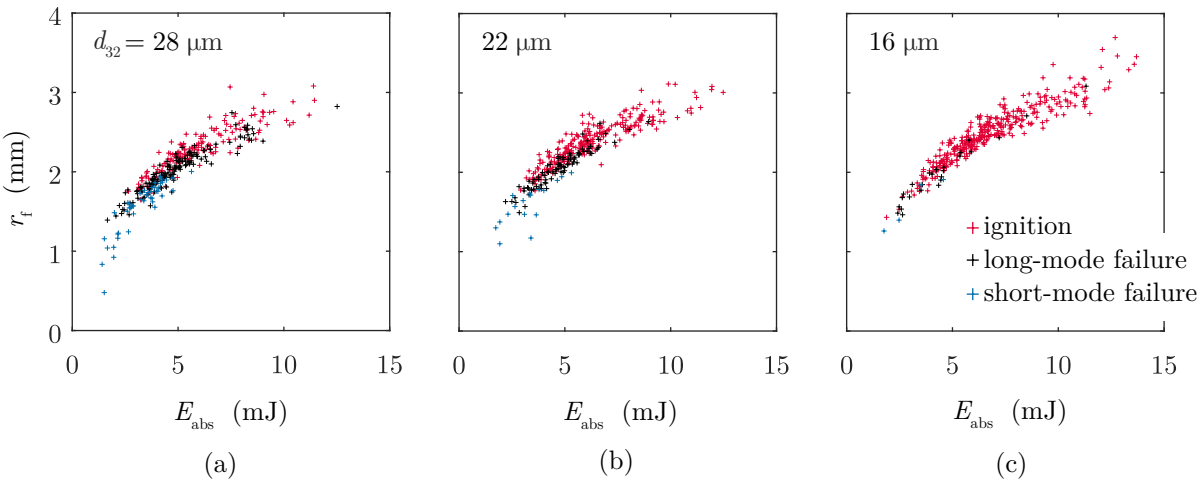

Fig. 5.9 Initial kernel size in terms of the absorbed energy and droplet sizes of (a) 28 µm, (a) 22 µm, and (a) 16 µm – Jet A, ϕ =1, E_{in} = 20 mJ.

Figure 5.8 presents a positive correlation between the initial radius of the flame and the outcome of the ignition event, showing that the number of ignition events increases with the initial kernel radius. Additionally, a suppression of all quenching modes was observed once the preheating temperature was increased to 50 °C, that is, as the equivalence ratio of the gas phase increased to approximately 0.5, being closer to the lower flammability limit of 0.66. The effects of the kernel radius and prevaporisation indicate that the presence of a flammable mixture in the spark location is determining to ignition, as shown in DNS [Neophytou et al., 2010]. The probability of finding a flammable mixture in the spark not only increases with prevaporisation, but should also increase with the spark size as a large spark will experience less fuel fluctuations. This affects polydisperse sprays, in which a significant fraction of the injected fuel is carried by large droplets which are scarce in the flow, as shown in Fig. 4.10 of Sec. 4.3, and modelled in Chapter 7. Further evidence of this effect is shown in experiments with Jet A sprays in Figure 5.9, where a suppression of short and long modes of ignition failure occurred as the SMD of the spray decreased, while the the relation between absorbed energy and initial kernel radius remained similar for the three cases.

5.4 Probabilities of ignition

The probabilities of breakdown and of ignition for ethanol sprays in terms of the equivalence ratio are shown in Fig. 5.10. For ignition energies between 30 and 60 mJ, an increase in equivalence ratio generally resulted in an increase of P_{bd}. Such behaviour was expected, as it is known that the presence of droplets along the beam path can act as micro lenses facilitating breakdown around the focusing point of the beam [Müsing et al., 2007]. Therefore, increasing the total amount of liquid, which effectively led to an increase of the droplet number density, enhanced the probability of breakdown, or P_{bd}. However, this effect was balanced by energy losses along the beam path between the focusing lens and the ignition location, being detrimental to P_{bd}. The lost energy as the laser beam crosses the flow was estimated from the mean value of E_{abs} conditional to events where no breakdown was observed, shown in Fig. 5.11. The results indicate the competing effects described previously, showing that losses increased with equivalence ratio and also with preheating temperature – the latter being likely associated with the suppression of the droplet-enhancement effect of breakdown, which increased the average breakdown threshold.

An estimate of the actual energy deposited at the focusing point, E^{*}_{abs}, was evaluated by taking the mean value of E_{abs} conditional to events where no breakdown was observed and subtracting it from the mean value of the same parameter conditional to events corresponding to breakdown. These values are reported in Fig. 5.12 for ethanol sprays. Nevertheless, it should be noted that large experimental uncertainties associated with the evaluation of E^{*}_{abs} are expected as a result of the combined uncertainty deriving from the energy measurements (1–4 mJ), as well as due to the random variations of the measured and derived parameters inherent of such experiments in sprays, as illustrated previously in Fig. 5.3. Values of E^{*}_{abs} varied between 1 and 20 mJ in the experiments, while the threshold energy for breakdown of air and fully-prevaporised ethanol–air mixtures was measured (P_{bd}=0.5) as approximately 8.5 mJ. This seems to explain the effect of prevaporisation on P_{bd} (Fig. 5.10), as increasing prevaporisation resulted in an overall higher P_{bd} for high E_{in}, but lower P_{bd} for low E_{in}. For E_{in} resulting in a deposited energy in the focusing point below the breakdown energy for the gaseous mixture, the creation of a flame kernel relied on the presence of droplets to promote breakdown. Therefore, P_{bd} decreased as the smallest droplets of the flow fully vaporised with preheating, resulting in a significantly lower droplet number density. In contrast, a high E_{in} was not affected by prevaporisation, hence a unity P_{bd} was verified

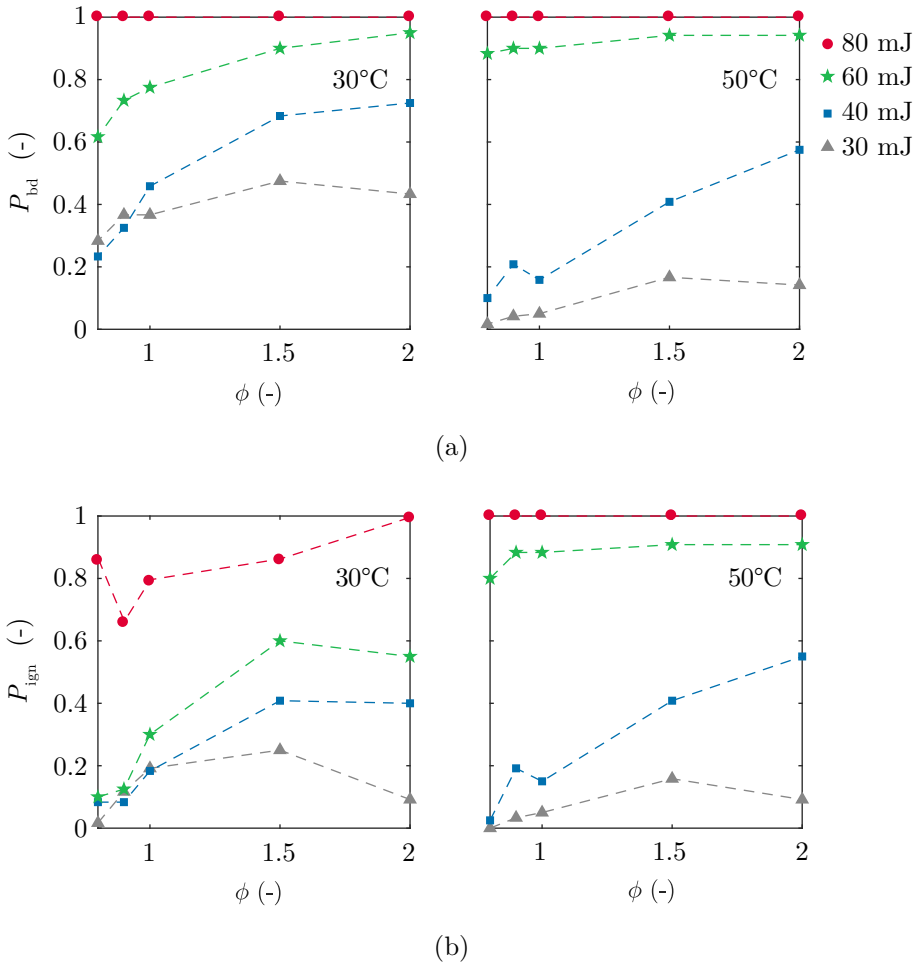

Fig. 5.10 Probabilities of (a) breakdown and (b) ignition for ethanol, $U_b = 6\,\mathrm{m/s}$ and $T_{in} = 30, 50\,^{\circ}\mathrm{C}$.

for 80 mJ and all ϕ. It should be noted that consistently-defined MIE for ethanol vapour at the conditions studied (p,T) was not available, and so a direct comparison with gaseous-only systems is not possible at present. Still, the trends with preheating provide useful insight.

Figure 5.10 also shows that lean conditions with low prevaporisation required the highest energy to ignite, which agrees with DNS [Chakraborty and Mastorakos, 2008]. Increasing E_{in} from 30 to 60 mJ gradually facilitated the formation of kernels, but their subsequent quenching was still verified, hence resulting in virtually no changes to P_{ign}. Furthermore, only a significant increase of the ignition energy to 80 mJ was effective in suppressing quenching. Increasing the amount of prevaporised fuel in lean conditions decreased this threshold to 60 mJ, as more of energy due to combustion was available to overcome evaporation and less fuel was present as liquid. Further, the minimum ignition energy evaluated as $E^{*}_{abs}(P_{ign}{=}0.5)$ is shown in Fig. 5.12. A

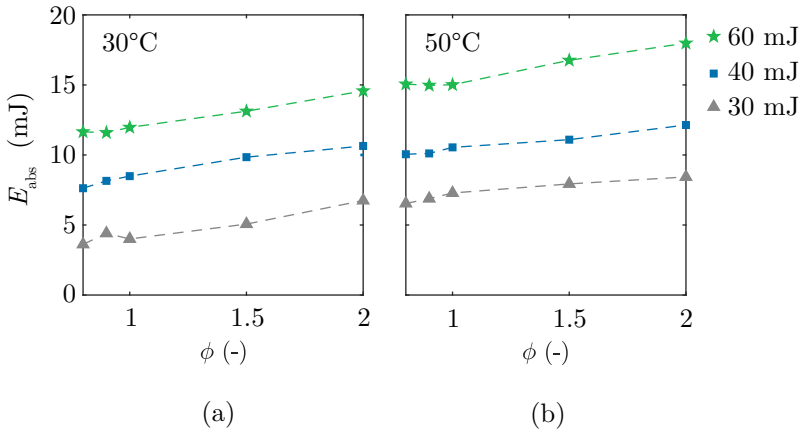

Fig. 5.11 Mean value of E_{abs} conditional to no-breakdown events, representing energy losses along the beam – ethanol, $T_{in} = 30$ and 50 °C, $U_b = 6$ m/s

consistent value of approximately 3.5 mJ was obtained for high prevaporisation and lower d_{32}, while higher values between 4 and 14 mJ were observed for conditions of low prevaporisation. For high prevaporisation, little effect of ϕ on P_{ign} was noticed, as the mixture in the interdroplet region was close to flammable and failure of the kernel did not occur once it was formed. For both conditions (a) and (b), the obtained MIE is higher than the theoretical limit of 1.5 mJ evaluated according to Spalding [1979], which has been attributed not only to the effects of spray and turbulence, but also due the added energy released in the form of a shock wave [Gebel et al., 2015*a*].

The effect of turbulence on P_{bd} is shown in Fig. 5.13. Significant changes were mostly noticed for a low ignition energy (30 mJ), where the effect of turbulence seemed strongly detrimental to P_{bd}. As E_{in} increased, resulting in larger kernels, this effect became less pronounced and completely vanished once energy reached 80 mJ. It should be noted that other than the effect of turbulence, some decrease of ϕ_g is expected as $\langle u'_{z,g} \rangle / S^{\circ}_{L,st}$ increases due to changes of the residence time of the droplets inside the burner. Further work is needed with higher turbulence and controlled ϕ_g to allow for a more detailed analysis.

Finally, an investigation of the effect of droplet size and polydispersity of the spray on the establishment and subsequent growth of a flame kernel was carried out for the two jet fuels, Jet A and ATJ-8, and is shown in Fig. 5.14. Although the overall, expected effect of increasing droplet size was to suppress ignition, an enhancement of ignition probability of Jet A was observed for the lean case and coarse atomisation, for conditions close to MIE. The presence of large droplets in the spark location or its

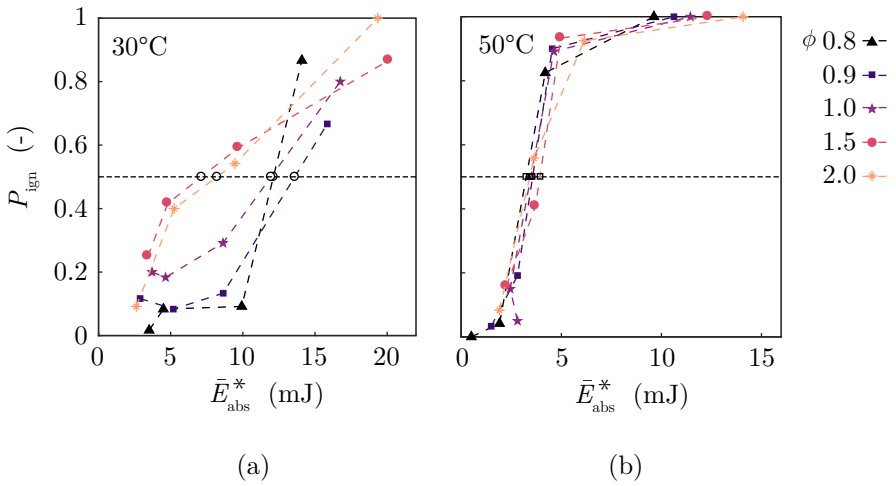

Fig. 5.12 Probability of ignition in terms of the energy deposited at the spark location, E^*_{abs}, for ethanol sprays at various equivalence ratios and (a) $T_{\mathrm{in}} = 30\,^{\circ}\mathrm{C}$ and (b) $50\,^{\circ}\mathrm{C}$ ($U_{\mathrm{b}} = 6\,\mathrm{m/s}$). Minimum ignition energy is shown as $E^*_{\mathrm{abs}}(P_{\mathrm{ign}} = 0.5)$ for each condition.

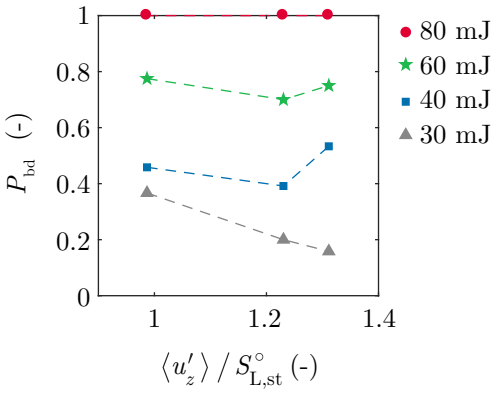

Fig. 5.13 Probability of breakdown and ratio of probability of ignition in terms of probability of breakdown – ethanol, $U_{\mathrm{b}} = 6$, 9, and $12\,\mathrm{m/s}$; $T_{\mathrm{in}} = 30\,^{\circ}\mathrm{C}$.

immediate vicinity, resulting in individual droplet burning, seemed crucial to allow for flame propagation following the establishment of a kernel in such cases. This issue is discussed in detail in Chapter 6. Similar to the experiments in ethanol sprays, the energy to ignite a lean mixture was also significantly higher than to ignite a stoichiometric and a rich case, as expected and verified in previous DNS studies [Chakraborty and Mastorakos, 2008]. ATJ-8 in lean conditions required higher laser energies than Jet A, and less energy as the equivalence ratio increased to stoichiometric and rich conditions. In the rich cases, little variation of $P_{\mathrm{ign}}/P_{\mathrm{ker}}$ of Jet A was verified between 10 and 20 mJ, while 10 mJ was enough to lead to a 100% ignition, given a kernel was formed,

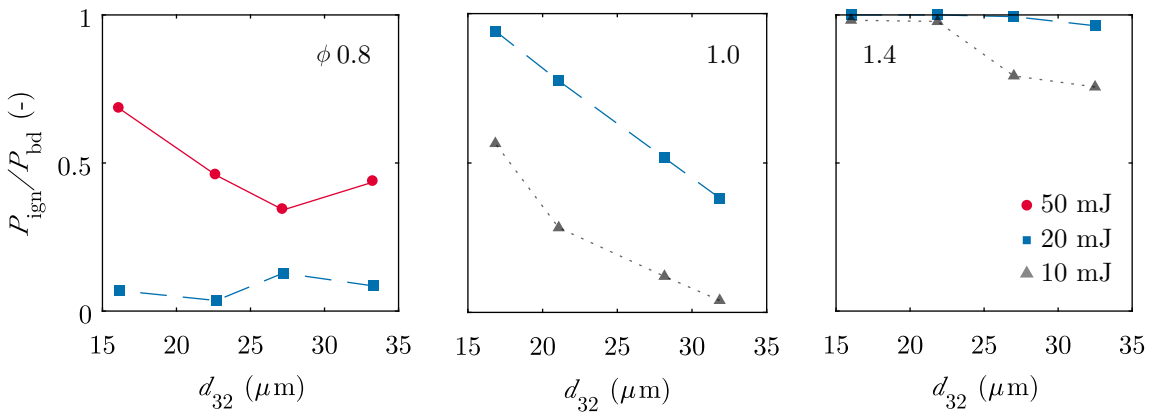

(a) Jet A

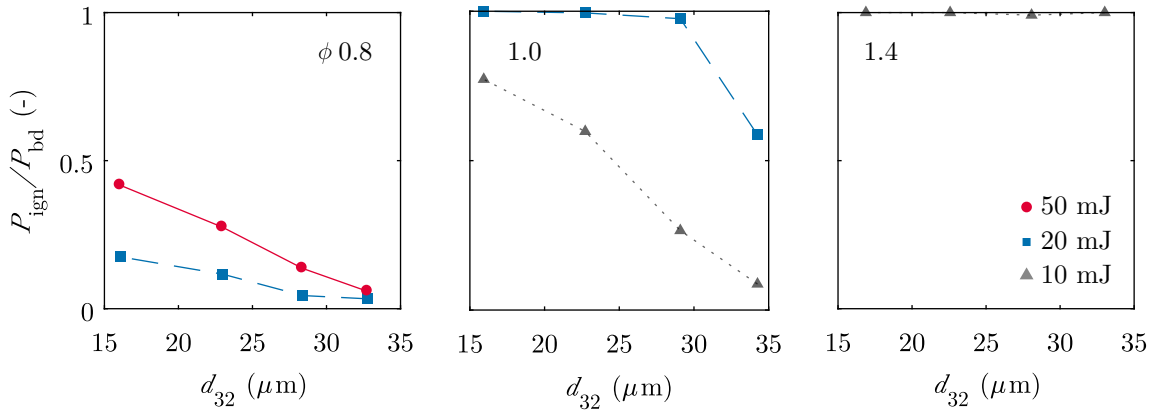

(b) ATJ-8

Fig. 5.14 Probability of ignition given breakdown for (a) Jet A and (b) ATJ-8 in terms of d_{32}.

in ATJ-8 sprays. This occurred even in conditions of coarse atomisation. Below 10 mJ, breakdown of the mixture was not achieved.

5.5 Summary

This chapter presented a statistical assessment of spray ignition processes by means of OH* imaging of spherically expanding flames initiated by a laser spark. Ignition probabilities and probability density functions of kernel size and time scales of ignition failure were given in terms of spray and spark characteristics, providing evidence of the effect of the droplets on the ignition process. Small kernels below a minimum size failed to ignite, quenching immediately after the spark. Ignition was strongly associated with the initial kernel size and, therefore, with the absorbed energy, given that breakdown

of the mixture occurred in conditions of low prevaporisation. Still, intermediate kernel sizes exhibited all types of ignition behaviour. Ignition was only guaranteed by high-energy sparks leading to large kernels, or by increasing fuel prevaporisation leading to a gas-phase equivalence ratio nearly flammable.

Chapter 6

Flame propagation mechanisms

6.1 Motivation and objectives

The propagation of a flame across a droplet mist has been typically modelled as a combination of individually burning droplets and homogenous reaction in a gaseous mixture [Polymeropoulos, 1984]. This combined propagation mechanism was suggested by early experimental works, which visualised the effect of droplets on the flame strucgture from macro-scale visualisations of the flame [Burgoyne and Cohen, 1954; Čekalin, 1961; Mizutani and Ogasaware, 1965]. This modelling approach has led to a significant improvement of the model originally proposed by Ballal and Lefebvre [1981*b*] especially at conditions of small droplet size, which are known to enhance flame speed either in relation to even finer sprays and, at times, even above the flame speed of an equivalent gaseous premixed flame [Burgoyne and Cohen, 1954; Mizutani and Nakajima, 1973*a*; Polymeropoulos and Das, 1975; Hayashi et al., 1977; Richards and Lefebvre, 1989; Nomura et al., 2007]

The contrasting experimental results on flame speed in the presence of droplets, as well as the lack of detailed information on the flame structure due to the complexities involved in carrying out well-controlled spray experiments, motivated a number of DNS works on this topic. The droplet-scale structure of the flame has been observed in 3-D DNS of spherically expanding flames with simplified [Wandel et al., 2009; Neophytou et al., 2010; Ozel Erol et al., 2018, 2019] and complex chemistry [Neophytou, Mastorakos and Cant, 2012]. In the work of Neophytou, Mastorakos and Cant [2012], two flame

The results of this chapter have been published in: de Oliveira, P.M., Mastorakos, E. [2019], 'Mechanisms of flame propagation in jet fuel sprays as revealed by OH/fuel planar laser-induced fluorescence and OH* chemiluminescence', *Combustion and Flame* **206**, 308–321.

propagation mechanisms were identified by the authors, namely the droplet and the inter-droplet ignition modes, as defined by Čekalin [1961]. The droplet ignition mode was observed in dilute sprays with Group number [Chiu and Liu, 1977] $G < 6$ and exhibited propagation of the flame through bridges of mixture fraction connecting the droplets. Additionally, reaction was observed in a below-flammable inter-droplet space, which seemed to be driven by diffusion of heat and species from individually burning droplets. For dense sprays (G=20), a more homogenous flame front was observed due to strong droplet evaporation occurring in the pre-heat layer of the flame, leading to reaction occurring mostly in near-stoichiometric mixture fraction conditions.

A number of droplet-scale phenomena have been identified to affect flame propagation, such as the presence of mixture inhomogeneities at the droplet scale, as well as droplet-induced increase of flame surface area due to wrinkling [Mizutani and Nakajima, 1973*b*; Hayashi et al., 1977; Nomura et al., 2007; Thimothée et al., 2017]. Further, an effective equivalence ratio was defined as the actual equivalence ratio at the inter-droplet space resulting from fuel evaporation between the fresh mixture and the high-temperature region ahead of the flame [Hayashi et al., 1977]. The importance of this parameter was shown in DNS, as enhanced propagation in relation to gaseous mixtures occurred mostly for an stoichiometric effective equivalence ratio [Neophytou et al., 2010; Neophytou, Mastorakos and Cant, 2012; Wacks et al., 2016; Nicoli et al., 2016]. The contribution of droplet-induced curvature spray flames was verified to increase with droplet size of the spray, both in laminar and turbulent conditions, although increasing turbulence seemed to eclipse the contribution of the droplets to wrinkling [Ozel Erol et al., 2018, 2019]. Droplet penetration through the flame occurs once droplets become large, leading to additional fuel influx once these reach the burnt products side and evaporate [Wandel et al., 2009; Wacks et al., 2016], possibly undergoing pyrolysis in that region due to high temperatures [Neophytou, Mastorakos and Cant, 2012]. These effects were also associated to high flame speeds in sprays. Experimentally, some evidence of droplet penetration for spherically expanding flames has been verified in experiments through schlieren [Bradley et al., 2014] and by tracking the sudden change of velocity of ethanol droplets as they crossed the flame [Thimothée et al., 2017]. At those conditions, triggering of Darrieus-Landau instabilities leading to flame wrinkling was observed through schlieren and associated with the droplet penetration [Thimothée et al., 2017].

Thus far, there has been no experimental droplet-scale visualisation of the interaction between the droplets and the flame nor experimental evidence of the propagation mechanisms in turbulent spray flames and the range of conditions in which they occur. Typically, DNS has been used to investigate these aspects of spray flames, but this approach is limited due its modelling assumptions of the spray and the combustion chemistry, often not meeting certain conditions relevant to real applications. Advanced diagnostics provide an opportunity of measurements to be taken at droplet scale in canonical experiments while featuring polydiserse sprays and complex multi-component fuels – two aspects especially relevant to gas turbine combustion. In this part of the thesis, the problem of flame propagation in sprays is addressed as follows,

- The problem of a spherically expanding flame is investigated by initiating a flame in a uniformly distributed droplet field advected by a weakly turbulent flow with constant mean velocity. In addition to global conditions in which ignition is more likely to occur, experiments include flow conditions in which ignition failure is more frequent (e.g., lean sprays with large droplets).

- Unburnt flame speeds are evaluated from OH*-chemiluminescence imaging for conditions of self-sustained propagation, that is, at times longer than the effect of the spark on the flame, as discussed in Chapter 5. The effects of droplet size, overall equivalence ratio, and fuel prevaporisation on the flame speed are investigated.

- The structure and propagation mode of the flames are visualised at the droplet scale using OH*-chemiluminescence, schlieren, and simultaneous OH/fuel planar laser-induced fluorescence.

- Finally, the impact of the droplets on the flame structure is evaluated through the two-dimensional flame curvature under different propagation mechanisms.

This investigation is carried out in jet fuel sprays, as these fuels feature the key characteristics of spray flames due to their low volatility and are the most relevant to gas-turbine applications. At the end of this chapter, a validation of the measurement technique is carried out in laminar premixed methane-air flames. Additionally, flame speed data for ethanol sprays is also given for completion.

6.2 Flame speed and flame characteristics

The effect of the spray SMD on the unburnt flame speed of Jet A and ATJ-8 is shown in Fig. 6.1a. The measurements were also given in terms of the overall equivalence ratio of the mixture for comparison with the calculated gaseous premixed laminar burning velocity (b). Overall, increasing the polydispersity of the spray and consequently its SMD was detrimental to $\overline{S}_u$ (Fig. 6.1a). This effect was verified in stoichiometric and rich mixtures of both fuels, with ATJ-8 being faster than Jet A as the SMD increased in rich conditions. Also, the measured flame speeds were generally lower than the gaseous laminar burning velocity for a mixture with the same ϕ (Fig. 6.1b). This distinct difference between $S_u(\phi)$ of the spray and $S^{\circ}_{\mathrm{L,g}}(\phi)$ indicates that one of the controlling parameters of flame speed in spray flames is the effective equivalence ratio at the leading edge of the propagating front rather than the overall equivalence ratio of the spray, ϕ, as pointed out in previous numerical works [Neophytou et al., 2010]. Thus, spray flames usually propagate at a leaner equivalence ratios than the overall equivalence of the mixture [Wacks et al., 2016; Ozel Erol et al., 2019] and may present S_u values that are significantly higher than the stoichiometric gaseous condition, as in cases with ϕ =1.4 for all atomisation conditions investigated here (Fig. 6.1b).

In addition, flame speeds higher than the estimated turbulent burning velocity were verified in these experiments. The flame speed measurements were normalised in terms of the gaseous turbulent burning velocity, which was calculated based on the laminar burning velocity and the correlation proposed in [Bradley, 1992]. For that, the respective parameters of the mixture and the flow were considered at each test condition. These results are shown in Fig. 6.1 in terms of (c) SMD and (d) $u'_z/S^{\circ}_{\mathrm{L},g}$. Flame speeds higher than $S_{\mathrm{T,g}}$ were observed for most of conditions with $\phi = 1.4$, with the highest absolute values being at fine atomisation conditions (d_{32}=16-22 μm). Other than the flame propagating at an effective equivalence ratio different from the overall value, the presence of droplets inside the flame has been observed to contribute to the high flame speed values found in previous DNS works [Wandel et al., 2009; Neophytou, Mastorakos and Cant, 2012]. This phenomenon is visualised and discussed further in Sec. 6.3. Additionally, a slight increase of $\overline{S}_{\mathrm{u}}$ with SMD (Fig. 6.1a,c) was present under lean conditions for both fuels, as opposed to the negative correlation found under stoichiometric and rich conditions. This positive effect of large droplets was verified even though $u'_z/S^{\circ}_{\mathrm{L},g}$ decreased with SMD (Fig. 6.1d). This has also been observed in

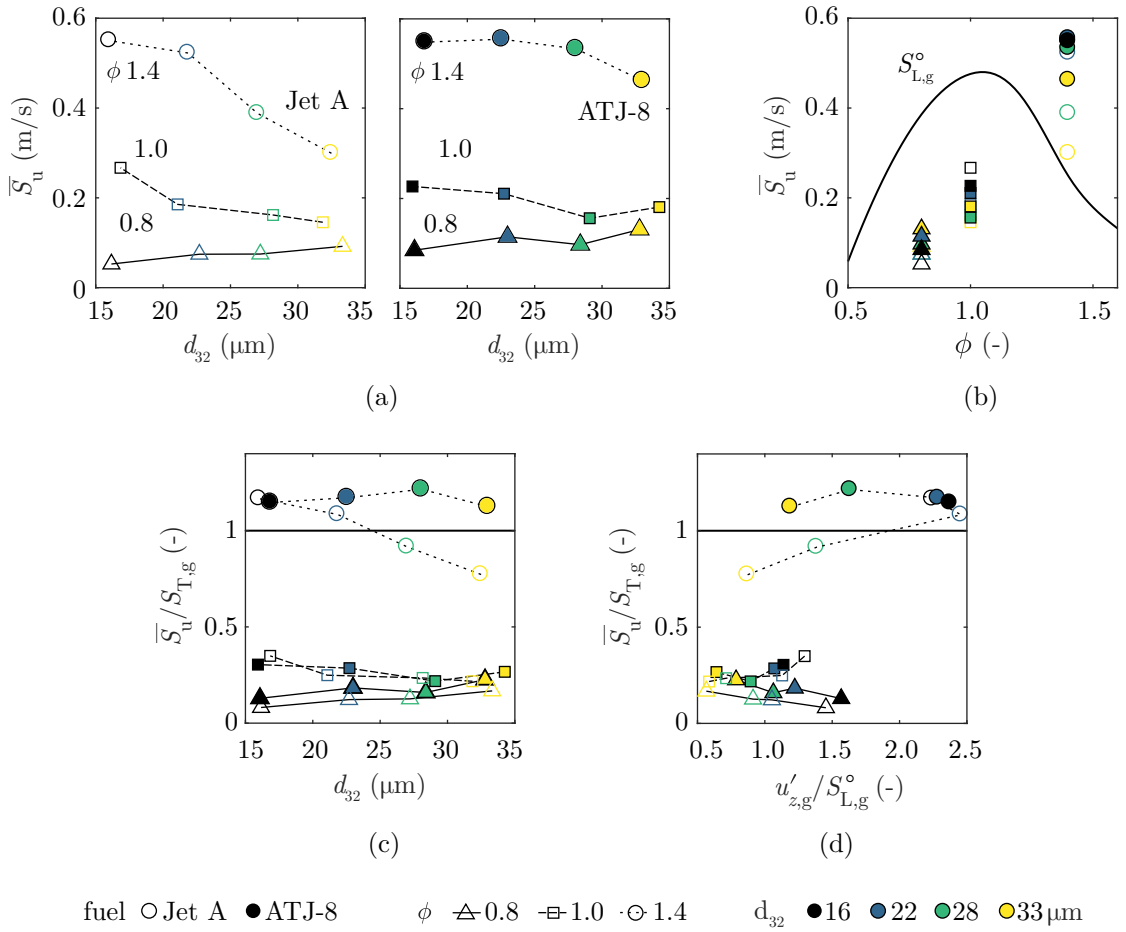

Fig. 6.1 Effect of droplet size on the unburnt flame speed of (a) Jet A and ATJ-8. A comparison against the gaseous laminar burning velocity of a 1-D gaseous premixed flame using the Dagaut chemical mechanism [Dagaut, 2002] is shown in (b). The measurements in (a) were normalised in terms of the gaseous turbulent burning velocity calculated using Bradley's correlation [Bradley, 1992] and are shown in terms of the (c) SMD and (d) $u'_{z,g}/S_{L,g}$.

other experimental works, which attributed to the inhomogeneities caused by large droplets, facilitating the flame propagation [Nomura et al., 2007].

Another important observation is that the measured flame speed in all lean conditions was distinctly low and similar to the laminar burning velocity at the lower flammability limit (Fig. 6.1b). The present results illustrate different ways in which flame speed enhancement may take place, in relation to a gaseous mixture or even a finer spray, for example. In Sec. 6.3, the mechanisms of flame propagation are discussed in detail through direct observations of the ignition event, offering visual evidence to explain the behaviours observed in Fig. 6.1.

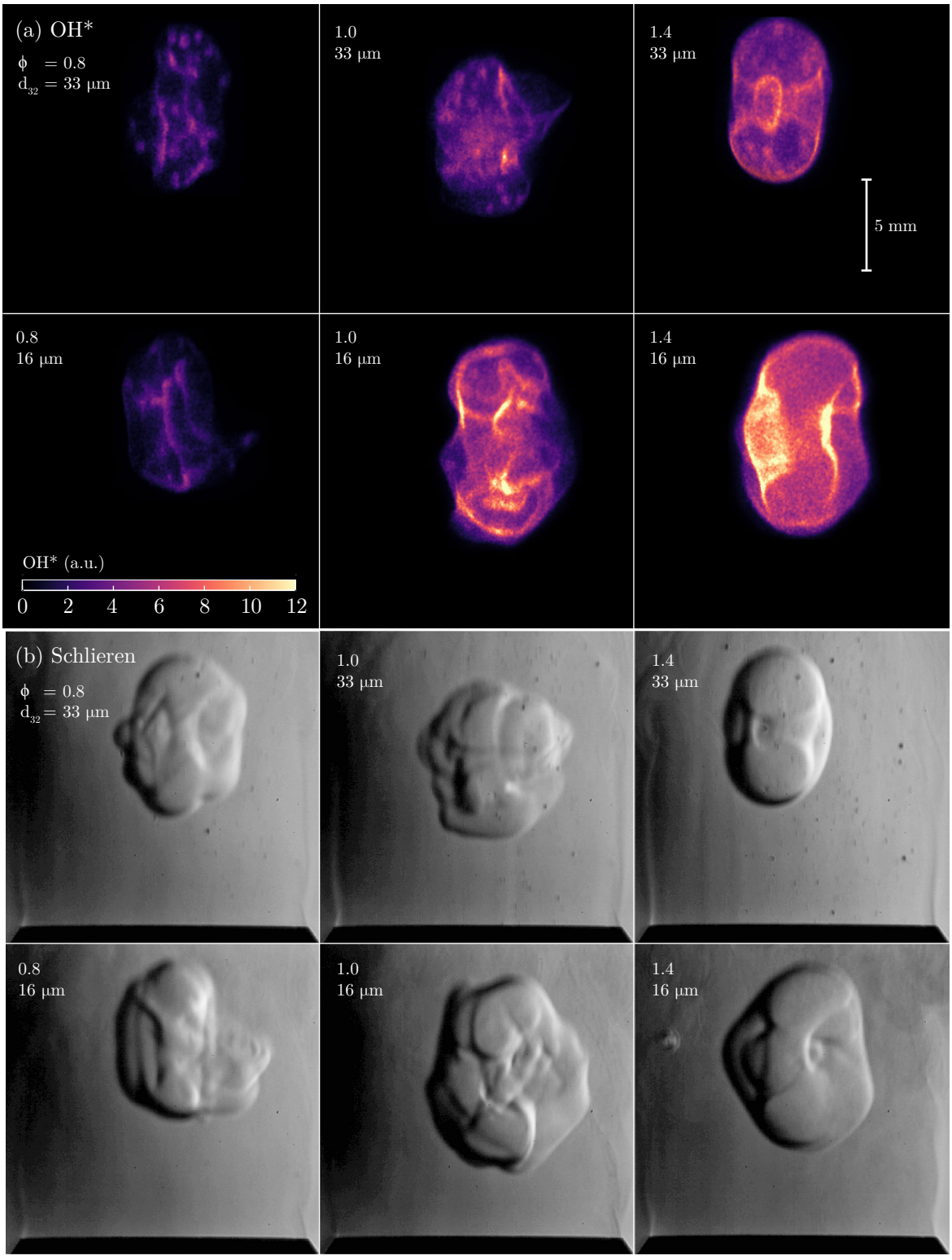

Fig. 6.2 Simultaneous (a) OH* and (b) schlieren snapshots of characteristic Jet A flames 1 ms after the spark.

Figure 6.2 shows the main characteristics of typical spray flames for the range of conditions studied. Jet A flames at 1 ms after the spark are shown through (a) OH* and (b) schlieren visualisation, with coarse (d_{32}=33 μm) and fine (d_{32}=16 μm) atomisation cases shown at the top and bottom rows, respectively, and ϕ of 0.8, 1, and 1.4 from left to right. The visualisation area shown for each flame is exactly the same between the OH* and the schlieren image, with the latter being flipped, or mirrored, in relation to its vertical axis for convenience. Also, as noted previously, the visualisation settings were kept the same during all experiments, hence the OH* signal can be directly compared between conditions.

The difference between fine and coarse atomisation can be seen in the schlieren images of Fig. 6.2b. The small black dots in the image represent the shadowgraph of large droplets in the flow (top row), while only a homogenous grey region can be seen where a monodisperse-like spray was obtained and droplets cannot be individually identified (bottom row). The presence of a polydisperse spray with high SMD gave rise to pockets of strong heat release in the flame. These are likely large individually burning droplets, as the presence of liquid fuel in that region was confirmed through PLIF visualisation. In contrast, a high heat release concentration was found in elongated regions of the flow with length of the order of L_{11}. This characteristic suggests that the highly dense OH* regions could be related to reaction occurring in clusters of droplets, as droplets with Stokes number around unity tend to accumulate due to turbulence [Eaton and Fessler, 1994]. It should be noted that such wrinkled structures were hardly found in the PLIF images due to their three-dimensional character.

6.3 Flame propagation mechanisms

Three distinct flame propagation modes were observed in the present experiments. The first was characterised by a homogenous gaseous-like flame front, which also presented aspects of the sheath combustion mode described in [Chiu and Liu, 1977]. The second propagation mode was characterised by strong reaction occurring only around large droplets. Finally, the third mode lay between the two others, exhibiting a homogenous heat release across the flame but also some zones of high heat release around large droplets. The first propagation mode is referred to as gaseous-like mode throughout this text, while the second and third mode fit the description of the droplet and inter-droplet propagation modes given by Neophytou, Mastorakos and Cant [2012] in their DNS work, thus the same terms are used.

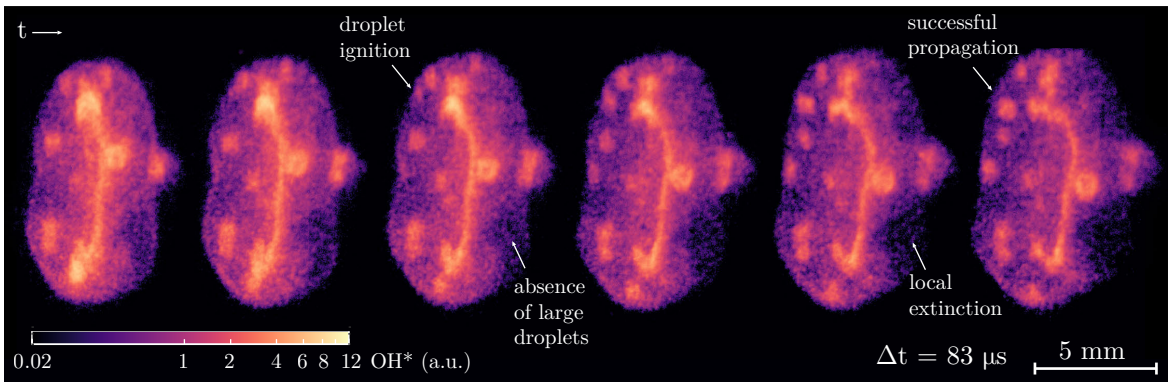

(a) OH*, event 1

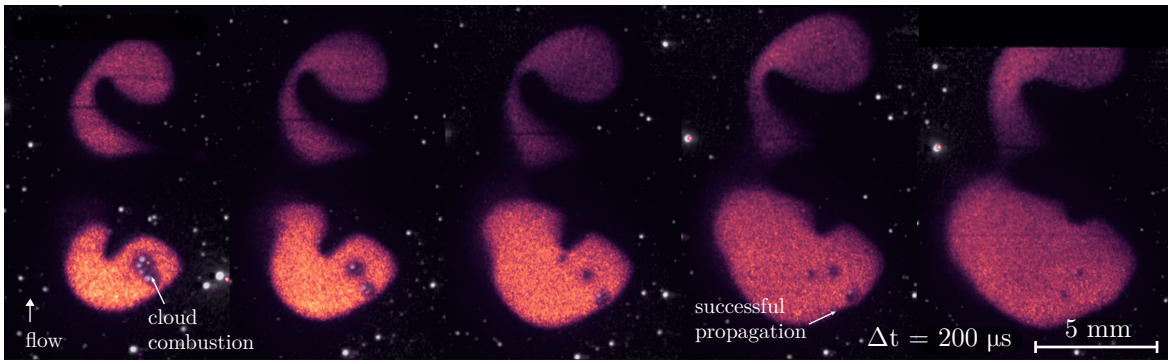

(b) OH/fuel PLIF, event 2

Fig. 6.3 Examples of droplet propagation mode visualised by (a) OH* and (b) OH/fuel PLIF – Jet A, ϕ=0.8, d_{32}=33 µm. OH* signal in (a) is shown in a logarithmic scale revealing the low heat-release zones.

Droplet propagation mode

This mode was characteristic of lean mixtures with SMD between 16-33 μm. In Fig 6.3, an OH* line-of-sight image sequence illustrates a typical event exhibiting droplet-propagation mode (a). The role of fuel droplets in such a mode can be better understood through the OH/fuel PLIF sequence of an additional event show in (b). In the PLIF images, the OH signal is shown in colour and the cube root of the fuel fluorescence signal (representing the droplet diameter) is shown in a grey scale. Due to the relatively low signal of small droplets combined to the image resolution, the smallest droplets seen in the image have an approximate size of 10-30 μm, estimated as the same order of magnitude of the sensor pixel. To allow the visualisation of very low heat release zones in (a), the OH* colour map was rescaled to a logarithmic form.

The propagation of the flame occurred preferentially through bridges between large droplets or groups of droplets, similarly to the propagation mechanism observed in a

stroichioimetric 20-μm monodisperse spray of n-heptane [Neophytou, Mastorakos and Cant, 2012]. Although the line-of-sight character of OH* experiments makes it difficult for a precise assessment of the flame front (Fig 6.3a), burning droplets seemed to have allowed for the local advancement the flame front towards the fresh mixture, which in turn ignited new large droplets. This can also be seen in the PLIF sequence (Fig 6.3b), where the flame front can be understood to lie at the leading edge of the OH-dense region, between this and the droplet field. In these regions, the flame front seemed to propagate faster than the average front, suddenly engulfing parts of the flow.

In the experiments, the propagating front surrounding the large burning droplets exhibited an especially low OH* signal, approximately ten times lower than in the vicinity of a droplet, indicating significant fuel deprivation and low heat release in those areas. Additionally, local extinction was observed in parts of the flame front lacking the presence of large individually burning droplets. These localised sources of heat release have been verified in DNS to allow for the reaction even in below-flammable inter-droplet gas phase [Neophytou, Mastorakos and Cant, 2012], which seems to be the phenomenon taking place in Fig 6.3a. However, in contrast to DNS [Neophytou, Mastorakos and Cant, 2012], droplet-mode propagation occurred only at ϕ of 0.8 for a similar d_{32}. This is likely associated to the prevaporised fuel present in the inter-droplet space ($\phi_g = 0.3$), in addition to numerous small droplets in the 1-10 μm range, which should present fast evaporation time scales. It should be noted that in a polydisperse spray, the amount of fuel accumulated in droplets that are smaller than what can be clearly resolved by the camera sensor (d<15 μm), being most of the droplets in the flow, accounted for roughly 25% of the liquid fuel mass. Considering the prevaporised fuel in the gas phase, large and scarce droplets must have accounted for approximately half of the energy released through combustion.

Moreover, the overall ignition of the flame was strongly attributed to the presence a few large droplets at the location of the spark, verified in the first few frames o the event. Typically, immediate quenching of the flame was verified in events that did not exhibited individually burning droplets following the spark. As verified in DNS of sprays [Wandel et al., 2009; Neophytou et al., 2010] and stratified gaseous mixtures [Chakraborty and Mastorakos, 2008], mixture inhomogeneities may facilitate the reaction in regions of optimal equivalence ratio, consequently enhancing the overall ignition of the flame. Thus, the slight increase in flame speed with SMD observed for both Jet A and ATJ-8 (Fig. 6.1a) may be associated with this mechanism.

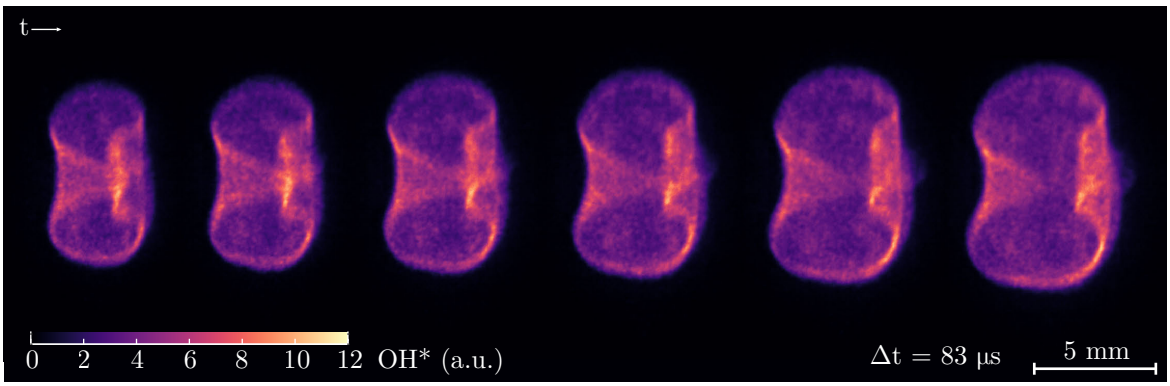

(a) OH*, event 1

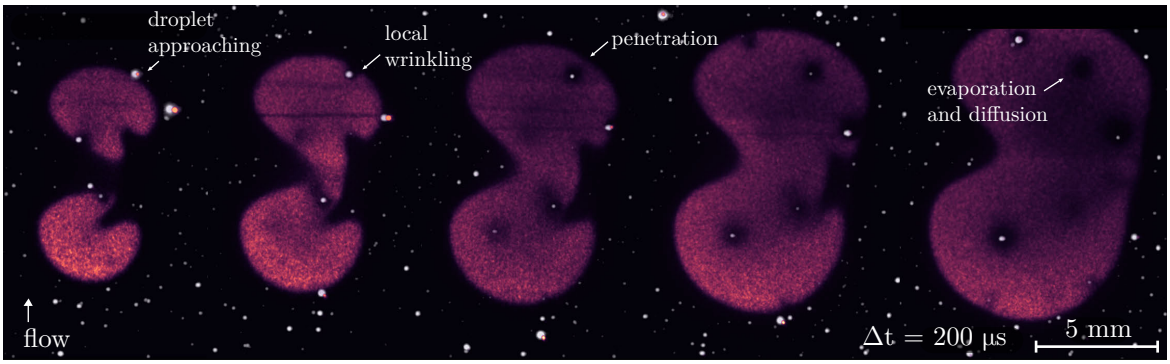

(b) OH/fuel PLIF, event 2

Fig. 6.4 Examples of inter-droplet propagation mode visualised by (a) OH* and (b) OH/fuel PLIF – ATJ-8, ϕ=1.4, d_{32}=33 µm.

Inter-droplet propagation mode

For sprays in the 21-33 μm SMD range, the heat release across the flame was significantly more homogenous in stoichiometric to rich mixtures (Fig. 6.4a) than in lean mixtures characterised by the droplet propagation mode (Fig. 6.3a). This effect seemed to be a consequence of fast evaporation rates found close to the flame front, as suggested by the PLIF sequence (Fig. 6.4b) with droplets quickly disappearing as they approached the flame. Consequently, a less stratified inter-droplet region is expected, richer than in overall lean mixtures with the same droplet sizes.

Further, the expansion of the flame pushed small droplets in its vicinity away towards its propagation direction, eventually leading to their full evaporation. Yet, large droplets survived the propagating front likely due to their higher momentum, evaporating significantly close to the flame front and producing small regions of high curvature. As a result, OH* inhomogeneities was verified across the flame, likely around large droplets penetrating the flame or in regions where full droplet vaporisation

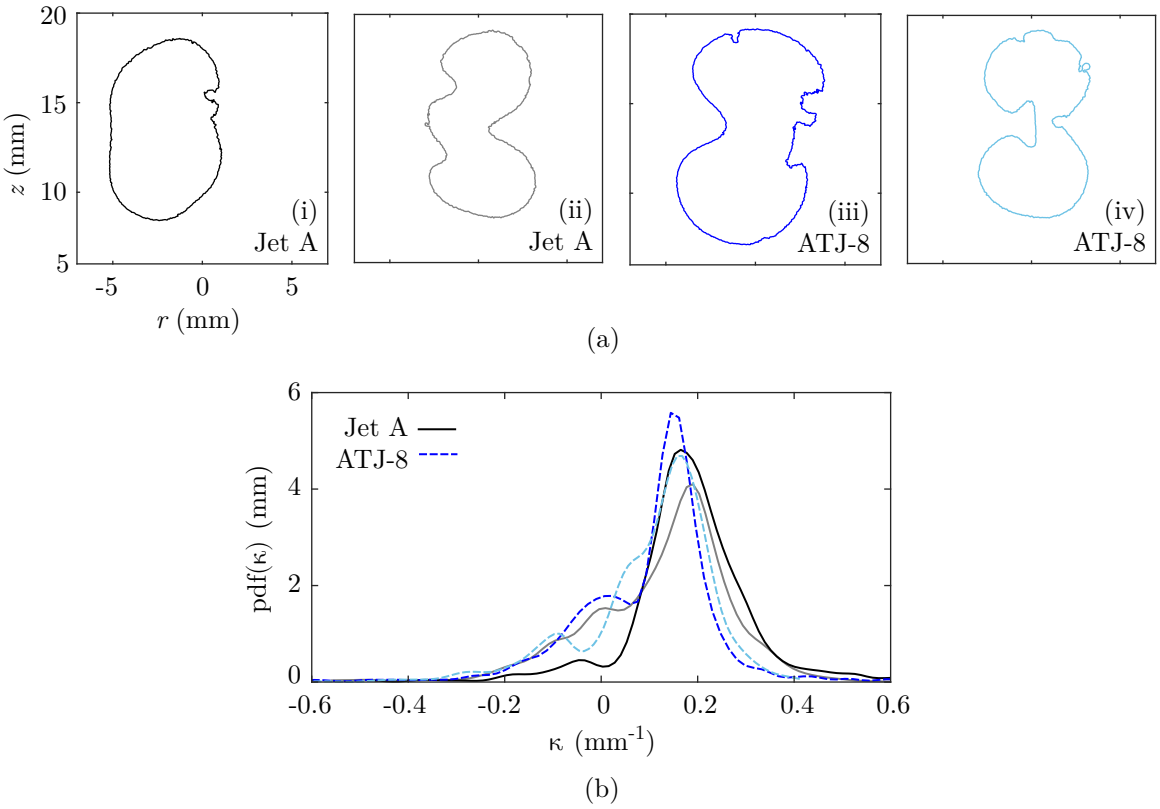

Fig. 6.5 Shape of the flames (a) and respective curvature pdfs (b) for Jet A and ATJ-8 at 1.35 ms after the spark – ϕ=1.4, d_{32}=33 µm.

occurred at the flame front. This effect is less visible for ATJ-8 (Fig. 6.4a), but is clearly seen in Jet A (Fig. 6.2a) for the same condition (ϕ=1.4, d_{32}=33 µm). Nevertheless, the OH* signal was still generally higher and more uniform than for droplet-propagation cases. These observations are, again, consistent with previous DNS works [Wandel et al., 2009; Neophytou, Mastorakos and Cant, 2012; Wacks et al., 2016], and describe the inter-droplet ignition mode as defined in [Neophytou, Mastorakos and Cant, 2012].

Interestingly, some of the largest droplets in the flow fully penetrated the flame front reaching the centre of the burnt gases, where they continued to evaporate. Although a precise evaluation of the change in droplet size is not feasible in PLIF studies due to potential out-of-plane motion, the dark regions surrounding the droplets inside the flame indicate the lack of OH as a consequence of a high concentration of fuel vapour. Due to high evaporation rates induced by the high temperatures found inside the flame, combustion products including OH were likely pushed away from the droplets due to a Stefan flow. The OH-poor regions slowly disappeared, indicating a fast diffusion process of fuel within the burnt products. This phenomenon has been used to explain

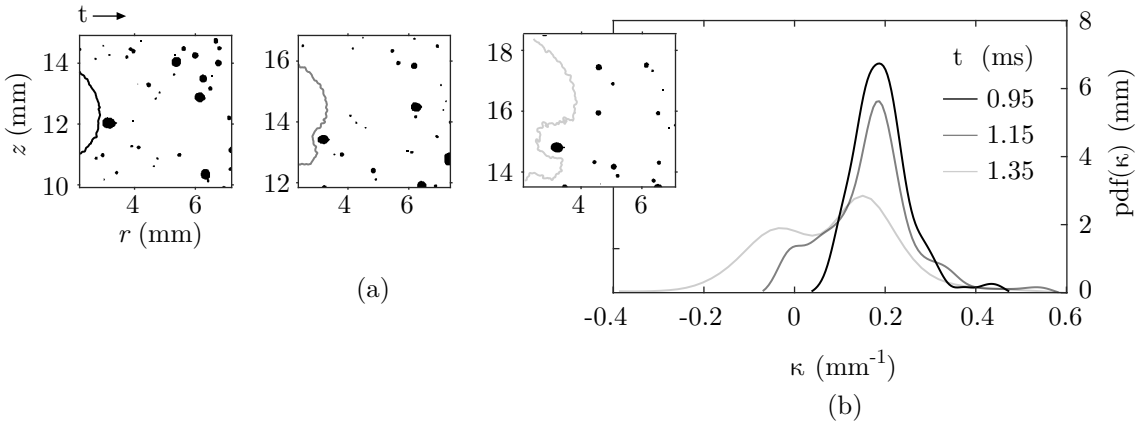

Fig. 6.6 Effect of droplet penetration on the flame curvature – ATJ-8, ϕ=1.4, d_{32}=33 µm.

the unusually high flame speeds that can be found in spray flame. The diffusion of fuel in the products side towards the reaction zone [Wandel et al., 2009] and its possible pyrolysis due to the high combustion temperatures [Neophytou, Mastorakos and Cant, 2012] are two possible contributions. Still, the highest flame speeds in the present experiments (Fig. 6.1) were found for conditions where full vaporisation occurred ahead of the flame, as described in the next section.

Characteristic curvatures concerning two individual events for each fuel at the above-mentioned flow conditions are presented in Fig. 6.5, with the shape of the flame front shown in (a) and its respective curvature pdf in (b). The flames exhibited the characteristic toroidal shape of laser ignition [Bradley et al., 2004] and propagated at a wide range of curvature values, with virtually no difference between the two fuels. A preferential positive curvature value of approximately 0.2 mm^{-1} was found at 1.35 ms after the spark, that is, corresponding to approximately the mean radius of the flame. Still, a significant portion of the flame propagated at negative curvature values, which were attributed to the presence of droplets and turbulence. As a result of this effect, an asymmetric pdf was observed, which differ from findings in gaseous turbulent premixed flames [Gashi et al., 2005; Alqallaf et al., 2019]. The presence of negative curvatures have also been observed in DNS of spray flames both in laminar and turbulent conditions ($S_\mathrm{u}/S^\circ_{\mathrm{L,g},\phi=1}$=0–8; $G \gg 1$; d/δ_f =0.02–0.06) [Ozel Erol et al., 2018, 2019]. Although turbulence may mask the contribution of droplets to flame curvature, a clear widening of the curvature pdfs as turbulence increased has been noticed in [Ozel Erol et al., 2018]. This effect can be identified directly in the present experiments by looking at a large droplet approaching the flame front, as shown in Fig. 6.6. The position of the flame front as well as the fuel droplets at three distinct moments are

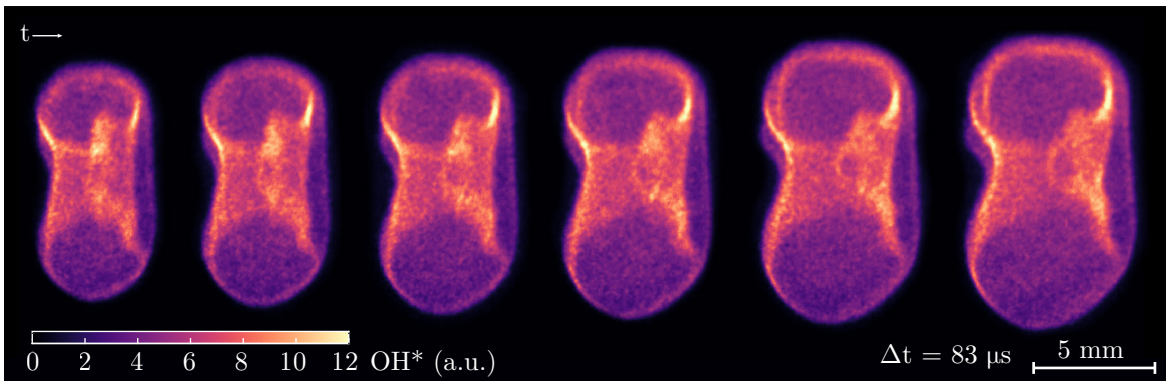

(a) OH*, event 1

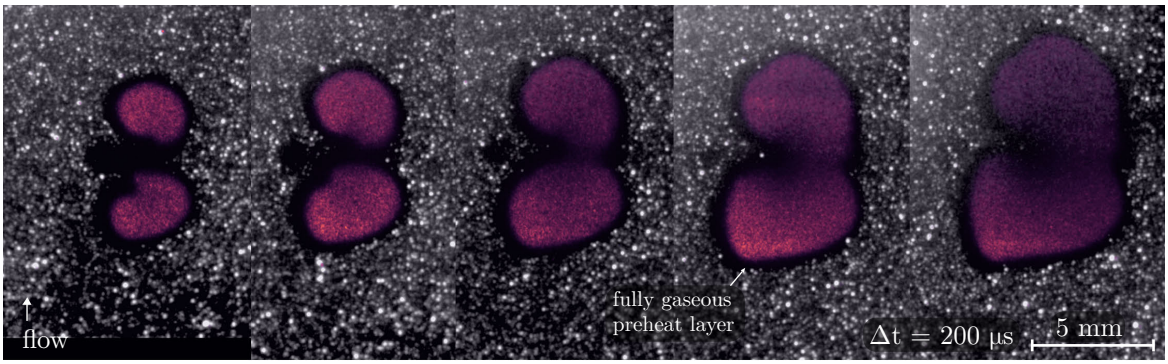

(b) OH/fuel PLIF, event 2

Fig. 6.7 Example of independent events visualised by (a) OH* and (b) OH/fuel PLIF – ATJ-8, ϕ=1.4, d_{32}=16 µm.

shown in Fig. 6.6a, with the respective flame curvature pdf for the region of the flame isolated in (a) is shown in (b). Significant wrinkling of the flame occurred as the large droplet approached the flame, resulting in a wide range of negative curvature values and a decrease of the preferential curvature value of the flame found in the probability density function.

Gaseous-like propagation mode

From the inter-droplet propagation mode, decreasing the SMD of the rich spray further to 16 μm led to flame propagation in a gaseous-like fashion (Fig. 6.7). At this condition, virtually all droplets evaporated far from the flame, giving rise to a thick and fully gaseous layer between the spray and the flame front (Fig. 6.7b), similarly to what is found in sheath combustion mode for high G [Chiu and Liu, 1977]. A regime diagram for the range of conditions and their respective Group number is given in Fig. 6.8, with the sheath-combustion line (G=10^2) [Chiu and Liu, 1977] added for reference.

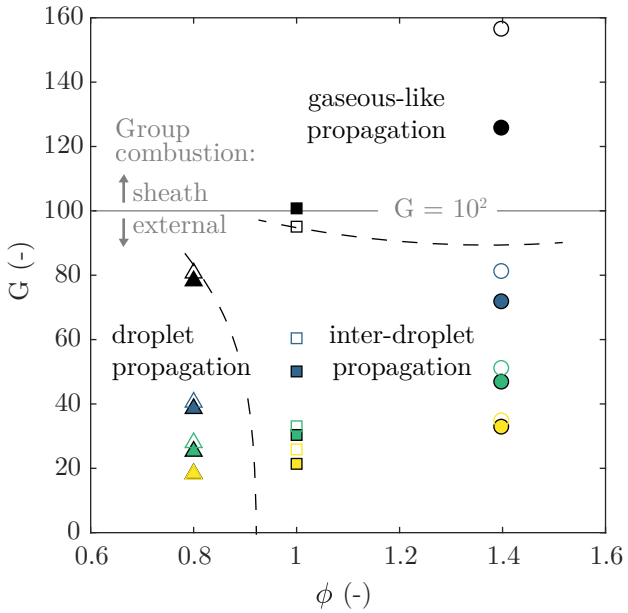

Fig. 6.8 Flame propagation mode diagram for the present experimental conditions. Symbols and colours are the same used in Fig. 4.5.

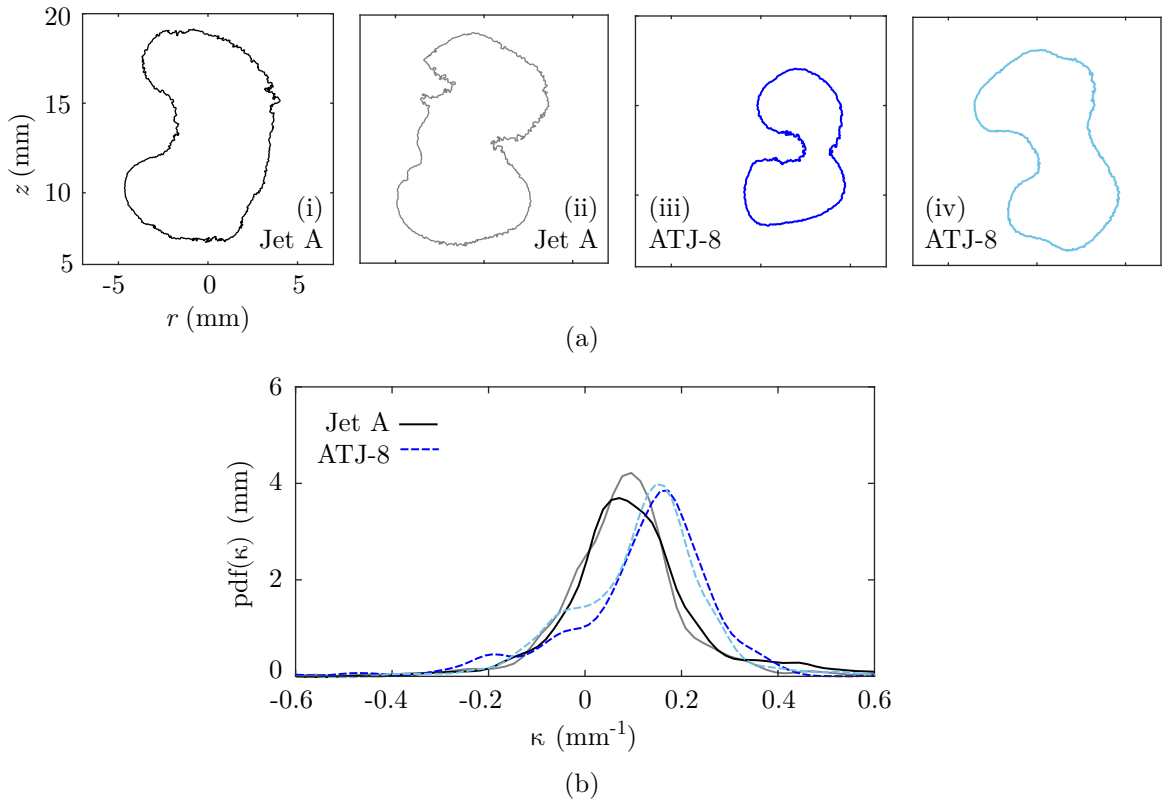

Fig. 6.9 Shape of flame kernels (a) and respective curvature pdfs (b) for Jet A and ATJ-8 at 1.35 ms after the spark – ϕ=1.4, d_{32}=16 µm.

Further, due to evaporation occurring far ahead of the flame, the gaseous-like propagation mode exhibited the highest and most homogenous OH* levels (Fig. 6.7a) within the range of experimental conditions. Evidence from DNS results of [Ozel Erol et al., 2018] has shown that, for similar conditions, such increase in heat release occurring as droplet sizes decrease is a direct consequence of predominantly premixed-type reactions as opposed to predominantly non-premixed; the latter occurring in cases similar to the presented droplet-propagation regimes. In a few events, scarce large droplets were observed in the gaseous layer, nearly reaching the flame. However, full penetration of such droplets across the flame was not observed, with full evaporation occurring within roughly 600 μs once the droplets entered the gaseous layer. This effect is also reflected in the curvature plots, as propagation at a slightly wider range of curvatures was observed in relation to the inter-droplet mode, with the pdfs exhibiting a more symmetric shape (Fig. 6.9).

6.4 Validation experiments

The proposed method for evaluating the unburnt flame speed was validated through experiments with laminar methane-air flames. For these experiments, the flow lines to the atomiser were kept closed and the total premixed methane-air flow was injected at the bottom of the burner, hence minimising turbulence and improving mixing. Measurements of S_u in methane-air mixtures were carried out in a 3-m/s jet at ambient temperature, with the mixture equivalence ratio varying between 0.7-1.3 and incident laser energies varying between 40-60 mJ. Toroidal-like flame kernels typical of laser ignition were observed for all experimental conditions, developing steadily within the visualisation window as shown in Figs. 6.10a-b. The instantaneous OH* and schlieren images of the flame before reaching the limits of the visualisation window are also shown in (b) and (c), respectively.

The mean stretched unburnt flame speed $\overline{S}_\mathrm{u}$ was evaluated and compared to the unstretched values obtained from Cosilab calculations using the GRI-Mech [Smith et al., n.d.] and the experimental data from Vagelopoulos and Egolfopoulos [1998] (Fig. 6.11). Consistent results were found between the results for two different energy levels, indicating the suppression of plasma-cooling effects on the flame. Good agreement between the measurements and the numerical and experimental data used as reference was found for lean to stoichiometric mixtures, although some difference between the experimental and reference values was observed for rich mixtures. The latter effect

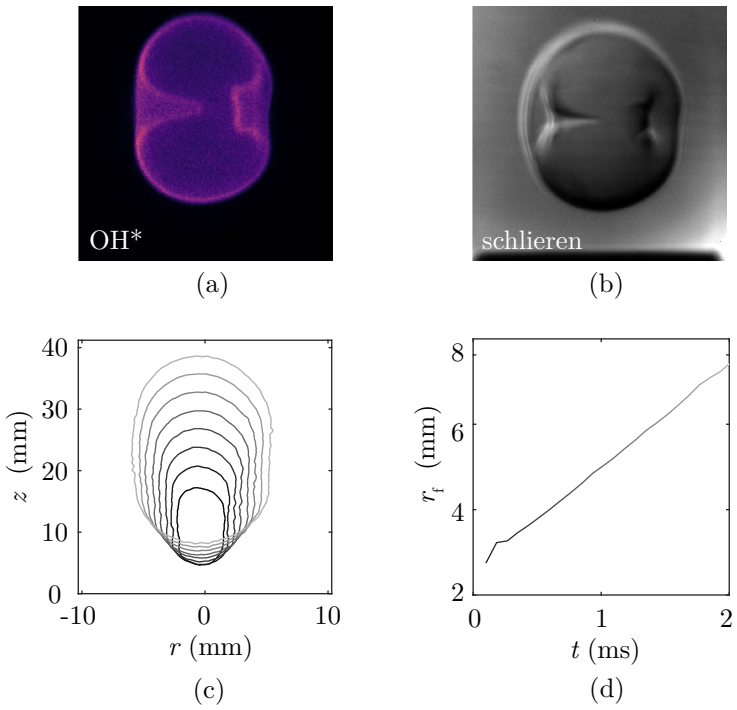

Fig. 6.10 Instantaneous (a) OH* and (c) schlieren image of the methane premixed flame at 2 ms after the spark. The evolution of the (c) shape and (d) radius of the flame calculated from the OH* image sequence in a single ignition event is also shown – $E_{in} = 60$ mJ, $\phi = 1.1$.

could be associated with stretch effects caused by flame curvature and higher Lewis number found in rich conditions [Chen et al., 2009], as the values of S_{u} reported are stretched values. Thus, effects of non-equidiffusive conditions at the flame front can be expected to increase the effect of stretch on the measured S_{b}, especially due to the relative small size of the flame kernels. Still, it is expected that such errors associated with the mean radius of the flame should be of less importance in a spray flame, as droplet-induced curvature and other effects highlighted in Sec. 3 are likely to have a stronger impact on flame speed. Indeed, since the spray flames are wrinkled due to turbulence and due to droplet-scale effects, it is not clear how one could employ, in this case, stretch corrections used to obtain S_{L}° from stretched S_{L} measurements [Egolfopoulos et al., 2014].

Additionally, the effect of the incident laser energy was investigated in ethanol sprays at the experimental conditions shown in Chapter 5. These results are shown in Fig. 6.12, which shows (a) the average flame radius $\bar{r}_f$ and (b) average unburnt flame speed $\bar{S}_u$ as a function of time after the spark event for a specific flow condition. The averages are representative of several ignition events, which number of events

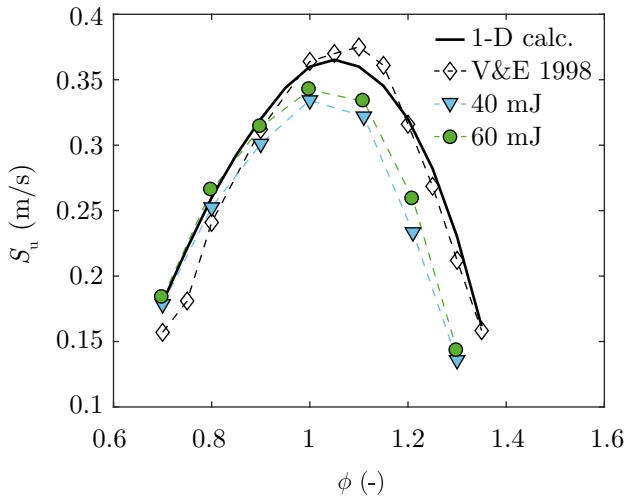

Fig. 6.11 Comparison of experimental measurements of S_u carried out in a laminar methane-air jet against one-dimensional calculations using Cosilab and [Smith et al., n.d.], and experimental data of Vagelopoulos & Egolfopoulos (1998) [Vagelopoulos and Egolfopoulos, 1998].

vary between each energy level due to different probabilities of ignition. The same parameters for individual ignition attempts using 40 mJ are shown in (c) and (d). The variation between ignition attempts of the initial radius of the kernel can be seen in Fig. 6.12c, while Fig. 6.12c shows the fluctuation of the flame speed due to turbulence and the presence of the spray.

Minor effects between different incident laser energies were noticed on the evaluated flame speed. Changes in the unburnt flame speed between different laser energies could be most likely associated with the fact that, as a result of an initially overdriven kernel, higher energies overall result in flame kernels with larger radius at $t \sim 0.1$ ms. Following an initial transient where the flame is still under the influence of the spark – as discussed in Chapter 5 – the growth of the spherically propagating flame stabilises. The flame speed is then evaluated at times greater than the effect of the spark on the flame (t_{crit}), just before the flame leaves the visualisation domain. Additionally, it was found that the resulting value of flame speed for cases of high laser energy will usually be slightly larger than cases with low energy. The measured flame speed will likely be different between these two cases due to effect of stretch caused by the flame's mean curvature, which scales as $1/r_{\text{f}}$.

The unburnt flame speed of ethanol sprays is given for the two preheat temperatures studied, that is, 30 and 50 °C. The effect of preheating in spray flames was significant. For conditions of high preheat temperature, the stretched unburnt flame speed behaved similarly as the laminar burning velocity of the counterpart gaseous mixture, for

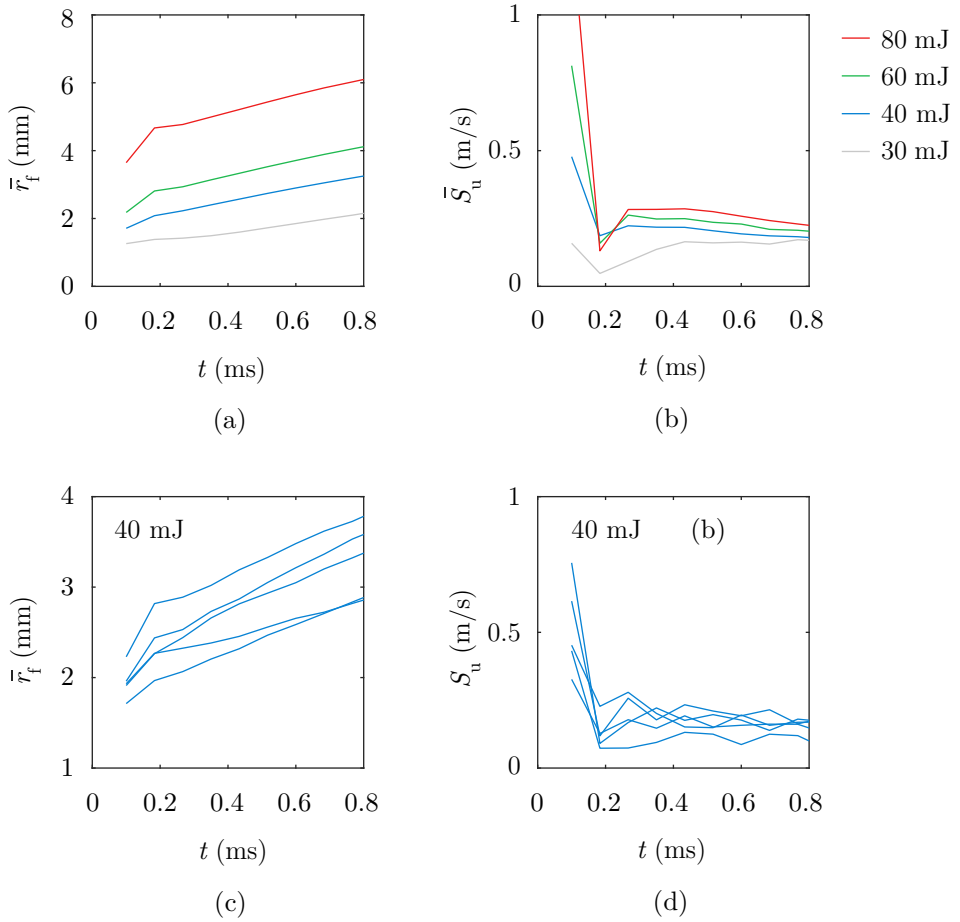

Fig. 6.12 Effect of laser energy on (a) flame radius and (b) unburnt flame speed. Individual ignition attempts with 35 mJ are shown in (c) and (d) – ethanol, T_{in} =50 °C, $\phi = 2$, $\bar{U}_b$= 6 m/s.

conditions close to stoichiometry. For conditions of low prevaporization, the presence of droplets seemed to control flame propagation, as the flame speed is observed to be only slightly affected by changes in equivalence ratio, mostly increasing from the leanest to the richest condition. Similar behaviour was observed with finely atomised jet fuel sprays, as discussed further.

6.5 Summary

In this chapter, three distinct propagation modes of self-sustained spherically expanding flames in jet fuel sprays were identified by means of OH/fuel PLIF and OH* high-speed visualisation. The droplet propagation mode was typical of lean mixtures and large droplet sizes, being characterised by concentrated reactions around large droplets or

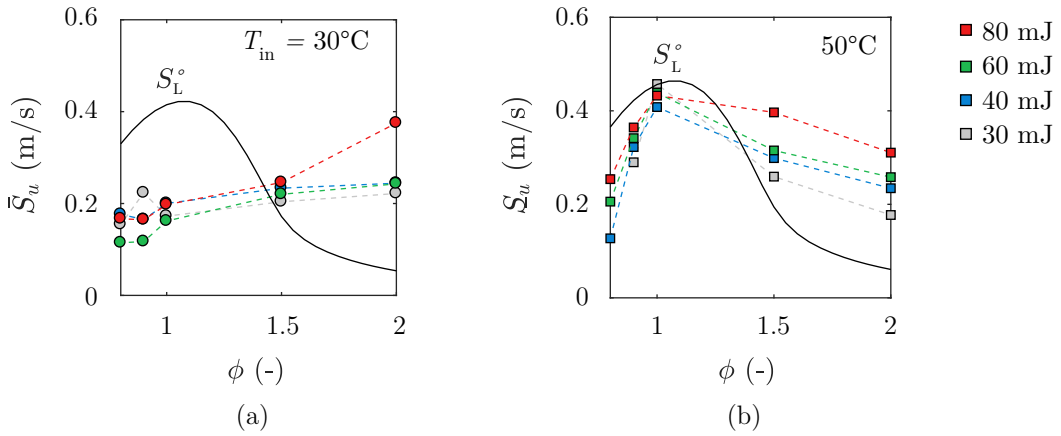

Fig. 6.13 Unburnt flame speed in terms of equivalence ratio for T_{in} = 30 and 50 °C and various energy levels. – $\bar{U}_b$= 6 m/s, ϕ = 0.8-2.

groups of droplets, with the presence of a slowly propagating flame front that ignited new droplets. The inter-droplet propagation mode occurred by improving atomisation or increasing the global equivalence ratio of the spray, presenting a more uniform flame front. Still, significant droplet-flame interaction leading to flame wrinkling was observed in this mode due to large droplets surviving the flame. Finally, at the richest conditions and finest atomisation, a gaseous-like propagation mode was observed, with a flame front resembling that of a gaseous flame. The resulting effect of such propagation modes on the unburnt flame speed was evaluated from the OH* measurements and additional 1-D laminar premixed flames calculations. In addition to the flame speed measurements in jet fuel sprays, a validation of the measurement technique was carried out in laminar premixed methane-air flames, and data was also given for ethanol spray experiments in which the effect of fuel prevaporisation and ignition energy were investigated.

Chapter 7

Low-order modelling of ignition

7.1 Motivation and objectives

Large-eddy simulations have been well established as a tool for the study of spray ignition in gas turbine combustors. Still, using these simulations to assess the stochastic behaviour of ignition is difficult due to the large number of simulations required. This is especially true in sprays, which are distinctly characterised by a strong stochastic behaviour arising from the droplets, as discussed in Chapter 7. For that reason, low-order models for prediction of ignition capability can be valuable tools, allowing the designer to perform parametric studies of the engine at various operating conditions.

The low-order ignition model SPINTHIR is based on an extinction criterion, central to the algorithm of the model, which uses an empirical correlation for the local Karlovitz number and a critical value $\mathrm{Ka}_{\mathrm{crit}}$ at which stochastic "flame particles" extinguish [Neophytou, Richardson and Mastorakos, 2012]. This critical value was verified to be approximately 1.5 in experiments with gaseous premixed flames in isotropic turbulence [Abdel-Gayed and Bradley, 1985], and has been used in SPINTHIR for non-premixed and spray flames [Neophytou, Richardson and Mastorakos, 2012; Neophytou, Mastorakos, Richardson, Stow and Zedda, 2011; Soworka et al., 2014] and premixed flames [Sitte et al., 2016].

In problems involving sprays, the effect of droplets on flame propagation has been accounted for in the model by using a correlation for laminar flame speed in sprays [Neophytou and Mastorakos, 2009]. SPINTHIR has been validated [Neophytou,

The work concerning the fuel fluctuation modelling and its respective calibration is shown in: de Oliveira, P.M., Sitte, M.P., Mastorakos, E. 'Polydispersity effects in low-order ignition modelling of jet fuel sprays', *Combustion Science and Technology* (accepted).

Richardson and Mastorakos, 2012] against experiments with heptane in swirl-stabilised bluff-body burner [Marchione et al., 2009], however, there is insufficient evidence that corroborates the use in sprays of the same Ka_{crit} for gaseous flames. In fact, spray flames in recirculation zones have been observed to extinguish at global Damköhler numbers that differ from gaseous premixed flames [Cavaliere et al., 2013; Yuan et al., 2018]. This is not surprising, as the presence of droplets may locally stretch the flame due to curvature and strain [Wacks and Chakraborty, 2016], as also seen in Chapter 6. Furthermore, in a polydisperse spray it is possible that, for instance, 50% of the total fuel mass may be carried by large and scarce droplets representing less than 2% of the droplet population. In addition to turbulent strain, this strong small-scale fuel inhomogeneities may cause a successfully stablished flame kernel to quench simply due to the lack of flammable mixture in its immediate vicinity. Thus, a model that takes into account flammability effects at the spark location as well as fuel fluctuation effects at the flame front is necessary to accurate ignition prediction in sprays. In order to improve the performance of SPINTHIR in applications with sprays,

- A calibration method is proposed for the extinction criterion of the model, that is, the critical Karlovitz number. This calibration is based directly on the ignition probability measurements obtained in the experiments carried out in uniform well-characterised Jet A sprays presented in Chapter 5.

- The effect of droplet size and equivalence ratio on the calibrated critical Karlovitz number is investigated.

- Fuel fluctuations are introduced in SPINTHIR by evaluating the local liquid equivalence ratio at the cell from a probability density function, which is modelled using a stochastic approach to evaluate the random number of droplets in the model's cell based on the polydispersity of the spray.

- An analysis of the probability density functions of local equivalence ratio at the cell and flammability plots are carried out in terms of spray and mixture parameters. The effect of evaluating the fuel fluctuations on the calibrated critical Karlovitz number is also assessed.

- The model is tested in a Rolls-Royce Trent 1000 combustor for conditions of the engine in which poor atomisation of the fuel is found in the combustor.[1]

[1]The author kindly acknowledges the work of Dr. P. Koniavitis and Dr. A. Giusti, who provided the cold-flow RANS simulation data concerning this combustor, as well as Dr. Marco Zedda at Rolls-Royce for providing the combustor geometry and additional details for the calculations.

7.2 Fuel fluctuation modelling

The effect of liquid fuel fluctuations arising from a polydisperse droplet distribution concerning a single domain cell of the low-order ignition model is here analysed. First, a polydisperse droplet distribution is defined for each cell, based on a modified Rosin-Rammler distribution. Given the local droplet distribution and local mixture parameters obtained from the cold-flow solution, it is possible to obtain the mean number density of each droplet size class. From this parameter, the probability of finding a specific number of droplets of each class in the cell can be modelled using a stochastic approach. Finally, in the model, the number of droplets of each size class in the cell can be randomly obtained from a probability density function for each droplet class, and the resulting random liquid equivalence ratio of the cell can be computed.

In each cell, the spray is defined based on a modified Rosin-Rammler distribution, where the accumulated liquid volume fraction [Rizk and Lefebvre, 1985] is,

$$1 - Q(d) = \exp\left[-\left(\ln d / \ln X\right)^{q}\right]. \tag{7.1}$$

Thus, the fraction of liquid stored in droplets of size k is simply,

$$\Delta Q_k = Q(k) - Q(k-1). \tag{7.2}$$

Based on the liquid volume fraction of the two-phase mixture obtained from the cold-flow solution, x_l, the local liquid volume fraction of the mixture for each droplet class is,

$$x_{\mathrm{l},k} = x_\mathrm{l} \Delta Q_k. \tag{7.3}$$

Further, assuming an arbitrary volume V_0 containing N_k droplets of diameter $d(k)$, the number of droplets of such size in a subvolume V_c (being the volume of a domain cell, Δx^3) follows a binomial distribution. This assumes a purely random process for each droplet class, hence not considering turbulence-induced clustering effects that may occur for specific droplet sizes [Eaton and Fessler, 1994; Sahu et al., 2016]. The probability of finding exactly $N_{k,\mathrm{c}}$ droplets in V_c can be calculated,

$$P_k(N_{k,\mathrm{c}} | N_k, p) = \binom{N_k}{N_{k,\mathrm{c}}} p^{N_{k,\mathrm{c}}} (1-p)^{N_k - N_{k,\mathrm{c}}}, \tag{7.4}$$

where p is the probability of finding a specific droplet in V_c, that is, $p = V_\mathrm{c}/V_0$. Alternatively, the droplet distribution in a cell given by Eq. 7.4 can be approximated by a Poisson distribution [Fessler et al., 1994],

$$P_k(N_{k,\mathrm{c}}) = \frac{\mathrm{e}^{-\mu}\mu^{N_{k,\mathrm{c}}}}{N_{k,\mathrm{c}}!}, \tag{7.5}$$

where μ_k is the mean number of droplets of size k in the cell, $\mu_k = n_k V_\mathrm{c}$, and $n_k = N_k/V_0$. Note that V_0 should be chosen such that,

$$N_k = \frac{x_{\mathrm{l},k} V_0}{\frac{4}{3}\pi\left(\frac{d_k}{2}\right)^3} \gg 1. \tag{7.6}$$

By using Eq. 7.5, a random number of droplets for each class k in the cell, $N_{k,\mathrm{c}}$, can be obtained. Hence, the total amount of liquid fuel in V_c can be simply calculated as the sum of the number of each droplet class in the cell times its respective volume, V_k,

$$V_{\mathrm{l,c}} = \sum_{k=1}^{\infty} V_{\mathrm{l},k} = \sum_{k=1}^{\infty}\left[x_\mathrm{c}\Delta Q_k \frac{N_{k,\mathrm{c}}}{n_k}\right]. \tag{7.7}$$

With additional flow parameters from the cold-flow solution, the particle's liquid equivalence ratio can be easily computed from Eq. 7.7. For the sake of the parametric analysis presented in this section, it can be assumed that $V_{\mathrm{l,c}}/V_\mathrm{c} \ll 1$, such that Eq. 7.7 can be written in terms of the liquid equivalence ratio, ϕ_l,

$$\phi_{\mathrm{l,c}} = \sum_{k=1}^{\infty}\left[\Delta Q_k \frac{N_{k,\mathrm{c}}}{n_k}\frac{1}{V_\mathrm{c}}\right]\phi_\mathrm{l}, \tag{7.8}$$

or in terms of the overall equivalence ratio,

$$\phi_\mathrm{c} = \left[\Omega + (1-\Omega)\sum_{k=1}^{\infty}\Delta Q_k \frac{N_{k,\mathrm{c}}}{n_k}\frac{1}{V_\mathrm{c}}\right]\phi. \tag{7.9}$$

where $\Omega = \phi_\mathrm{g}/\phi$. Thus, the probability density function of ϕ_c can be evaluated using a Monte-Carlo approach. Additionally, the flammability factor of the cell is given by Mastorakos [2009],

$$F_c = \int_{\phi_\mathrm{lean}}^{\phi_\mathrm{rich}} p(\phi_\mathrm{c})\mathrm{d}\phi_\mathrm{c}. \tag{7.10}$$

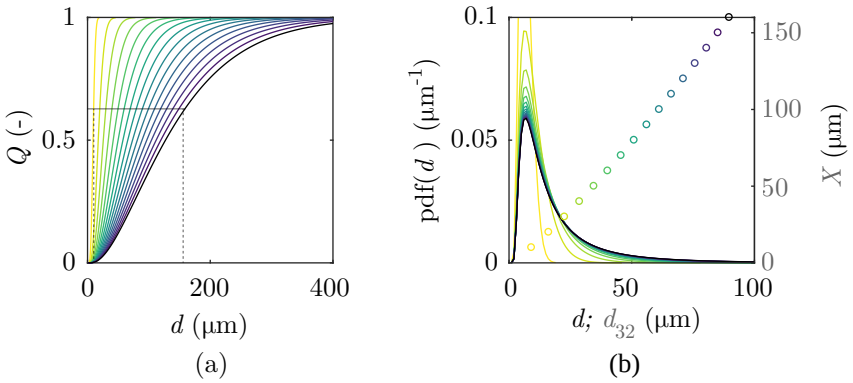

Fig. 7.1 Modified Rosin-Rammler (a) accumulated volume and (b) droplet size pdfs in terms of X. The sauter mean diameter is shown in (b) for the range of X highlighted in (a).

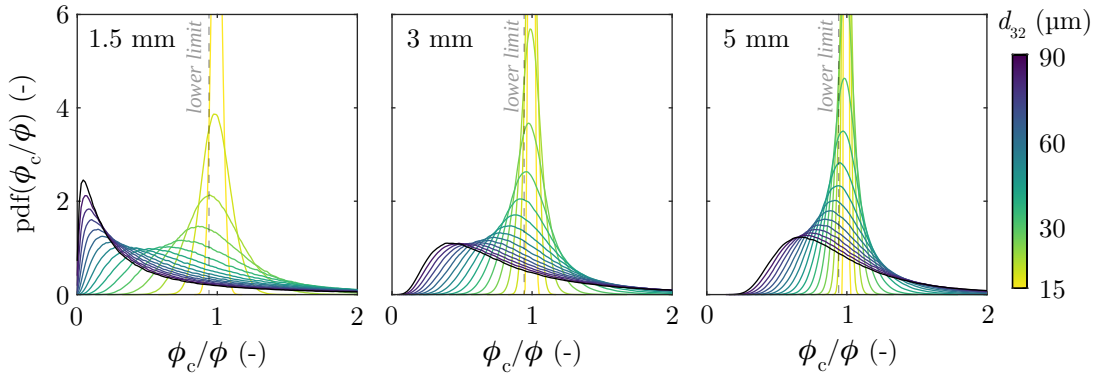

Fig. 7.2 Pdfs of the local equivalence ratio in terms of the droplet distributions (d_{32} = 20-90 μm) for cell size Δ_x of 1.5, 3, and 5 mm — $\phi = 0.7$, $\Omega = 0$.

A parametric analysis was performed considering jet fuel, with prevaporisation between 0 to 99% and overall equivalence ratio from 0.1 to 4. The X parameter of the modified Rosin-Rammler distribution was set from 10 to 160 μm, resulting in the Q curves and pdf(d) shown in Fig. 7.1. For these distributions, the Sauter mean diameter d_{32} as a function of X is also shown in Fig. 7.1a, varying from 15 μm for a fine and monodisperse-like spray up to 90 μm. The cell size was chosen between 1.5 and 5 μm for the analysis. For each condition, the approximation of $P_k(x)$ from Equation 7.5 was used, and every pdf was generated from one million samples.

The effect of the cell size and droplet size distribution on the pdfs of ϕ_c/ϕ is shown in Fig. 7.2, with the line colour scheme shown according to the distributions of droplet size in Fig. 7.1a. For this given condition, ϕ was set just above the lower flammability limit ϕ_{lean} (dashed vertical line). The effect on the local equivalence ratio caused by the polydispersity can be clearly noticed: coarse atomisation conditions (high d_{32}) resulted in high probability for values below ϕ_{lean}, with leaner conditions than the

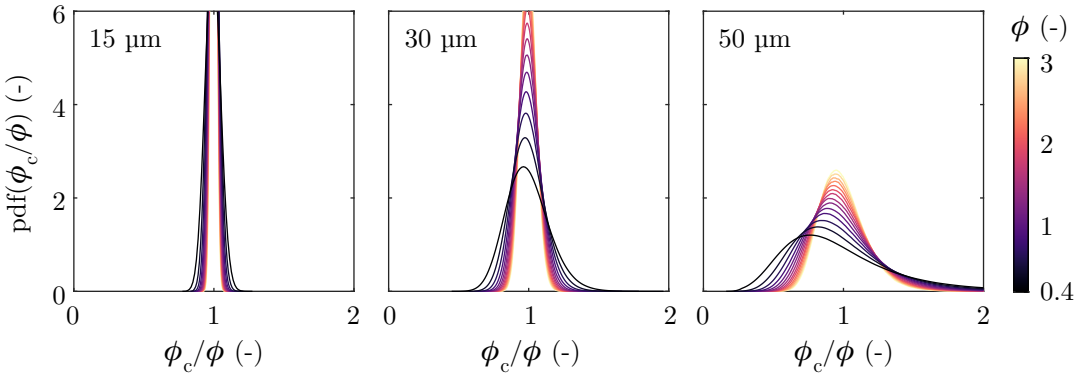

Fig. 7.3 Pdfs of the local equivalence ratio in terms of the overall equivalence ratio ϕ (0.4-3) for droplet distributions with d_{32} of 15, 30, and 50 μm — $\Delta_x = 3$ mm, $\Omega = 0$.

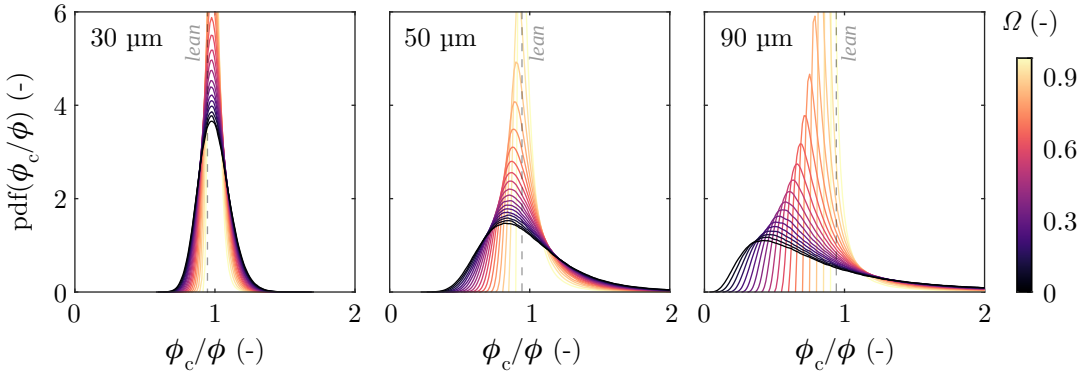

Fig. 7.4 Pdfs of the local equivalence ratio in terms of the prevaporisation degree Ω (0-0.95) for for droplet distributions with d_{32} of 30, 50, and 90 μm — $\phi = 0.7$, $\Delta_x = 3$ mm.

average cell equivalence ratio ϕ being more likely to occur. As d_{32} decreases and the spray becomes closer to monodisperse condition this effect disappears. Evidently, the size of the domain cell also determines the magnitude of the fluctuations in this model. Thus, Δx must be chosen according to physical criteria (e.g. chemical, turbulent, and evaporation time/length scales) in addition to those given by Neophytou, Richardson and Mastorakos [2012] to satisfy the assumption of turbulent transport of the flame particles by the eddies.

The effect of the overall (average) equivalence ratio for a fixed droplet size distribution ($d_{32} = 50\,\mu$m) and a cell size of 3 mm, typical of the spark size shown in Chapter 5 and used here for validation, is shown in Fig. 7.4. Increasing ϕ slightly decreased the magnitude of the fluctuations of ϕ_c, as the droplet number density increases with ϕ. Still, for the given cell size, this effect was only significant for d_{32} over 50 μm. Further, increasing prevaporisation (Fig. 7.4) led to shift of the leanest part of the pdfs towards

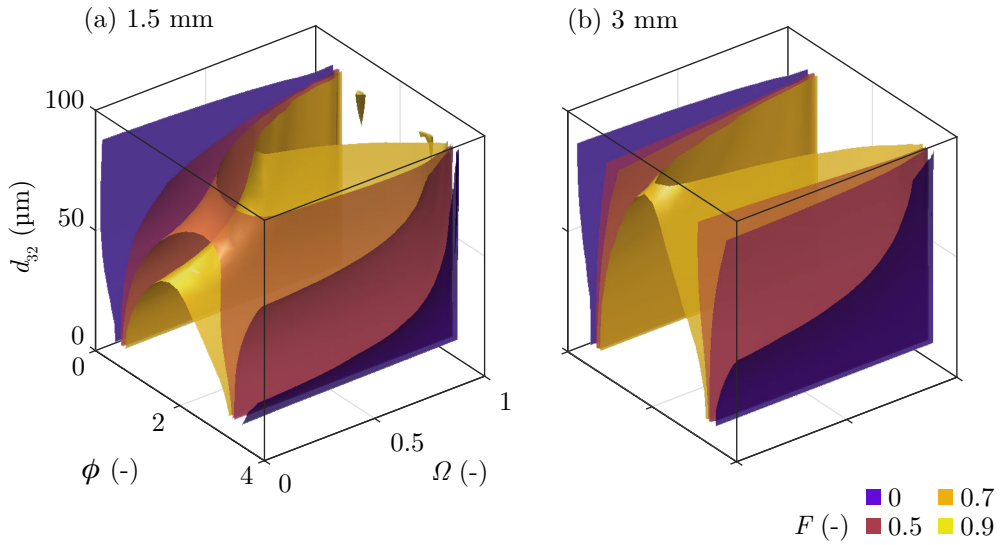

Fig. 7.5 Flammability isosurfaces for cell sizes of (a) 1.5 and (b) 3 mm.

ϕ, as expected. However, this effect also led to a reduction of events where ϕ_c is richer than ϕ, which can be relevant in conditions lower than the lower flammability limit.

Moreover, Figs. 7.2-7.4 show that the polydispersity of the spray may reduce the local flammability at the spark location and surroundings of the flame kernel by producing mixtures that are either below or above the flammable limits. Nevertheless, the actual value of ϕ_c is also key to ignition, as seen that stoichiometric and rich mixtures require significantly less spark energy in order to result in self-sustained flame propagation [Chakraborty and Mastorakos, 2008; Wandel et al., 2009]. Also, the variation of ϕ_p has also a direct impact on $\mathrm{Ka_p}$ through the evaluation of S_L. Thus, for a given lean overall mixture in the combustor, the spray polidispersity can potentially enhance the ignitability by giving rise to locally stoichiometric to rich mixtures, enhancing the flammability at the spark as well as flame propagation. Further, isosurfaces of flammability were plotted in Fig. 7.5 in terms of the overall equivalence ratio, degree of prevaporisation and Sauter mean diameter. For a cell size of 3 mm, positive effects on flammability were only found at values of overall equivalence ratio close to the lower and upper flammability limits, while for a smaller 1.5-mm cell a significant reduction of flammability can be noticed for a stoichiometric equivalence ratio and d_{32} of 50 μm.

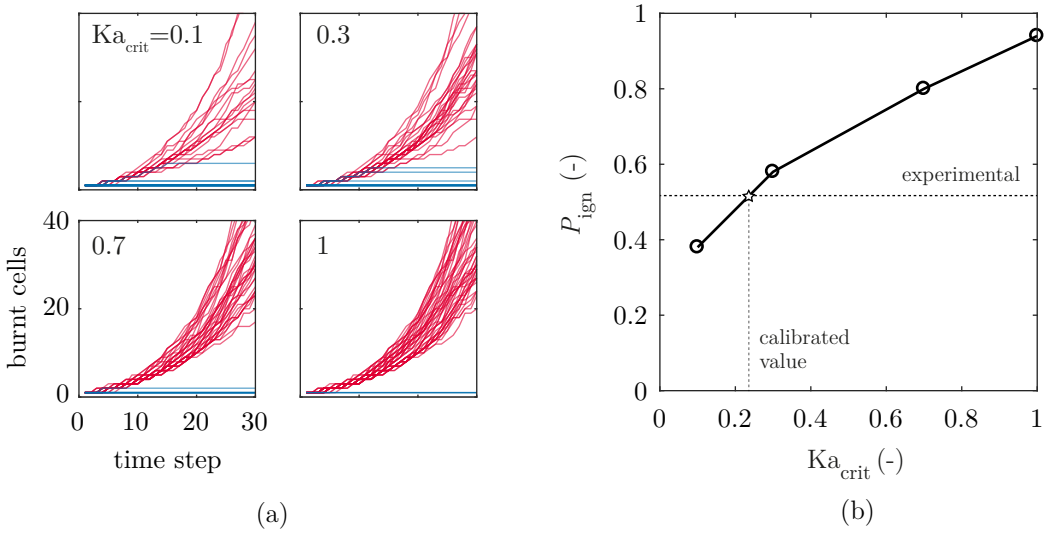

Fig. 7.6 (a) Burnt cells in the domain for $\mathrm{Ka_{crit}}$ set as 0.1, 0.3, 0.7, and 1. Ignition events are shown in red and failed events in blue. (b) Resulting probability of ignition for the conditions presented in (a) and comparison to experimental measurements – Jet A, $\phi_o = 1$, $\phi_g = 0.3$, d_{32} =29 μm.

7.3 Calibration

In order to validate the model's extinction criterion under spray conditions, a calibration method based on the measurements of ignition probability has been proposed. It consists in obtaining a $\mathrm{Ka_{crit}}$ set in the model, for which the resulting ignition probability corresponds to the experimental measurement. The method is shown in Fig. 7.6 for a simulation where the liquid fuel fluctuations (Sec. 7.2) have not been included in the ignition model. The number of burnt cells in time for each set $\mathrm{Ka_{crit}}$ is presented in Fig. 7.6a, with successful ignition events shown in red and failed ignition attempts in blue. Ignition probability was calculated for each value of $\mathrm{Ka_{crit}}$, and the resulting ignition probability in terms of that parameter is shown in Fig. 7.6b. The latter plot was used to obtain a calibrated $\mathrm{Ka_{crit}}$ (approximately 0.2 for the given condition) by comparing the simulation data to the experimental data given in Chapter 5.

In the experiments, P_{ign} and P_{bd} were obtained from multiple spark attempts in the spray flow. As not all sparks resulted in the breakdown of the mixture, the experimental value $P_{\mathrm{ign}}/P_{\mathrm{bd}}$ was used for comparison to P_{ign} obtained from the simulations. In this chapter, the ignition probability given a kernel was formed, $P_{\mathrm{ign}}/P_{\mathrm{bd}}$, is referred to as P_{ign} for simplicity. In the present calibration, the probability of ignition at each condition was evaluated from 50 ignition attempts in each flow condition and $\mathrm{Ka_{crit}}$. The flow was simply modelled as a uniform flow, with constant mean and root-mean-square velocity as well as droplet distribution throughout the domain. The spark

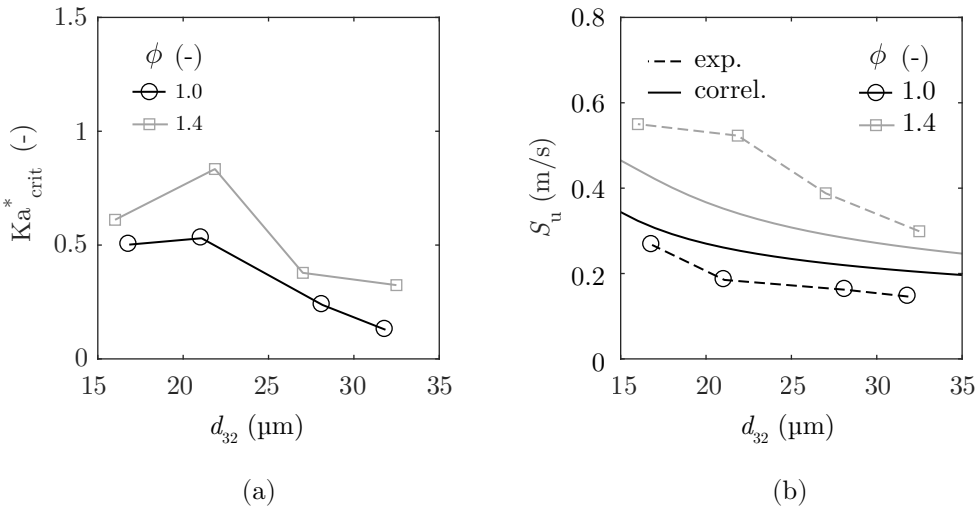

Fig. 7.7 (a) Calibrated critical Karlovitz number for Jet A and (b) comparison of experimental flame speed measurements and values obtained with the correlation by Neophytou and Mastorakos [2009].

diameter and the grid cell size were chosen as 3 mm, that is, smaller than $(C_0\epsilon\Delta t)^{1/2}\Delta t$, for consistency with the modelling assumptions [Neophytou et al., 2010]. Additionally, a 0.5-ms time step was used, which also satisfies the modelling assumptions, being shorter than the mean turbulent scale L_{turb}/u' of the flow (approximately 10 ms).

First, a preliminary calibration of SPINTHIR was carried out without accounting for liquid fuel fluctuations due to the spray. The effects of d_{32} and ϕ on the calibrated critical Karlovitz number, $\text{Ka}^*_{\text{crit}}$, were evaluated as to improve our understanding of the application of the model to sprays. Figure 7.7a shows the resulting $\text{Ka}^*_{\text{crit}}$ as a function of SMD for an overall stoichiometric and a rich mixture condition. Within the present atomisation conditions of 16-33 μm, values of $\text{Ka}^*_{\text{crit}}$ were mostly between 0.1 and 0.6, that is, significantly lower than 1.5 for gaseous premixed flames [Abdel-Gayed and Bradley, 1985]. This is possibly related to phenomena that contribute to flame extinction, enhancing heat loss from the flame in addition to turbulent strain. For example, flame wrinkling and evaporative cooling occurring around large droplets as they approach the flame were observed in DNS [Wandel et al., 2009; Wandel, 2014] as well as in Chapter 6. Also, for the 23-μm rich spray, a high $\text{Ka}^*_{\text{crit}}$ was obtained as a result of a highly under-predicted flame speed by the model's correlation for that condition. Figure 7.7b shows a comparison between measurements and correlation [Neophytou and Mastorakos, 2009] values of flame speed used in SPINTHIR, showing a reasonable agreement between the two, except for the condition pointed out previously. A negative correlation between d_{32} and $\text{Ka}^*_{\text{crit}}$ was observed for both ϕ (Figure 7.7a),

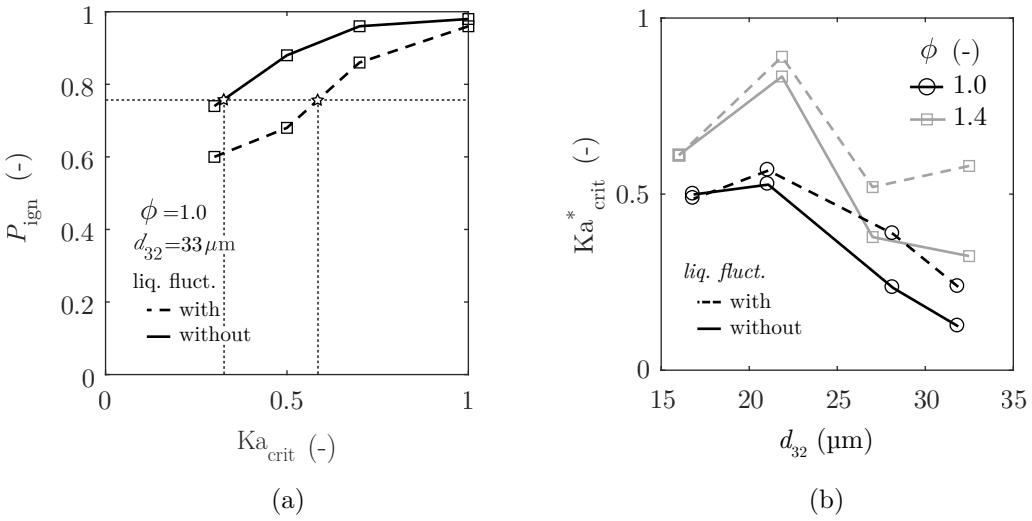

Fig. 7.8 Comparison between simulations with and without the liquid fuel fluctuation model: (a) example of a calibration for a single condition (Jet A, ϕ=1.4, d_{32} =33 μm); (b) resulting calibration for all conditions.

which is consistent with the observed droplet-related phenomena and their contribution to flame extinction, as such effects are likely to become more intense as d_{32} increases.

Fuel fluctuations are accounted for in the calibration shown next, in Fig. 7.8. In this case, the stochastic model given in Sec. 7.2 was included in the low-order ignition model. Local fuel fluctuations affected the calculation of $\mathrm{Ka_p}$ in two particular ways. First, through changes in the flammability of a cell, which may cause a particle to extinguish directly. Second, and perhaps the most important for the present range of conditions, such modelling introduces fluctuations to the local equivalence ratio of the cell and, in turn, to the local S_L. The effect of the fuel fluctuations on the calibration is shown in Fig. 7.8a for a rich 33-μm spray. In this case, a significant decrease of the probability of ignition for any set $\mathrm{Ka_{crit}}$ was observed, leading to a higher $\mathrm{Ka^*_{crit}}$. The resulting $\mathrm{Ka^*_{crit}}$ for the whole range of conditions (ϕ, d_{32}) is shown in Fig. 7.8b. Overall, the implementation of the liquid fluctuations resulted in higher $\mathrm{Ka^*_{crit}}$ values for high SMD conditions, while low SMD conditions remained approximately the same, as it was expected from the results presented in the Monte-Carlo analysis of the model.

7.4 Application to gas-turbine combustors

SPINTHIR was tested by simulating the ignition at sub-idle conditions of the Rolls-Royce Trent 1000 combustor. Cold-flow data, necessary as input for SPINTHIR

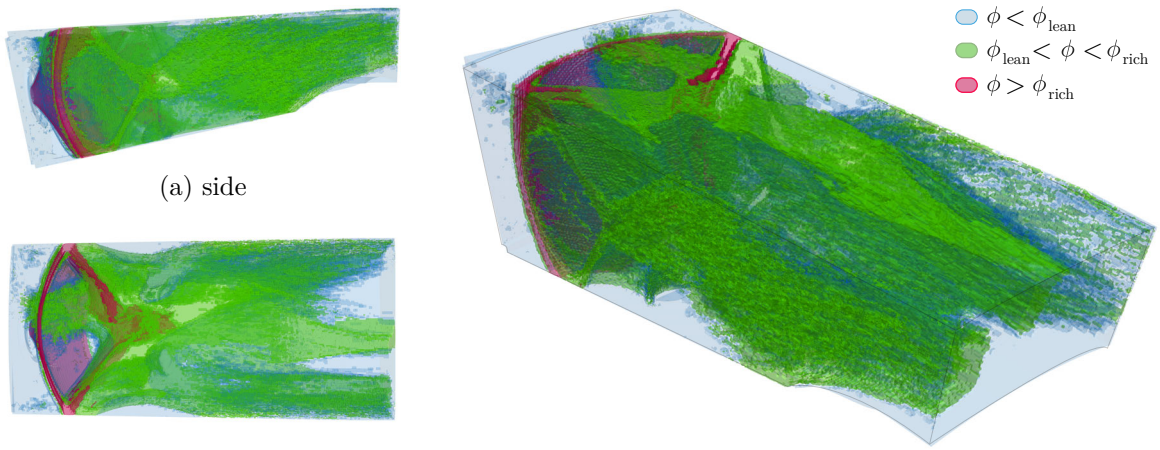

(a) side

(b) top

(c) isometric

Fig. 7.9 Fuel distribution in a sector of a Trent 1000 combustor. Flammable regions are depicted in green.

computation, was obtained from a Reynolds-averaged Navier-Stokes (RANS) simulation of a single sector of the combustor, in which the combustor's pre-diffuser and inner and outer annuli were included in the computational domain. The simulation was performed using the Rolls-Royce proprietary finite volume code PRECISE-UNS. The code implements an Eulerian-Lagrangian approach for dilute spray in low-Mach number flows. A standard k-epsilon turbulence model was used for the simulation and second-order discretisation schemes were used for all the quantities but turbulence model variables, for which the upwind scheme was employed. The numerical mesh used comprised a hexa-dominant unstructured mesh of about 20 million cells refined close to the injector and in high shear region, and was provided by Rolls-Royce plc. Mesh independence of the results was assessed in preliminary computations. Velocity profiles obtained from simulations of the compressor were imposed at the inlet, whereas an outlet condition was used at the combustor's exit. The operating condition is representative of sub-idle operation of the engine. The fuel spray at the injector was assumed to follow a Rosin-Rammler distribution with d_{32} equal to 50 µm.

The fuel distribution in the combustor at the condition studied is shown in Fig. 7.9, with green isocountours representing flammable regions and blue and red isocontours representing regions below the lean limit and above the rich flammability limit, respectively. It should be noted that the droplet Sauter mean diameter remained fairly similar in the combustor, resulting in little variation from the specified value at the injection. Further, the velocity field is shown in Fig. 7.10, normalised in terms of the

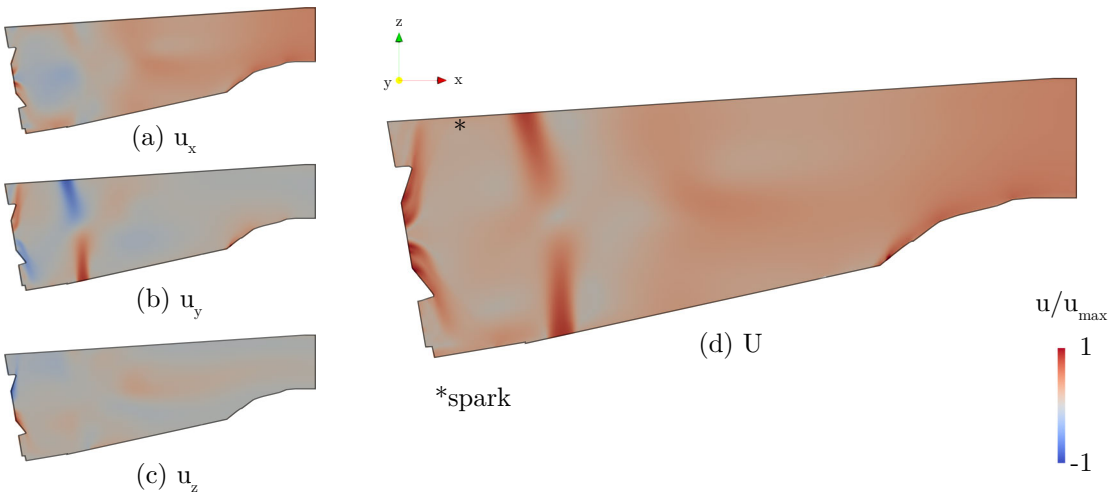

Fig. 7.10 Gas velocity components (a-c) and magnitude (d) in a sector of a Trent 1000 combustor, shown at the cross-section $y = 0$.

maximum absolute velocity found in the combustor. The injection regions and dilution jets characterised by a high velocity magnitude can be clearly seen in Fig. 7.10c.

For the ignition simulations with SPINTHIR, the spark location was set at the top of the combustor near the injector location (show in Fig. 7.10d), and a 10-mm diameter kernel was assumed in all spark events. Similar to the simulations for the calibration of $\mathrm{Ka_{crit}}$, the time step and cell size in the model were set as 0.5 ms and 3 mm, respectively. Based on the results given in Sec. 7.3, a $\mathrm{Ka_{crit}}$ of 0.5 was assumed and 500 ignition attempts were carried out. The ignition progress factor, Π, was calculated as the number of burnt cells divided by the number of cells in the combustor. At the end of an ignition attempt, ignition was verified once $\Pi > 0.15$ for the regular SPINTHIR model, and $\Pi > 0.05$ considering the fuel fluctuations model. This threshold is arbitrary and geometry specific, as indicated by Neophytou, Richardson and Mastorakos [2012], and can be verified in the future with help from experimental and high-fidelity reacting simulation data.

Figure 7.11 shows Π in terms of the time after the spark for SPINTHIR (a) without and (b) with the fuel fluctuation model introduced in Sec. 7.2. In most ignition attempts and for both models, the flame particles quenched soon after the "spark", that is, the start of the simulation. Failure to ignite the combustor in (a) was also observed in cases where a large burnt region took place ($\Pi = 0.1$, approximately), although this type of failure event rarely occurred. The ignition probability was evaluated as 18% without the fuel fluctuation model. Once the fuel fluctuations model was used, this

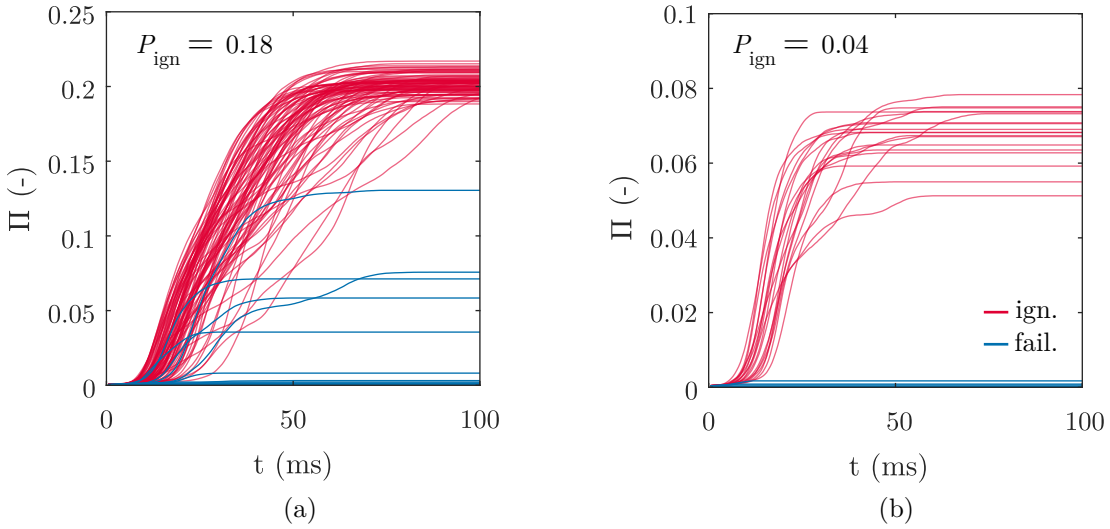

Fig. 7.11 Ignition progress factor in terms of time after the spark for SPINTHIR (a) without and (b) with the fuel fluctuations model.

value decreased significantly, to approximately 4%. This effect is mainly attributed to an overall reduction of the local equivalence ratio of the cell, as shown previously in Fig. 7.2, leading to a low flame speed evaluated from the model's correlation and, in turn, resulting in a high Karlovitz number of the particles. This also leads to an effectively smaller flammable region in the combustor, which explains the lower values of Π obtained in (b) in relation to (a). Moreover, these preliminary results suggest that the modelling approach given in Sec. 7.2 can be used.

7.5 Summary

In this chapter, the effects of liquid fuel fluctuations arising from the spray's polydispersity were investigated in the context of a low-order ignition model applied to a gas-turbine combustor. A stochastic model was developed to account for local variations of the liquid equivalence ratio, presenting a way to incorporate droplet-induced effects, such as the decrease in flammability and the enhancement of extinction by turbulent strain, into the extinction criterion of the model. This criterion based on a critical Karlovitz number was calibrated using ignition probability data presented in Chapter 5 for Jet A. Finally, the calibrated model was tested in an aviation gas-turbine combustor.

Chapter 8

Final remarks

This chapter presents the conclusions of this work. The findings of Chapters 5-7 are presented in Sec. 8.1.1-8.1.3, and recommendations for future work are given in Sec. 8.2.

8.1 Conclusions

In this thesis, the effect of fuel droplets on the initiation and propagation of a flame was investigated in uniform droplet distributions in a turbulent jet. A spherically expanding flame was initiated by a laser spark in a droplet-laden flow characterised by a top-hat velocity profile and a uniform polydispersed droplet distribution, allowing for the flame growth in the absence of large-scale flow inhomogeneities. Experiments were carried out with ethanol and two aviation fuels, namely Jet A and a renewable alternative, ATJ-8. Detailed measurements of the flow were given in Chapter 4.

Measurements of OH* emissions following the spark were used to characterise the early phases of ignition in terms of a critical time scale representing the effects of the spark on the flame, that is, marking the net increase of chain-branching reactions over recombination reactions. This time scale was proposed to distinguish between the kernel generation phase and the flame growth phase based on a quantitative parameter, which then allowed for a revision of the definitions and evaluation of ignition-related parameters (e.g., probabilities of ignition and time scales of ignition failure) in the context of the experiments described previously. A statistical evaluation of the effect of droplets on these time scales and on the probabilities of ignition were discussed in Chapter 5, while their effect on the mechanisms of propagation of a self-sustained flame were investigated in Chapter 6. Finally, measurements and insight from both chapters were used to improve a low-order ignition model, discussed in Chapter 7.

8.1.1 Stochastic nature of ignition

In Chapter 5, the problem of initiation of a spherically expanding flame was investigated in the turbulent laden jet consisting of a droplet distribution in a fuel vapour-air mixture. The probability of breakdown P_{bd} was evaluated from the first frame of the OH* image sequence and depended on the laser beam promoting breakdown of the mixture at the focusing point. In the experiments, P_{bd} was mainly controlled by two competing effects that increased with equivalence ratio: the enhancement of breakdown due to the presence of droplets in the focusing point of the laser, and energy losses due to Mie scattering and absorption occurring along the beam path. Overall, P_{bd} was improved by increasing the equivalence ratio of the mixture, while the effect of prevaporising the fuel was overall detrimental to P_{bd} as it resulted in a decrease of the droplet number density. For high incident laser energies, breakdown was independent of the presence of droplets in the focusing point of the beam, since the amount of energy deposited was above the breakdown threshold for a gaseous mixture.

Given a kernel was initiated by the spark, ignition was strongly associated with the initial kernel size for all conditions with low prevaporisation, suggesting that fluctuations of the overall equivalence ratio at the spark zone controlled the ignition process. This was also supported by the fact that, given a kernel was formed in conditions of higher prevaporisation, ignition was virtually always achieved. In addition to that, an increase of ignition conditions and suppression of long and short-mode failure was also observed when droplet sizes decreased, which represents a combined increase of evaporation rates and decrease in fuel fluctuations due to smaller droplets. Finally, a positive correlation between kernel size and absorbed energy was observed. The dependence of ignition on kernel size and degree of prevaporisation was, therefore, associated to the occurrence of flammable mixture in the spark zone, as increasing both parameters gave rise to smaller fluctuations of fuel in that location.

Time scales of ignition failure were evaluated based on the duration of the effect of the spark on the flame, t_{crit}, and time scale statistics were given for a range of conditions. The duration of the spark effect on the flame varied between 0.4-1.1 ms, being higher for lean mixtures and low-energy sparks. These values were similar to t_{crit} values found in DNS works. The short mode of ignition failure was characteristic of kernels below a minimum size for ignition (1 mm), and was also verified in kernels with more than twice the minimum size. Density functions of kernel sizes conditional to ignition or quenching were also presented, offering a way to implement part of the

stochasticity related to the spark in simulations of ignition of real combustors operating with sprays.

8.1.2 Flame propagation mechanisms

In Chapter 6, a direct visualisation of the propagation mechanisms of spray flames was presented. OH* chemiluminescence, schlieren, and OH/fuel PLIF imaging were used to visualise the ignition and development of spherically expanding flames in polydispersed jet fuel sprays in a turbulent jet. Three distinct propagation modes were identified: the droplet, inter-droplet, and gaseous-like propagation modes.

The droplet-propagation mode was typical of lean mixtures (ϕ=0.8, SMD 16-33 μm) and characterised by reactions around large droplets or groups of droplets immediately following the spark. These individually burning droplets allowed for the propagation of a flame front marked by low heat release. Thus, successful ignition of the flame kernel relied on the propagation of this front to ignite new large droplets in its vicinity. In the absence of individually burning droplets, local extinction was found. These observations are in agreement with DNS, confirming the presence of a slowly propagating flame front due to reaction occurring in below-flammable inter-droplet space even at times greater than the duration of the spark effects on the flame. Significantly low flame speeds around 0.1 m/s were verified in such conditions. Still, a slight increase of flame speed with SMD was observed in both jet fuels, possibly due to an enhancement of small-scale mixture inhomogeneities arising from a more polydisperse spray.

A vigorous and uniform flame was found in stoichiometric to rich conditions (ϕ=1-1.4, SMD 16-27 μm), resulting from high evaporation of the droplets ahead of the flame. In this inter-droplet propagation mode, a negative correlation of flame speed with SMD was observed, with ATJ-8 exhibiting faster flame speeds than ATJ-8 at ϕ of 1.4 and high SMD. The behaviour of flame speed with SMD at these conditions is expected due to a decrease in the spray surface area, detrimental to evaporation. Nonetheless, the measured flame speed values were noticeably higher than the laminar burning velocity in a gaseous mixture. Such high flame speeds have been observed in DNS and associated with an additional influx of fuel which has undergone pyrolysis, from droplets that penetrated the flame. In the experiments, evaporation of the droplets and diffusion of fuel within the burnt products were also observed, corroborating the numerical findings. Negative droplet-induced curvature values were observed as droplets approached the flame, and large droplets fully penetrated the flame.

The highest flame speeds were observed once the SMD decreased to 16 µm in the rich spray (ϕ=1.4), leading to a dense spray and the gaseous-like propagation mode. A suppression of the droplet-induced effects (i.e. wrinkling and penetration) was verified, giving rise to a fully gaseous layer ahead of the flame and, therefore, a flame front more commonly found in propagation in fine mists and volatile-fuel sprays.

Finally, the flame speed measurement technique was verified in laminar premixed methane-air flames as well as in experiments with ethanol sprays. A good agreement between the measurements and laminar flame calculations was obtained, although minor differences were observed at rich conditions. Additionally, a small effect of laser energy was observed on the measurements in ethanol experiments. Both issues were attributed to curvature-induced stretch effects due to the relatively small size of the flame and to non-equidiffusive conditions.

8.1.3 Low-order modelling of ignition

Chapter 7 presented an investigation of the effects of liquid fuel fluctuations arising from the spray's polydispersity in the context of a low-order ignition model. A stochastic modelling approach was used to include such fluctuations in the model, and their resulting effects on the local equivalence ratio and flammability at the model's cell level were investigated as a function of spray characteristics. A Monte-Carlo analysis showed that a change in flammability and, most importantly, high fluctuations of equivalence ratio may occur, presenting a way of incorporating droplet-induced effects in the ignition model.

Further, experimental data of ignition probability in jet fuel sprays was used to calibrate the extinction parameter of the model, the critical Karlovitz number. In this calibration, critical values approximately between 0.2 and 0.6 were found, being significantly lower than those found in the literature for gaseous premixed flames. Once the stochastic fuel fluctuation model was considered in the ignition model, the correlation of the critical Karlovitz number with the spray SMD became less evident, as the calibrated values concerning high SMD conditions increased. Moreover, following the present calibration and introduction of a stochastic model to account for the spray polydispersity, it is expected that the present low-order ignition model should better predict the ignitability of combustors operating with liquid fuel, specially at conditions where fuel atomisation is compromised such as in cold-start of aviation gas turbines.

A preliminary study of the effect of the fuel fluctuations model was carried out by running SPINTHIR in an aviation combustor geometry at conditions similar to

sub-idle operation of the engine. For this test, RANS cold-flow simulation data of a Rolls-Royce Trent 1000 combustor was used. At this condition, liquid fuel was injected in the combustor following a Rosin-Rammler distribution with Sauter mean diameter of 50 μm. Significant variation of fuel concentration was present in the combustor, leading to non-flammable regions due to lean or rich mixtures. The local spray SMD was observed to be approximately constant in the combustor. Preliminary simulation results showed that, at such atomisation conditions, a significantly lower ignition probability was found when fuel fluctuations were considered in the model.

8.2 Future work

In respect to the work on the stochastic ignition behaviour of spray flames, the following actions is recommended for future work:

1. Carry out further analysis of the visualisation data from Chapters 5 and 6 to investigate the main reasons behind failed ignition events. Compare these to findings in DNS of spherically expanding flames [Wandel, 2014]. Additionally, verify the relevance of such findings to stable flame conditions by comparison to the local extinction phenomena observed by Verdier et al. [2018].

2. Provide data concerning new experiments with fully prevaporised fuels at the same conditions of this work, allowing for a direct comparison of the present data to gaseous premixed flames. Additionally, verify the relevance of the present findings to conditions closer to gas-turbine operating conditions, that is, with minimum fuel prevaporisation, by running experiments at low temperature and, potentially, at high pressure.

3. Using spectroscopy measurements of the plasma formed after each successful breakdown event, available for all experimental conditions of the present work, investigate the role of radicals in the transition of plasma to flame kernel and their effect on the ignition outcome.

Further, the following points are recommended for continuing the investigation on the effects of droplets on flame propagation:

1. Provide statistics of flame curvature, rather than for a single event, for each propagation mode based on the current PLIF data of this work. Additionally, verify the effect of droplets to the global turbulent flame speed by increase of flame surface area in comparison to a gaseous premixed flame.

2. Provide statistics of droplet evaporation time scales at the flame front and approximate size based on fuel PLIF data. These are valuable results for validation of analytical models relying on this time scale, such as those proposed by Polymeropoulos [1984], Greenberg [2007], and Rochette et al. [2019].

3. Use the ignition probability data, failure time scales, turbulent flame speed and visualisation data available from both Chapters 5 and 6, to verify the ignition/extinction capabilities of Cambridge's Large Eddy Simulation with Doubly Conditional Moment Closure code.

And finally, regarding the improvement of the low-order ignition model SPINTHIR,

1. Develop a criterion based on physical length scales and time scales to constrain the lower and upper limits of the model's cell size at which the fuel fluctuations are evaluated. Line-of-sight and PLIF visualisation data from experiments of Chapter 7 could be used to this end.

2. Based on experimental or numerical data, propose a second local flame extinction criterion, in addition to turbulent strain represented by the critical Karlovitz number, to account for flame extinction due to the low reaction rates arising from the combined heat-sink effect and excess of fuel vapour as a result of strong evaporative cooling of large droplets.

3. Provide a more complete analysis of the effect of the fuel fluctuations model on SPINTHIR, by running the ignition model with the present gas-turbine combustor geometry for additional operation conditions of the engine. To validate SPINTHIR with the new model, high-fidelity reacting simulations of the ignition transient in the combustor can be performed and compared to the ignition progress in the combustor obtained from the low-order ignition model.

References

Abdel-Gayed, R. G. and Bradley, D. [1985], 'Criteria for turbulent propagation limits of premixed flames', *Combust. Flame* **62**, 61–68.

Aggarwal, S. [1998], 'A review of spray ignition phenomena: Present status and future research', *Prog. Energy Combust. Sci.* **24**, 565–600.

Aggarwal, S. K. [2014], 'Single droplet ignition: Theoretical analyses and experimental findings', *Prog. Energy Combust. Sci.* **45**, 79–107.

Aggarwal, S. K. and Sirignano, W. A. [1985], 'Ignition of fuel sprays: Deterministic calculations for idealized droplet arrays', *Symp. (Int.) Combust.* **20**, 1773–1780.

Ahmed, S. F., Balachandran, R., Marchione, T. and Mastorakos, E. [2007], 'Spark ignition of turbulent nonpremixed bluff-body flames', *Combust. Flame* **151**, 366–385.

Ahmed, S. F. and Mastorakos, E. [2006], 'Spark ignition of lifted turbulent jet flames', *Combust. Flame* **146**, 215–231.

Alqallaf, A., Klein, M. and Chakraborty, N. [2019], 'Effects of Lewis Number on the Evolution of Curvature in Spherically Expanding Turbulent Premixed Flames', *Fluids* **4**, 17–27.

Annamalai, K. and Ryan, W. [1992], 'Interactive processes in gasification and combustion. Part I: Liquid drop arrays and clouds', *Prog. Energy Combust. Sci.* **18**, 221–295.

ASTM Standard D7566-16 [2013], Standard Specification for Aviation Turbine Fuels Containing Synthesized Hydrocarbons, Technical report.

Ballal, D. R. and Lefebvre, A. H. [1978*a*], 'Ignition and Flame Quenching of Quiescent Fuel Mists', *Proc. R. Soc. A* **364**, 277–294.

Ballal, D. R. and Lefebvre, A. H. [1978*b*], 'Ignition of liquid fuel sprays at subatmospheric pressures', *Combust. Flame* **31**, 115–126.

Ballal, D. R. and Lefebvre, A. H. [1979], 'Ignition and flame quenching of flowing heterogeneous fuel-air mixtures', *Combust. Flame* **35**, 155–168.

Ballal, D. R. and Lefebvre, A. H. [1981*a*], 'A general model of spark ignition for gaseous and liquid fuel-air mixtures', *Symp. (Int.) Combust.* **18**, 1737–1746.

Ballal, D. R. and Lefebvre, A. H. [1981*b*], 'Flame propagation in heterogeneous mixtures of fuel droplets, fuel vapor and air', *Symp. (Int.) Combust.* **18**, 321–328.

Beduneau, J. L., Kawahara, N., Nakayama, T., Tomita, E. and Ikeda, Y. [2009], 'Laser-induced radical generation and evolution to a self-sustaining flame', *Combust. Flame* **156**, 642–656.

Birch, A. D., Brown, D. R. and Dodson, M. G. [1981], 'Ignition probabilities in turbulent mixing flows', *Symp. (Int.) Combust.* **18**, 1775–1780.

Birch, A. D., Brown, D. R., Dodson, M. G. and Thomas, J. R. [1979], 'Studies of flammability in turbulent flows using laser RAMAN spectroscopy', *Symp. (Int.) Combust.* **17**, 307–314.

Bradley, D. [1992], 'How fast can we burn?', *Symp. (Int.) Combust.* **24**, 247–262.

Bradley, D., Lawes, M., Liao, S. and Saat, A. [2014], 'Laminar mass burning and entrainment velocities and flame instabilities of i-octane, ethanol and hydrous ethanol/air aerosols', *Combust. Flame* **161**, 1620–1632.

Bradley, D., Sheppard, C. G. W., Suardjaja, I. M. and Woolley, R. [2004], 'Fundamentals of high-energy spark ignition with lasers', *Combust. Flame* **138**, 55–77.

Burgoyne, J. H. and Cohen, L. [1954], 'The Effect of Drop Size on Flame Propagation in Liquid Aerosols', *Proc. R. Soc. A* **225**, 375–392.

Cardin, C., Renou, B., Cabot, G. and Boukhalfa, A. M. [2013], 'Experimental analysis of laser-induced spark ignition of lean turbulent premixed flames: New insight into ignition transition', *Combust. Flame* **160**, 1414–1427.

Cavaliere, D. E., Kariuki, J. and Mastorakos, E. [2013], 'A Comparison of the Blow-Off Behaviour of Swirl-Stabilized Premixed, Non-Premixed and Spray Flames', *Flow, Turbul. Combust.* **91**, 347–372.

Čekalin, E. K. [1961], 'Propagation of flame in turbulent flow of two-phase fuel-air mixture', *Symp. (Int.) Combust.* **8**, 1125–1129.

Chakraborty, N. and Mastorakos, E. [2008], 'Direct numerical simulations of localised forced ignition in turbulent mixing layers: The effects of mixture fraction and its gradient', *Flow, Turbul. Combust.* **80**, 155–186.

Chakraborty, N., Mastorakos, E. and Cant, R. S. [2007], 'Effects of turbulence on spark ignition in inhomogeneous mixtures: a direct numerical simulation (DNS) study', *Combust. Sci. Technol.* **179**, 293–317.

Chen, Z., Burke, M. P. and Ju, Y. [2009], 'Effects of Lewis number and ignition energy on the determination of laminar flame speed using propagating spherical flames', *Proc. Combust. Inst.* **32**, 1253–1260.

Chiu, H. H., Kim, H. Y. and Croke, E. J. [1982], 'Internal group combustion of liquid droplets', *Symp. (Int.) Combust.* **19**, 971–980.

Chiu, H. H. and Liu, T. M. [1977], 'Group Combustion of Liquid Droplets', *Combust. Sci. Technol.* **17**, 127–142.

Coleman, H. and Steele, W. [2009], *Experimentation, Validation, and Uncertainty Analysis for Engineers*, 3rd ed. edn, John Wiley & Sons, Inc., Hoboken.

Colket, M., Heyne, J., Rumizen, M., Gupta, M., Edwards, T., Roquemore, W. M., Andac, G., Boehm, R., Lovett, J., Williams, R., Condevaux, J., Turner, D., Rizk, N., Tishkoff, J., Li, C., Moder, J., Friend, D. and Sankaran, V. [2017], 'Overview of the National Jet Fuels Combustion Program', *AIAA J.* **55**, 1087–1104.

Cordier, M., Vandel, A., Cabot, G., Renou, B. and Boukhalfa, A. M. [2013], 'Laser-Induced Spark Ignition of Premixed Confined Swirled Flames', *Combust. Sci. Technol.* **185**, 379–407.

COSILAB [2012], *Cosilab collection, v3.3.2*, Rotexo-Softpredict-Cosilab GmbH and Co. KG Bad Zwischenahn (Germany).

Dagaut, P. [2002], 'On the kinetics of hydrocarbons oxidation from natural gas to kerosene and diesel fuel', *Phys. Chem. Chem. Phys.* **4**, 2079–2094.

Danis, A. M., Namer, I. and Cernansky, N. P. [1988], 'Droplet size and equivalence ratio effects on spark ignition of monodisperse N-heptane and methanol sprays', *Combust. Flame* **74**, 285–294.

Dietrich, D. L., Cernansky, N. P., Somashekara, M. B. and Namer, I. [1991], 'Spark ignition of a bidisperse, n-decane fuel spray', *Symp. (Int.) Combust.* **23**, 1383–1389.

Eaton, J. K. and Fessler, J. R. [1994], 'Preferential concentration of particles by turbulence', *Int. J. Multiph. Flow* **20**, 169–209.

Edwards, J. T. [2017], Reference Jet Fuels for Combustion Testing, *in* '55th AIAA Aerosp. Sci. Meet.', Paper 2017-0146, American Institute of Aeronautics and Astronautics, Reston.

Egolfopoulos, F. N., Hansen, N., Ju, Y., Kohse-Höinghaus, K., Law, C. K. and Qi, F. [2014], 'Advances and challenges in laminar flame experiments and implications for combustion chemistry', *Prog. Energy Combust. Sci.* **43**, 36–67.

El-Rabii, H., Gaborel, G., Lapios, J.-P., Thévenin, D., Rolon, J. and Martin, J.-P. [2005], 'Laser spark ignition of two-phase monodisperse mixtures', *Opt. Commun.* **256**, 495–506.

El-Rabii, H., Zahringer, K., Rolon, J.-C. and Lacas, F. [2004], 'Laser Ignition in a Lean Premixed Prevaporized Injector', *Combust. Sci. Technol.* **176**, 1391–1417.

Fessler, J. R., Kulick, J. D. and Eaton, J. K. [1994], 'Preferential concentration of heavy particles in a turbulent channel flow', *Phys. Fluids* **6**, 3742–3749.

Gashi, S., Hult, J., Jenkins, K. W., Chakraborty, N., Cant, S. and Kaminski, C. F. [2005], 'Curvature and wrinkling of premixed flame kernels — comparisons of OH PLIF and DNS data', *Proc. Combust. Inst.* **30**, 809–817.

Gebel, G. C., Mosbach, T., Meier, W. and Aigner, M. [2015*a*], 'Laser-induced blast waves in air and their effect on monodisperse droplet chains of ethanol and kerosene', *Shock Waves* **25**, 415–429.

Gebel, G. C., Mosbach, T., Meier, W. and Aigner, M. [2015*b*], 'Optical and spectroscopic diagnostics of laser-induced air breakdown and kerosene spray ignition', *Combust. Flame* **162**, 1599–1613.

Gebel, G. C., Mosbach, T., Meier, W., Aigner, M. and Le Brun, S. [2013], 'An Experimental Investigation of Kerosene Droplet Breakup by Laser-Induced Blast Waves', *J. Eng. Gas Turbines Power* **135**, 021505.

Greenberg, J. [2007], 'Finite-rate evaporation and droplet drag effects in spherical flame front propagation through a liquid fuel mist', *Combust. Flame* **148**, 187–197.

Hardalupas, Y. and Orain, M. [2004], 'Local measurements of the time-dependent heat release rate and equivalence ratio using chemiluminescent emission from a flame', *Combust. Flame* **139**, 188–207.

Hayashi, S., Kumagai, S. and Sakai, T. [1977], 'Propagation Velocity and Structure of Flames in Droplet-Vapor-Air Mixtures', *Combust. Sci. Technol.* **15**, 169–177.

Hendershott, T. H., Stouffer, S., Monfort, J. R., Diemer, J., Busby, K., Corporan, E., Wrzesinski, P. and Caswell, A. W. [2018], Ignition of Conventional and Alternative Fuel at Low Temperatures in a Single-Cup Swirl-Stabilized Combustor, *in* '56th AIAA Aerosp. Sci. Meet.', American Institute of Aeronautics and Astronautics, Reston, Virginia.

International Civil Aviation Organization (ICAO) [2013], 'Resolutions adopted at the 38th session of the assembly, provisional edition.'.

Kariuki, J. and Mastorakos, E. [2017], 'Experimental investigation of turbulent flames in uniform dispersions of ethanol droplets', *Combust. Flame* **179**, 95–116.

Ko, Y., Anderson, R. W. and Arpaci, V. S. [1991], 'Spark ignition of propane-air mixtures near the minimum ignition energy: Part I. An experimental study', *Combust. Flame* **83**, 75–87.

Kotzagianni, M., Yuan, R., Mastorakos, E. and Couris, S. [2016], 'Laser-induced breakdown spectroscopy measurements of mean mixture fraction in turbulent methane flames with a novel calibration scheme', *Combust. Flame* **167**, 72–85.

Lawes, M., Lee, Y., Mokhtar, A. S. and Woolley, R. [2007], 'Laser Ignition of Iso-Octane Air Aerosols', *Combust. Sci. Technol.* **180**, 296–313.

Lawes, M. and Saat, A. [2011], 'Burning rates of turbulent iso-octane aerosol mixtures in spherical flame explosions', *Proc. Combust. Inst.* **33**, 2047–2054.

Lee, S. H., Do, H. and Yoh, J. J. [2016], 'Simultaneous optical ignition and spectroscopy of a two-phase spray flame', *Combust. Flame* **165**, 334–345.

Lefebvre, A. H. and Ballal, D. R. [2010], *Gas Turbine Combustion: Alternative Fuels and Emissions*, 3rd edn, CRC Press, Boca Raton.

Letty, C., Mastorakos, E., Masri, A. R., Juddoo, M. and O'Loughlin, W. [2012], 'Structure of igniting ethanol and n-heptane spray flames with and without swirl', *Exp. Therm. Fluid Sci.* **43**, 47–54.

Lewis, B. and von Elbe, G. [1961], *Combustion, Flames and Explosions of Gases*, Academic Press, New York and London.

Lorenzetto, G. E. and Lefebvre, a. H. [1977], 'Measurements of Drop Size on a Plain-Jet Airblast Atomizer', *AIAA J.* **15**, 1006–1010.

Marchione, T., Ahmed, S. and Mastorakos, E. [2009], 'Ignition of turbulent swirling n-heptane spray flames using single and multiple sparks', *Combust. Flame* **156**, 166–180.

Marinov, N. M. [1999], 'A detailed chemical kinetic model for high temperature ethanol oxidation', *Int. J. Chem. Kinet.* **31**, 183–220.

Mastorakos, E. [2009], 'Ignition of turbulent non-premixed flames', *Prog. Energy Combust. Sci.* **35**, 57–97.

Mastorakos, E. [2017], 'Forced ignition of turbulent spray flames', *Proc. Combust. Inst.* **36**, 2367–2383.

Mikami, M., Mizuta, Y., Tsuchida, Y. and Kojima, N. [2009], 'Flame structure and stabilization of lean-premixed sprays in a counterflow with low-volatility fuel', *Proc. Combust. Inst.* **32**, 2223–2230.

Mizutani, Y. and Nakajima, A. [1973*a*], 'Combustion of fuel vapor-drop-air systems: Part I-Open burner flames', *Combust. Flame* **20**, 343–350.

Mizutani, Y. and Nakajima, A. [1973*b*], 'Combustion of fuel vapor-drop-air systems: Part II—Spherical flames in a vessel', *Combust. Flame* **20**, 351–357.

Mizutani, Y. and Nishjmoto, T. [1972], 'Turbulent Flame Velocities in Premixed Sprays Part I. Experimental Study', *Combust. Sci. Technol.* **6**, 1–10.

Mizutani, Y. and Ogasaware, M. [1965], 'Laminar flame propagation in droplet suspension of liquid fuel', *Int. J. Heat Mass Transf.* **8**, 921–935.

Moesl, K. G., Vollmer, K. G., Sattelmayer, T., Eckstein, J. and Kopecek, H. [2009], 'Experimental Study on Laser-Induced Ignition of Swirl-Stabilized Kerosene Flames', *J. Eng. Gas Turbines Power* **131**, 021501.

Moffat, R. [1988], 'Describing the uncertainties in experimental results', *Exp. Therm. Fluid Sci.* **1**, 3–17.

Mosbach, T., Sadanandan, R., Meier, W. and Eggels, R. [2010], Experimental Analysis of Altitude Relight Under Realistic Conditions Using Laser and High-Speed Video Techniques, *in* 'Vol. 2 Combust. Fuels Emiss. Parts A B', ASME, 523–532.

Mulla, I. A., Chakravarthy, S. R., Swaminathan, N. and Balachandran, R. [2016], 'Evolution of flame-kernel in laser-induced spark ignited mixtures: A parametric study', *Combust. Flame* **164**, 303–318.

Müsing, A., Riedel, U., Warnatz, J., Herden, W. and Ridderbusch, H. [2007], 'Laser-induced breakdown in air and behind droplets: A detailed Monte-Carlo simulation', *Proc. Combust. Inst.* **31 II**, 3007–3014.

Myers, G. D. and Lefebvre, A. H. [1986], 'Flame propagation in heterogeneous mixtures of fuel drops and air', *Combust. Flame* **66**, 193–210.

Neophytou, A. and Mastorakos, E. [2009], 'Simulations of laminar flame propagation in droplet mists', *Combust. Flame* **156**, 1627–1640.

Neophytou, A., Mastorakos, E. and Cant, R. [2011], 'Complex chemistry simulations of spark ignition in turbulent sprays', *Proc. Combust. Inst.* **33**, 2135–2142.

Neophytou, A., Mastorakos, E. and Cant, R. S. [2010], 'DNS of spark ignition and edge flame propagation in turbulent droplet-laden mixing layers', *Combust. Flame* **157**, 1071–1086.

Neophytou, A., Mastorakos, E. and Cant, R. S. [2012], 'The internal structure of igniting turbulent sprays as revealed by complex chemistry DNS', *Combust. Flame* **159**, 641–664.

Neophytou, A., Mastorakos, E., Richardson, E., Stow, S. and Zedda, M. [2011], A practical model for the high-altitude relight of a gas turbine combustor, *in* '7th Mediterr. Combust. Symp.'.

Neophytou, A., Richardson, E. and Mastorakos, E. [2012], 'Spark ignition of turbulent recirculating non-premixed gas and spray flames: A model for predicting ignition probability', *Combust. Flame* **159**, 1503–1522.

Nicoli, C., Denet, B. and Haldenwang, P. [2015], 'Rich spray-flame propagating through a 2D-Lattice of alkane droplets in air', *Combust. Flame* **162**, 4598–4611.

Nicoli, C., Haldenwang, P. and Denet, B. [2016], 'Spray-Flame Dynamics in a Rich Droplet Array', *Flow, Turbul. Combust.* **96**, 377–389.

Nomura, H., Kawasumi, I., Ujiie, Y. and Sato, J. [2007], 'Effects of pressure on flame propagation in a premixture containing fine fuel droplets', *Proc. Combust. Inst.* **31 II**, 2133–2140.

O'Briant, S. A., Gupta, S. B. and Vasu, S. S. [2016], 'Review: laser ignition for aerospace propulsion', *Propuls. Power Res.* **5**, 1–21.

Orain, M., Baranger, P., Ledier, C., Apeloig, J. and Grisch, F. [2014], 'Fluorescence spectroscopy of kerosene vapour at high temperatures and pressures: Potential for gas turbines measurements', *Appl. Phys. B Lasers Opt.* **116**, 729–745.

Ozel Erol, G., Hasslberger, J., Klein, M. and Chakraborty, N. [2018], 'A direct numerical simulation analysis of spherically expanding turbulent flames in fuel droplet-mists for an overall equivalence ratio of unity', *Phys. Fluids* **30**, 1–21.

Ozel Erol, G., Hasslberger, J., Klein, M. and Chakraborty, N. [2019], 'A Direct Numerical Simulation Investigation of Spherically Expanding Flames Propagating in Fuel Droplet-Mists for Different Droplet Diameters and Overall Equivalence Ratios', *Combust. Sci. Technol.* **191**, 833–867.

Parzen, E. [1962], 'On Estimation of a Probability Density Function and Mode', *Ann. Math. Stat.* **33**, 1065–1076.

Peters, J. E. and Mellor, A. M. [1980], 'An ignition model for quiescent fuel sprays', *Combust. Flame* **38**, 65–74.

Peterson, B., Reuss, D. L. and Sick, V. [2011], 'High-speed imaging analysis of misfires in a spray-guided direct injection engine', *Proc. Combust. Inst.* **33**, 3089–3096.

Peterson, B., Reuss, D. L. and Sick, V. [2014], 'On the ignition and flame development in a spray-guided direct-injection spark-ignition engine', *Combust. Flame* **161**, 240–255.

Phuoc, T. X. [2006], 'Laser-induced spark ignition fundamental and applications', *Opt. Lasers Eng.* **44**, 351–397.

Pinnick, R. G., Biswas, A., Armstrong, R. L., Jennings, S. G., Pendleton, J. D. and Fernández, G. [1990], 'Micron-sized droplets irradiated with a pulsed CO2 laser: measurement of explosion and breakdown thresholds', *Appl. Opt.* **29**, 918.

Poinsot, T. and Veynante, D. [2001], *Theoretical and numerical combustion*, Edwards, Philadelphia.

Polymeropoulos, C. E. [1974], 'Flame Propagation in a One-Dimensional Liquid Fuel Spray', *Combust. Sci. Technol.* **9**, 197–207.

Polymeropoulos, C. E. [1984], 'Flame Propagation in Aerosols of Fuel Droplets, Fuel Vapor and Air', *Combust. Sci. Technol.* **40**, 217–232.

Polymeropoulos, C. E. and Das, S. [1975], 'The effect of droplet size on the burning velocity of kerosene-air sprays', *Combust. Flame* **25**, 247–257.

Pope, S. B. [2000], *Turbulent Flows*, Cambridge University Press, Cambridge.

Reveillon, J. and Vervisch, L. [2005], 'Analysis of weakly turbulent dilute-spray flames and spray combustion regimes', *J. Fluid Mech.* **537**, 317–347.

Richards, G. A. and Lefebvre, A. H. [1989], 'Turbulent flame speeds of hydrocarbon fuel droplets in air', *Combust. Flame* **78**, 299–307.

Rizk, N. K. and Lefebvre, A. H. [1985], 'Drop-size distribution characteristics of spill-return atomizers', *J. Propuls. Power* **1**, 16–22.

Rochette, B., Riber, E. and Cuenot, B. [2019], 'Effect of non-zero relative velocity on the flame speed of two-phase laminar flames', *Proc. Combust. Inst.* **37**, 3393–3400.

Rosenblatt, M. [1956], 'Remarks on Some Nonparametric Estimates of a Density Function', *Ann. Math. Stat.* **27**, 832–837.

Sahu, S., Hardalupas, Y. and Taylor, A. M. K. P. [2016], 'Droplet–turbulence interaction in a confined polydispersed spray: effect of turbulence on droplet dispersion', *J. Fluid Mech.* **794**, 267–309.

Singh, A. K. and Polymeropoulos, C. E. [1988], 'Spark ignition of aerosols', *Symp. (Int.) Combust.* **21**, 513–519.

Sitte, M. P., Bach, E., Kariuki, J., Bauer, H. J. and Mastorakos, E. [2016], 'Simulations and experiments on the ignition probability in turbulent premixed bluff-body flames', *Combust. Theory Model.* **20**, 548–565.

Smith, G. P., Golden, D. M., Frenklach, M., Moriarty, N. W., Eiteneer, B., Goldenberg, M., Bowman, C. T., Hanson, R. K., Song, S., Gardiner Jr., W. C., Lissianski, V. V. and Qin, Z. . [n.d.], 'GRI-Mech 3.0, http://www.me.berkeley.edu/gri_mech/'.

Soworka, T., Gerendas, M., Eggels, R. L. G. M. and Mastorakos, E. [2014], Numerical Investigation of Ignition Performance of a Lean Burn Combustor at Sub-Atmospheric Conditions, *in* 'Vol. 4A Combust. Fuels Emiss.', Paper GT2014-25644, ASME, 1–10.

Spalding, D. B. [1979], *Combustion and mass transfer: a textbook with multiple-choice exercises for engineering students*, Pergamon Press.

Spiglanin, T. A., Mcilroy, A., Fournier, E. W., Cohen, R. B. and Syage, J. A. [1995], 'Time-resolved imaging of flame kernels: Laser spark ignition of H2/O2/Ar mixtures', *Combust. Flame* **102**, 310–328.

Thimothée, R., Chauveau, C., Halter, F., Nicoli, C., Haldenwang, P. and Denet, B. [2017], 'Microgravity experiments and numerical studies on ethanol/air spray flames', *Comptes Rendus - Mec.* **345**, 99–116.

Vagelopoulos, C. M. and Egolfopoulos, F. N. [1998], 'Direct experimental determination of laminar flame speeds', *Symp. (Int.) Combust.* **27**, 513–519.

Verdier, A., Marrero Santiago, J., Vandel, A., Godard, G., Cabot, G. and Renou, B. [2018], 'Local extinction mechanisms analysis of spray jet flame using high speed diagnostics', *Combust. Flame* **193**, 440–452.

Wacks, D. H. and Chakraborty, N. [2016], 'Flame Structure and Propagation in Turbulent Flame-Droplet Interaction: A Direct Numerical Simulation Analysis', *Flow, Turbul. Combust.* **96**, 1053–1081.

Wacks, D. H., Chakraborty, N. and Mastorakos, E. [2016], 'Statistical Analysis of Turbulent Flame-Droplet Interaction: A Direct Numerical Simulation Study', *Flow, Turbul. Combust.* **96**, 573–607.

Wandel, A. P. [2014], 'Influence of scalar dissipation on flame success in turbulent sprays with spark ignition', *Combust. Flame* **161**, 2579–2600.

Wandel, A. P., Chakraborty, N. and Mastorakos, E. [2009], 'Direct numerical simulations of turbulent flame expansion in fine sprays', *Proc. Combust. Inst.* **32**, 2283–2290.

Wang, K., Xu, R., Parise, T., Shao, J., Movaghar, A., Lee, D. J., Park, J. W., Gao, Y., Lu, T., Egolfopoulos, F. N., Davidson, D. F., Hanson, R. K., Bowman, C. T. and Wang, H. [2019], 'A physics-based approach to modeling real-fuel combustion chemistry – IV. HyChem modeling of combustion kinetics of a bio-derived jet fuel and its blends with a conventional Jet A', *Combust. Flame* **193**, 520–537.

Weinberg, F. J. and Wilson, J. R. [1971], 'A Preliminary Investigation of the Use of Focused Laser Beams for Minimum Ignition Energy Studies', *Proc. R. Soc. A Math. Phys. Eng. Sci.* **321**, 41–52.

Yuan, R., Kariuki, J. and Mastorakos, E. [2018], 'Measurements in swirling spray flames at blow-off', *Int. J. Spray Combust. Dyn.* **10**, 185–210.

Appendix A

Video

The visualisation data used in this work was edited as a single movie, available at: *http://www.vimeo.com/pedromo/ignition-spray-flames*

The video consists of four parts:

Part I - Ignition sequence

Shows an example of a schlieren visualisation of the laser pulse, breakdown, and subsequent growth of the flame in an ethanol spray, as shown in Fig. 3.4.

Part II - Ethanol spray ignition

Comprises of multiple ignition attempts, including successful and failed events, in ethanol sprays at various mixture conditions. OH* and schlieren images are shown, similar to those of Fig. 5.4.

Part III - Jet fuel spray ignition

Comprises of multiple ignition attempts in jet fuel sprays at different mixture and atomisation conditions, and for both Jet A and ATJ-8. OH* and schlieren images are shown, similar to those of Fig. 6.2.

Part IV - Propagation mechanisms of spray flames

Includes simultaneous OH/fuel PLIF as well as OH* imaging of each of the propagation modes found in jet fuel spray flames, as shown in Figs. 6.3, 6.4, and 6.7.